

# Search for excited quarks at $\sqrt{s} = 8$ TeV with the CMS Experiment at the Large Hadron Collider

THESIS SUBMITTED TO THE UNIVERSITY OF DELHI  
FOR THE DEGREE OF  
DOCTOR OF PHILOSOPHY



VARUN SHARMA

DEPARTMENT OF PHYSICS & ASTROPHYSICS  
UNIVERSITY OF DELHI  
DELHI 110 007  
INDIA

FEBRUARY, 2016



## DECLARATION

It is certified that the work presented in this thesis entitled “**Search for excited quarks at  $\sqrt{s} = 8$  TeV with the CMS Experiment at the Large Hadron Collider**” has been carried out at the Department of Physics & Astrophysics of the University of Delhi under the supervision of Prof. Brajesh Chandra Choudhary and Prof. Debajyoti Choudhury. This thesis deals with the search of excited quarks in the photon + jet final states at 8 TeV with  $19.7 \text{ fb}^{-1}$  of proton–proton collision data collected by the CMS Experiment at the Large Hadron Collider at European Organization for Nuclear Research (CERN), Geneva, Switzerland.

This work has been done by the candidate himself and, to the best of his knowledge, no part of this work has earlier been submitted for any degree or diploma of this or any other university.

Varun Sharma

(Candidate)

Prof. Brajesh Chandra Choudhary

(Supervisor)

Prof. Debajyoti Choudhury

(Co-Supervisor)

Prof. Amitabha Mukherjee

Head, Department of Physics & Astrophysics

University of Delhi

Delhi 110 007





## Department of Physics & Astrophysics

University of Delhi  
Delhi-110007, India

Date: \_\_\_\_\_

## Certificate of Originality

The research work embodied in this thesis entitled "Search for excited quarks at  $\sqrt{s} = 8$  TeV with the CMS Experiment at the Large Hadron Collider" has been carried out by me at the Department of Physics & Astrophysics, University of Delhi, Delhi, India. The manuscript has been subjected to plagiarism check by Turnitin software. The work submitted for consideration of award of Ph.D is original.

Varun Sharma

Name and Signature of the Candidate



*Dedicated  
To  
My Grand-Parents  
&  
Parents*



## ACKNOWLEDGEMENTS

This thesis is a work of a long journey for five and a half year. It has been an eventful ride where I met numerous people, with each leaving some impression on my professional or personal life. I would like to take this place to acknowledge these people.

First and foremost, I would like to express my gratitude to my thesis supervisor Prof. Brajesh Chandra Choudhary for providing support and expertise. I am really grateful to him for providing the opportunity to work with the CMS experiment at the European Organization for Nuclear Research. His guidance over the years has proved most valuable for my shaping as a researcher. His enthusiasm about the results, whether positive or negative, has been a continuous source of motivation and encouragement. I also learnt from him the importance of being organized and having a professional attitude in research.

I would like to thank my co-supervisor Prof. Debajyoti Choudhury for his invaluable suggestions and comments during my research work. For the innumerable interactions I had with him, whether brief or extended, it always made me ever more motivated and passionate as his deep insight into physics and desire to search for new ideas has always been a source of encouragement. I would also like to thank both my supervisors for their thorough review and patience over my research period and especially during the preparation of this thesis over the last few months.

Many thanks to my Ph.D advisory committee members, Prof. Amitabha Mukherjee and Dr. Samit Mandl, for giving me constructive suggestions and comments at different stages of my Ph.D.

I owe a sincere thank to Dr. Sushil Singh Chauhan with whom I closely worked, during my Ph.D tenure. I am grateful for his help, both fundamental and technical, to learn about the software and analysis aspects. Many thanks to Prof. Robert Harris for carefully reviewing the analysis and his invaluable suggestions to improve the final results. I would also like to acknowledge the fruitful discussions with Dr. John Paul Chou and Dr. Dinko Ferencek on several aspects of this analysis. A vote of thanks to members of the CMS collaboration and people involved in this analysis directly or indirectly at different stages of the analysis.

I would like to thank everyone in the Experimental High Energy Physics group at the University of Delhi, Prof. R. K. Shivpuri, Dr. Kirti Ranjan, Dr. Md. Naimuddin, Dr. Ashok Kumar, Dr. Ashutosh Bhardwaj, and Dr. Satyaki Bhattacharya (now at SINP) for their valuable support during my Ph.D tenure. I am obliged to Prof. Amitabha Mukherjee (Head, Department of Physics & Astrophysics) for providing adequate facilities in the department. I would also like to acknowledge fellow colleagues and faculty members of the India-CMS collaboration for their valuable discussions and suggestions during the collaboration meetings and otherwise.

I would like to thank my seniors who have all graduated and fellow colleagues at our research lab at the University of Delhi, consisting of Dr. Sudha Ahuja, Dr. Sandhya Jain, Dr. Shilpi Jain, Dr. Arun Kumar, Dr. Raman Khurana, Dr. Daljeet Kaur, Ranjeet Dalal, Shivali Malhotra, Ajay Kumar, Pavanpoot Pandey, Rocky Singla, Ram Krishna Sharma, Prabjhot Singh, Sumit Kesri, Ankit Gaur, Priyanka Phogat, Geetika Jain, Aashaq Hussain Shah, Aman Phogat, Mohit Gola, Zuber Ahmad Dar, Mohd. Rafik, Prajesh Sharma, few of whom are also good friends. Many thanks to the staff of CDRST lab, Mohd. Yunus, Sanjay Singh, and Aamir Husain for their innumerable help.

I would like to acknowledge the taxpayers of India and across the globe, whose silent contributions made this experiment possible through the grants from UGC, DAE-DST (Govt. of India) and funding agencies of all the collaborating nations. I would also like to thank the organizers of various summer schools, viz., SUSSP69 (St. Andrews, UK), 8<sup>th</sup> MCnet (Ambleside, UK), Sakura Exchange Program (Osaka, Japan) for inviting and providing necessary financial support for these programs. A special thank to Prof. Silvia Pascoli for inviting me to IPPP, Durham University, UK for research related work and ensuring my pleasant stay at Durham.

I would like to acknowledge my best buddies, Vivek Rajawat, Abhishek Rajawat, Sachin Bhatija, for their support through these years. I thank them for numerous cheerful and unforgettable moments we have shared together. I am thankful to the special person in my life Dr. Bhawna Gomber for being around (virtually) all these years. Many thanks for her love, care, support and patience despite the difficult times.

Finally, my deepest gratitude goes to my loving parents, who mean the world to me. I am and will always be indebted to them for all the sacrifices they have made for me. This thesis would have simply been impossible without their understanding, endless patience and constant encouragement. A big thank to all my cousin brothers and sisters for their continuous love and support through these years, with special mention to little cousin Aarav Dogra.

Varun Sharma

# LIST OF PUBLICATIONS

## Journal Publication:

1. “Search for excited quarks in the  $\gamma$  + jet final state in proton–proton collisions at  $\sqrt{s} = 8$  TeV”, B. C. Choudhary ... **Varun Sharma** ...et. al. [CMS Collaboration]. **Physics Letters B 738 (2014) 274-293.**

## Other Public Results:

1. “Search for excited quarks in the photon + jet final state in proton–proton collisions at  $\sqrt{s} = 8$  TeV”, B. C. Choudhary ... **Varun Sharma** ...et. al. [CMS Collaboration]. **CMS PAS EXO-13-003 (Public Analysis Summary).**

## CMS Analysis Notes:

1. “Search for excited quarks in the photon+jet final state in  $pp$  collisions at  $\sqrt{s} = 8$  TeV in the CMS experiment with  $19.7\text{fb}^{-1}$  of data”, Sushil Singh Chauhan, Brajesh Choudhary, Debajyoti Choudhury, **Varun Sharma**, Mani Tripathi. **CMS Analysis Note-13-218 (2013).**
2. “Search for excited b-quarks in the b-tagged  $\gamma$  + jet final state at 8 TeV”, Brajesh Choudhary, Rocky Bala Garg, **Varun Sharma**. **CMS Analysis Note-15-039 (2015).**
3. “Search for excited quark resonance using the photon+jet mass spectrum with  $2.5\text{fb}^{-1}$  of proton-proton collision data at  $\sqrt{s} = 13$  TeV in the CMS experiment.” Sushil Singh Chauhan, Brajesh Choudhary, Rocky Bala Garg, **Varun Sharma**, Mani Tripathi. **CMS Analysis Note-15-262 (2015).**

## Conference Proceedings/Poster Presentations:

1. “Search for an excited quark resonance decaying to a photon and a jet at the CMS”, **Varun Sharma**. Poster presented at the **Eight MCnet School**, held at Ambleside (Lake District), UK, 24–30 August 2014.
2. “Resonance search for quark excitation with the CMS experiment, **Varun Sharma**. Poster presented at the **37<sup>th</sup> International Conference on High Energy Physics** held at Valencia, Spain, 2–9 July 2014. To be published in Nuclear and Particle Physics Proceedings.

3. “Search for excited quarks in the  $\gamma$  + jet final state in proton proton collisions at 8 TeV”, **Varun Sharma**.

Poster presented at the **LHC Experiments Committee meeting poster session (LHCC)** held at CERN, Switzerland, 5<sup>th</sup> March 2014.

4. “Search for Quark Compositeness”, **Varun Sharma**.

Poster presented at the **69<sup>th</sup> Scottish Universities Summer School in Physics** held at St. Andrews, Scotland, 19<sup>th</sup> August – 1<sup>st</sup> September 2012.

# Search for excited quarks at $\sqrt{s} = 8 \text{ TeV}$ with the CMS Experiment at the Large Hadron Collider

Varun Sharma

Department of Physics & Astrophysics  
University of Delhi

## *ABSTRACT*

Quarks and leptons are understood to be fundamental particles within the framework of the standard model of particle physics. Their existence and properties have been verified by different experiments. Despite its success, the standard model is far from being a complete theory. There are several unexplained phenomena which motivates us to go beyond the standard model. One of the directions is to search for the substructure of quarks, or, in other words, search for the compositeness of quarks. The motivation which makes us turn to this path comes from the experience of the past, in that the use of higher energies to probe the sub-structure, has often led to the observation of something more fundamental. The most compelling sign for the sub-structure of quarks would be the discovery of an excited state of a quark, often termed as the “excited quarks” and denoted by  $q^*$ . Excited quarks may provide some insight as to why there exist three generations of quarks and leptons. Many different models of excited quarks have been put forward, where they can be seen either by contact interactions for scale of compositeness,  $\Lambda \gg \sqrt{s}$  or by gauge interactions for  $\Lambda \leq \sqrt{s}$ . Different experiments, in the past and present have searched for excited quarks with no success and have put lower bounds on the compositeness scale,  $\Lambda$ , and mass of the excited quark,  $M_{q^*}$ .

This thesis presents a search for excited quarks by looking at a final state comprising of a photon and a high  $p_T$  jet using  $19.7 \text{ fb}^{-1}$  of proton-proton collision data collected by the CMS experiment at the LHC at a center-of-mass energy of  $8 \text{ TeV}$ . This final state is also mimicked by several other standard model processes. The dominant contribution comes from the standard model  $\gamma + \text{jet}$  production, which forms an irreducible background for this search. The second largest background comes from QCD dijet or multi-jet processes where one of the high  $p_T$  jet mimics an isolated photon inside the detector. The  $W/Z + \gamma$  processes could also give a similar final state, but due to its small cross section, this background is negligible. The  $q^*$  signal and dominant standard model backgrounds are simulated using PYTHIA event generator and are compared with the data. It is assumed throughout the study presented in this thesis that the LHC center-of-mass energy is larger than the compositeness scale,  $\Lambda$  and excited quarks have a mass scale comparable to that of the dynamics of the new binding force, i.e.,  $M_{q^*} = \Lambda$ . Events containing photons and

jets with high transverse momentum are selected to search for a resonance peak in the invariant mass distribution of the photon and jet. The core of the search for the  $q^*$  resonance is the measurement of invariant mass distribution of the  $\gamma + \text{jet}$  system and the estimation of the background. The background is evaluated using a parameterized fit function estimated using the data. It is advantageous to use a fit function as even though the shape and normalization may agree between the data and the MC simulated background, there are still considerable theoretical and experimental uncertainties to be taken care of in the analysis. The methodology of smooth parameterization makes use of the fact that  $\gamma + \text{jet}$  background always produces a smooth and monotonically decreasing spectrum. The various sources of systematic uncertainties affecting only the signal MC, such as jet energy resolution, photon energy resolution, jet energy calibration scale, photon energy calibration scale, and uncertainty on the integrated luminosity, are considered in the analysis. The data are found to be consistent with the standard model predictions with no evidence of quark compositeness.

The results are presented in terms of the expected and observed 95% confidence level upper limits on the  $\sigma \times \mathcal{B}$  for excited quarks,  $q^*$ , as a function of  $M_{q^*}$  for coupling multiplier,  $f = 1.0$  and  $f = 0.5$ , where  $\sigma$  is the production cross section and  $\mathcal{B}$  is the branching ratio for  $q^* \rightarrow \gamma + \text{jet}$ . For  $q^*$  signal, acceptance times efficiency has been found to range from 54% to 58% for  $q^*$  masses from 1 TeV to 4 TeV. The observed limits are found to be consistent with those expected in the absence of a signal. Excited quarks within the mass range  $0.7 < M_{q^*} < 3.5$  (2.9) TeV are excluded at 95% confidence level for coupling multipliers  $f = 1.0$  (0.5). Based on the theoretical predictions for different coupling strengths from 0.1 to 1.0 and the observed limits, we also present exclusion limits of the excited quark mass as a function of coupling strength. This is the first such study performed at the LHC.

The work presented in the thesis entitled “Search for excited quarks at  $\sqrt{s} = 8$  TeV with the CMS Experiment at the Large Hadron Collider” has been published in Physics Letters B 738 (2014) 274-293.

# Contents

<b>1</b>	<b>Introduction &amp; Theoretical Overview</b>	<b>1</b>
1.1	The Standard Model of Particle Physics . . . . .	2
1.1.1	Fundamental Particles . . . . .	7
1.1.2	Forces of interactions . . . . .	8
1.1.3	Electroweak Unification and Higgs Mechanism . . . . .	11
1.2	Beyond the Standard Model . . . . .	17
1.2.1	The Excited Quark Model . . . . .	18
<b>2</b>	<b>The Experimental Apparatus</b>	<b>23</b>
2.1	The Large Hadron Collider . . . . .	23
2.2	The Compact Muon Solenoid . . . . .	29
2.2.1	Coordinate System . . . . .	31
2.2.2	Magnet . . . . .	32
2.2.3	Tracking System . . . . .	33
2.2.4	Calorimeter System . . . . .	37
2.2.5	Muon System . . . . .	43
2.3	Trigger and Data Acquisition Systems . . . . .	46
2.3.1	Level-1 Trigger . . . . .	48
2.3.2	High Level Trigger . . . . .	49
2.3.3	DAQ . . . . .	50
2.4	Software and Computing . . . . .	50
<b>3</b>	<b>Event Simulation and Data Samples</b>	<b>53</b>
3.1	Event Generation . . . . .	55
3.1.1	Hard Scattering and QCD Radiation . . . . .	55
3.1.2	Parton Shower, Underlying Event and Hadronization . . . . .	56
3.1.3	Monte Carlo Event Generators . . . . .	58
3.2	Detector Simulation . . . . .	59
3.3	Simulated Samples . . . . .	60

3.4	Data Samples . . . . .	63
<b>4</b>	<b>Event Reconstruction and Object Identification</b>	<b>65</b>
4.1	Track Reconstruction . . . . .	67
4.2	Reconstruction of Primary Vertices . . . . .	69
4.3	Photons . . . . .	70
4.3.1	Photon Reconstruction . . . . .	70
4.3.2	Photon Identification . . . . .	75
4.4	Jets . . . . .	79
4.4.1	Particle Flow Reconstruction . . . . .	80
4.4.2	<b>Anti-<math>k_T</math></b> Clustering Algorithm . . . . .	82
4.4.3	Jet Energy Calibrations . . . . .	83
4.4.4	Jet Identification . . . . .	85
<b>5</b>	<b>Search for excited quarks in <math>\gamma +</math> jet final state</b>	<b>87</b>
5.1	Signal : Excited quarks . . . . .	88
5.2	Sources of background . . . . .	90
5.3	Data Samples and Triggers . . . . .	92
5.3.1	Data . . . . .	92
5.3.2	Trigger . . . . .	93
5.4	Reweighting of MC samples for pile-up . . . . .	95
5.5	Event Selection . . . . .	97
5.6	Photon + Jet Spectrum . . . . .	108
5.6.1	Choice of Fit function . . . . .	111
5.7	Interpolation technique . . . . .	115
5.8	Systematic Uncertainties . . . . .	119
5.8.1	Photon and Jet Energy Calibration Scale . . . . .	120
5.8.2	Photon and Jet Energy Resolution . . . . .	121
5.8.3	Final State Radiations . . . . .	121
5.8.4	Background Shape Uncertainty . . . . .	122
5.8.5	Theoretical Uncertainty . . . . .	122
5.8.6	Pileup Uncertainty . . . . .	123
5.8.7	Luminosity . . . . .	123
5.9	Limit setting procedure . . . . .	123
5.9.1	Optimization . . . . .	125
<b>6</b>	<b>Results and Summary</b>	<b>129</b>
6.1	Results . . . . .	129

6.2 Summary . . . . .	134
-----------------------	-----



# List of Figures

1.1	Example of electroweak symmetry breaking for the potential with real scalar, $V(\phi) = \mu^2\phi^2 + \phi^4$ . The ground state for $\mu^2 < 0$ no longer respect the symmetry $\phi \rightarrow -\phi$ . . . . .	15
1.2	Some of the Feynman diagrams for $pp \rightarrow q^* \rightarrow \gamma + \text{jet}$ final state. . . . .	20
2.1	Picture showing the LHC ring and a series of accelerators which boost the proton (ion) beam to different energy levels [84]. . . . .	25
2.2	Layout of LHC ring [85]. . . . .	26
2.3	Total integrated luminosity delivered to the CMS experiment for $pp$ collisions by the LHC during the 2012 run at $\sqrt{s} = 8 \text{ TeV}$ [91]. . . . .	28
2.4	Sectional view of the CMS detector [85]. . . . .	30
2.5	Schematic view of the CMS tracker in the $r - z$ plane [83]. Each line depicts a detector module and double lines represents back-to-back modules. Abbreviations TEC, TIB, TID, TOB, etc. are described later in text. . . . .	33
2.6	Total thickness of the tracker material traversed by a particle produced at the nominal interaction point, as a function of pseudorapidity, expressed in units of (a) radiation length $X_0$ and (b) nuclear interaction length $\lambda_I$ [94].	34
2.7	(a) Hit coverage and (b) geometrical layout of the CMS pixel detector [83]. . . . .	36
2.8	A Schematic layout of the silicon microstrip detector [83]. . . . .	37
2.9	A schematic design of the CMS ECAL showing the arrangement of crystals, supermodules and endcaps with the preshower in front [83]. . . . .	38
2.10	A schematic design of the CMS HCAL showing the barrel section (HB), endcap section (HE), the tail catcher outside the solenoid (HO) and the forward section (HF) [87]. . . . .	41
2.11	A schematic design of one quadrant of the muon system in the $r - z$ plane showing the position of three sub-detectors used for muon detection [85]. . . . .	43
2.12	Individual drift tube cells and pictorial representation of its operation principle [87]. . . . .	44
2.13	Operation principle of the Cathode Strip Chamber [85]. . . . .	45
2.14	Schematic diagram of architecture of CMS DAQ and trigger system [85]. . . . .	47

2.15	Architecture of CMS Level-1 trigger system [108]. . . . .	48
3.1	Illustration of a generated event depicting incoming partons undergoing interaction via a hard scattering process, and outgoing partons showering and hadronizing. . . . .	54
3.2	Hadronization of an initial state of two quarks where another quark pair is created from the energy stored in the color field. . . . .	57
4.1	Transverse view of the CMS detector, showing particle identification [85]. .	66
4.2	Flowchart of event reconstruction algorithms. . . . .	67
4.3	Schematic overview of clustering algorithms in barrel and endcap ECAL regions [139]. . . . .	72
4.4	Infrared safety (top) : Addition of a soft gluon. Collinear safety (bottom) : Splitting of one parton into two collinear partons. . . . .	81
4.5	The behaviors of different jet algorithms in parton level [143]. . . . .	84
5.1	Feynman diagrams for $qg \rightarrow q^* \rightarrow q\gamma$ final state via (left) s- and (right) t-channel processes. . . . .	88
5.2	Invariant mass plot normalized to unity for all the $q^*$ mass points. . . . .	89
5.3	Some of the Feynman diagrams of SM $\gamma +$ jet final states with different possible allowed exchanges. . . . .	90
5.4	Some of the Feynman diagrams for SM QCD Dijet background. . . . .	91
5.5	Feynman diagrams for Bremsstrahlung contribution of SM QCD dijet production. . . . .	92
5.6	Background contributions to $\gamma +$ jet from electroweak processes. . . . .	92
5.7	Trigger turn-on curve for single photon trigger HLT_Photon_150. The errors on each point are statistical only. . . . .	95
5.8	Effect of pileup re-weighting on MC. . . . .	97
5.9	N-1 plots for photon identification and isolation variables. . . . .	99
5.10	Distributions of photon identification and isolation variables after all the selection criteria. . . . .	101
5.11	2-dimensional histogram comparing $p_T$ of $\gamma$ and jet for $q^*$ signal. . . . .	102
5.12	Comparison of Data and MC for jet identification variables after final selection criteria has been applied. . . . .	103
5.13	The $p_T$ and $\eta$ spectrum of the leading $\gamma$ and jet for the events comparing data and MC simulation after applying the final selection criteria. . . . .	106
5.14	The $\Delta\eta(\gamma, jet)$ and $\Delta\phi(\gamma, jet)$ distributions between the leading $\gamma$ and jet comparing data and MC simulation after applying final selection criteria. .	107
5.15	Invariant mass of $\gamma +$ jet. . . . .	107

5.16	Fitting the core of $q^*$ invariant mass for different samples of $M_{q^*}$ from 700 to 1700 GeV with $f = 1.0$ using Breit-Wigner (Blue), Crystal-Ball (Red), and Gaussian (Green) functions to get the mass resolution of each mass point. . . . .	109
5.17	Fitting the core of $q^*$ invariant mass for different samples of $M_{q^*}$ from 2000 to 3500 GeV with $f = 1.0$ using Breit-Wigner (Blue), Crystal-Ball (Red), and Gaussian (Green) functions to get the mass resolution of each mass point. . . . .	110
5.18	Fit function to get the variable binning from resolution of signal samples. .	110
5.19	Fit $\gamma +$ jet invariant mass in data using different fit function. . . . .	112
5.20	Fit to data with different fit ranges. . . . .	114
5.21	The $\gamma +$ jet invariant mass spectrum from data, the result of the fit with fit error, and residuals. . . . .	115
5.22	Graphic display for highest $\gamma +$ jet invariant mass event in different geometric planes, with $M_{\gamma, \text{jet}} = 2934.4 \text{ GeV}$ , $p_T^\gamma = 1361.3 \text{ GeV}$ and $p_T^{\text{jet}} = 1280.2 \text{ GeV}$ . .	116
5.23	$X$ distribution for excited quark with different mass points for generated and Interpolated samples. . . . .	117
5.24	Comparison of $q^*$ resonance shapes for the generated and interpolated samples. The solid lines are from the generated samples ( $q^*$ ) while dotted lines represent interpolated samples (I.M). . . . .	118
5.25	Comparison of $q^*$ resonance shape for generated (solid lines) and interpolated (dotted lines) excited quark at 1.0 and 2.5 TeV. . . . .	119
5.26	Uncertainty in jet Energy Scale as a function of mass. . . . .	120
5.27	Uncertainty in photon energy scale as a function of mass. . . . .	121
5.28	Comparison of interpolated (red dots) and generated signal shapes (black dots) based on the observed limits. . . . .	125
5.29	Optimization based on the expected limits with different $\Delta\eta$ selection criteria. .	126
5.30	Optimization based on the expected limits with different criteria on $p_T$ , $\Delta\eta$ and mass selections. . . . .	126
5.31	Turn on region in the $\gamma +$ jet invariant mass plot for different selection criteria. .	127
6.1	The expected and observed 95% CL upper limits on $\sigma \times \mathcal{B} \times A \times \epsilon$ for $q^* \rightarrow \gamma +$ jet with coupling parameter $f = 1.0$ . The upper limits are also compared with theoretical prediction for $q^*$ production. The uncertainty at $1\sigma$ and $2\sigma$ levels are shown as green and yellow bands, around the expected limit. .	130

6.2	The expected and observed 95% CL upper limits on $\sigma \times \mathcal{B} \times A \times \epsilon$ for $q^* \rightarrow \gamma + \text{jet}$ with coupling parameter $f = 0.5$ . The upper limits are also compared with theoretical prediction for $q^*$ production. The uncertainty at $1\sigma$ and $2\sigma$ levels are shown as green and yellow bands, around the expected limit.	130
6.3	The expected and observed 95% CL upper limits on $\sigma \times \mathcal{B}$ for $q^* \rightarrow \gamma + \text{jet}$ with coupling parameter $f = 1.0$ . The upper limits are also compared with theoretical predictions for $q^*$ production. The uncertainty at $1\sigma$ and $2\sigma$ levels are shown as green and yellow bands, around the expected limit. . .	131
6.4	The expected and observed 95% CL upper limits on $\sigma \times \mathcal{B}$ for $q^* \rightarrow \gamma + \text{jet}$ with coupling parameter $f = 0.5$ . The upper limits are also compared with theoretical predictions for $q^*$ production. The uncertainty at $1\sigma$ and $2\sigma$ levels are shown as green and yellow bands, around the expected limit. . .	131
6.5	Comparison of observed limits for excited quarks with $f = 0.5$ and $1.0$ respectively. . . . .	132
6.6	The expected and observed 95% CL upper limits on $\sigma \times \mathcal{B}$ for $q^* \rightarrow \gamma + \text{jet}$ production, and comparison with theoretical predictions for coupling parameters $f = 0.5$ and $f = 1.0$ respectively. The uncertainty at $1\sigma$ and $2\sigma$ levels are shown as green and yellow bands, around the expected limits. . .	135
6.7	The expected and observed 95% CL upper limits on $\sigma \times \mathcal{B}$ of excited quarks for coupling parameter $f$ , ranging from $f = 0.004$ to $1.0$ . . . . .	135
6.8	The expected (dashed) and observed (red filled) excluded regions at 95% CL as a function of $q^*$ mass and coupling strength for $\Lambda = M_{q^*}$ (left axis) or the $M_{q^*}/\Lambda$ for coupling strength $f = 1$ (right axis). . . . .	136

# List of Tables

1.1	Three generation of elementary particles in the SM [60]. . . . .	8
1.2	Fundamental forces, gauge bosons and scalar field [60]. . . . .	9
1.3	The branching ratios (BR) of various decay channels of the $q^*$ ( $u^*$ , $d^*$ ) of mass $M_{q^*} = 1$ TeV. . . . .	21
3.1	MC samples of excited quarks ( $q^*$ ) simulated and reconstructed at $\sqrt{s} = 8$ TeV, with number of generated events, cross-sections, and coupling strengths. . . . .	61
3.2	Background MC samples simulated and reconstructed at $\sqrt{s} = 8$ TeV. . . .	62
3.3	List of datasets with corresponding Run Range, Luminosity, and JSON file. All the datasets uses AOD tier of the data format. . . . .	63
4.1	Parameter values used in Hybrid algorithm. . . . .	72
4.2	Parameter values used in Multi5 $\times$ 5 algorithm. . . . .	73
5.1	List of HLT paths used in the analysis. . . . .	94
5.2	Effective Area for photon isolation criteria. . . . .	98
5.3	Selection cut flow table for $q^*$ signal with $M_{q^*} = 1$ TeV, data and different backgrounds showing number of expected events after each level. . . . .	105
5.4	Selection efficiencies (in %) for $q^*$ signal samples with $M_{q^*} = 700$ –4500 GeV, and coupling $f = 1.0$ . . . . .	105
5.5	Selection efficiencies (in %) for $q^*$ signal samples with $M_{q^*} = 1000$ – 4500 GeV, and coupling $f = 0.5$ . . . . .	106
5.6	Effect of change in Final state radiations on the mean and width of FAST-SIM $q^*$ shapes at 1 TeV and 3 TeV. . . . .	122
5.7	Table showing expected limits for different cases of optimization. . . . .	127
6.1	Expected and observed 95% CL upper limits on $\sigma \times \mathcal{B}$ (in fb) as a function of resonance mass for couplings strengths $f = 0.5$ and $1.0$ respectively. . . .	133
6.2	Cross section (in pb) of $q^*$ signal samples for different couplings ( $f = 0.04$ to $1.0$ ). . . . .	134



# Chapter 1

## Introduction & Theoretical Overview

The field of particle physics is rooted in the aspiration to address some of the most fundamental questions of the universe that we live in, i.e., what are we and everything around us made up of? The human quest to understand the most fundamental building blocks of the universe and their interactions has a long history. The ancient Indians believed the universe to be made of five basic elements: air, earth, fire, space, and water. Similar ideas also prevailed in other civilizations as well. In 6th century B.C. an Indian philosopher named Kanaada espoused a form of atomism and postulated that all objects in the physical universe were reducible to a finite number of atoms, which he called “anu”. The Greek philosophers Leucippe and his disciple Democritus in 5th century B.C. hypothesized that everything on earth was composed of small indivisible entities, called “the atomos”, the Greek word for indivisible. This understanding has evolved from its roots in natural philosophy and metaphysics into an area of natural science in which experiments attempt to confirm or reject theories that describe the nature of elementary constituents. The picture of these building blocks has changed over the period of time and has led to the development of the “Standard Model (SM)” of particle physics [1–3]. In the last few decades, physics at high energies ( $\sim$ GeV/TeV) has proven to be an efficient way to build and test the SM. In high energy collider experiments, the fundamental idea is to steer two accelerated beams of particles together in opposite directions and study

the properties of the remnant particles produced in the collision.

In this chapter, the theoretical framework of the SM, used to describe the elementary particles and their interactions, is outlined briefly. In addition, the motivation for the search of physics beyond the SM and a brief introduction to the physics of compositeness is also presented. Chapter 2 describes the Large Hadron Collider (LHC), the machine which produces proton-proton (pp) collisions, and the Compact Muon Solenoid (CMS) detector, the instrument which records these interactions. While Chapter 3 discusses the event generation and simulation for signal and background processes, Chapter 4 describes the reconstruction of the physics objects used in the analyses. Chapter 5 describes, in detail, the physics analysis used for the search of excited quarks in the  $\gamma + \text{jet}$  final state and Chapter 6 summarizes the results of the analysis.

## 1.1 The Standard Model of Particle Physics

The modern era of particle physics began at the end of the 19<sup>th</sup> century with the discovery of the first subatomic particle, the electron [4], by J. J. Thomson in 1897, when he observed bending of the cathode rays in the presence of a magnetic field. The chemists and physicists continued their work for several decades to understand the structure of the atom. In 1911, Rutherford gave the concept of nucleus [5, 6] by analyzing the data of Geiger and Marsden on the scattering of  $\alpha$ -particles against a thin gold foil. He showed that atoms consist of a compact positively charged nucleus and a cloud of negative charge composed of electrons. Observations by Thomson and Rutherford led N. Bohr, in 1914, to propose a theory of atomic structure based on quantum ideas [7]. However, the understanding of the composition of the atom only became complete with the discovery of neutrons by Chadwick in 1932 [8]. It was thus confirmed, by early 1930s, that ordinary matter consists of three particles: electrons, protons, and neutrons.

Around the same period, in 1900, M. Planck proposed that electromagnetic radiation comes in packets as quanta of energy but gave no explanation for quantization, which was

later given by Albert Einstein in 1905 using the theory of photoelectric effect [9]. The quanta of electromagnetic radiation was later termed as “photon” by Gilbert N. Lewis in 1926. The discovery of Compton effect by Arthur Holly Compton in 1923 confirmed the particle nature of the photons [10]. A. Einstein, in 1905, introduced a theory of special relativity, that took several years to be accepted, while Paul Dirac, in 1927, combined it with quantum mechanics to form a single theory, known as “quantum field theory” [11]. Dirac used quantum field theory to describe the behaviour of free electrons. Dirac’s equation though appeared to be correct, had negative energy solutions, that could only be explained by the presence of a particle with mass same as that of an electron but opposite in charge. The discovery of positron (anti-electron) in 1933 by Carl Anderson [12] was a triumph of Dirac’s theory. This was the first observation of an anti-particle.

Another astonishing observation seen in the same period was the energy spectrum of electrons in nuclear  $\beta$  decay. Assuming the decay of a nucleus into a lighter nuclei and an electron, the energy of the electron could be explicitly predicted by its kinematics. However, it was observed that the energy spectrum of the electrons was softer and broader than the energies predicted. The effect was explained by Pauli in 1930 by introducing an invisible particle that carried away the missing energy and momentum, and which was termed neutrino ( $\nu$ ) in 1932 by Enrico Fermi. As this process can be explained neither by electromagnetic nor by strong interactions, Fermi in 1934 put forth a theory of  $\beta$  decay [13] that introduced the theory of weak interactions. The neutrinos were experimentally observed for the first time in 1956 by Cowan and Reines [14]. They studied the inverse  $\beta$  decay process  $\bar{\nu} + p^+ \rightarrow n + e^-$  in a large tank of cadmium enriched water at the Savannah river nuclear reactor that gave evidence for anti-neutrino (at that time thought to be neutrino) existence by identifying the positrons.

One question that bothered everyone at that time (1930s) was what binds the nucleus together? Confining several positive charges together into a small region ( $1\text{ fm} = 10^{-15}\text{ m}$ ) results in a strong repulsive electrostatic force. If nuclei are to be stable then the protons need to be bound together by a powerful force. This force was called “strong force”. Hideki

Yukawa in 1934 combined quantum theory and relativity to describe nuclear interaction among nucleons via exchange of a particle called meson [15], later termed as “pions”. Yukawa postulated that the mass of these mesons must be  $\sim 300$  times the mass of electron. Anderson and Neddermeyer in 1937 [16] searched for this particle in cosmic rays and found a particle with mass  $\sim 200$  times that of electron mass, which turned out to be a different particle, later called the muon ( $\mu$ ). The muon is a particle with quantum numbers same as that of an electron but with larger mass. Eventually the pion was discovered by Cecil Powell in cosmic ray experiments in 1947 [17].

The period after 1940’s saw the beginning of particle physics as a distinct field of study with the pioneering work of Feynman [18–20], Schwinger [21, 22], and Tomonaga [23], who together, developed the theory of Quantum Electrodynamics (QED) [24] which explained electromagnetic processes at a basic level in terms of the exchange of photons. The decades of 1940’s and 1950’s saw a number of particles being discovered in scattering experiments. In 1947, a particle called the Kaon, having a long lifetime was discovered by Rochester and Butler [25]. Another particle with similar property, called  $\Lambda$ , was observed by Hopper and Biswas in 1950 [26]. These strange particles were produced copiously and quickly but decayed very slowly. These were later assigned a new quantum number, Strangeness, by Gell-Mann and Nishijima. With advances in the particle physics experiments, in subsequent years more and more new particles were found. In an attempt of arrange these particles they were classified into leptons (light weight), mesons (medium weight) and baryons (heavy weight). The electron, muon, and the neutrino belonged to the species of leptons. Further to this, Murray Gell-Mann organized the hadrons (mesons and baryons) based on charge and strangeness into the famous “Eightfold way”, which led to the prediction of  $\Omega^-$  with a strangeness quantum number of -3.

In 1964, Gell-Mann and Zweig [27, 28] proposed the ‘quark model’ according to which the hadrons have sub-structure and are made up of fundamental particles called ‘quarks’. These proposed quarks were to be of three types or flavors, namely, up ( $u$ ), down, ( $d$ ), and strange ( $s$ ). According to this model, baryons consist of three quarks while the

mesons are made up of a quark and an anti-quark pair. The weakness for this model was that no free quark had been observed by then and as per Pauli's exclusion principle three identical quarks (fermions) cannot co-exist together, which led to the introduction of a new quantum number, 'color'. The quark model required hadrons to be colorless entity and didn't allow quarks to exist in free state. A major triumph for the quark model was the discovery of already predicted  $\Omega^-$  with known quantum numbers at the Brookhaven National Laboratory (BNL) [29]. In 1967, experiments which had beam of electrons striking nuclear targets (or  $e - p$  interactions) i.e., scattering of electron off protons at the experiment at SLAC showed the existence of substructure in the proton, in a manner similar to the way scattering experiments of Rutherford proved the existence of substructure in the atom.

The elementary particles known to physicists by this time comprised of three quarks,  $u$ ,  $d$ , and  $s$ , four leptons,  $e^-$ ,  $\nu_e$ ,  $\mu^-$  and  $\nu_\mu$  and a boson, called photon. The apparent asymmetry between the number of leptons and quarks, in 1964 led Glashow and Bjorken [30] to predict that there might exist a fourth quark and they named it 'charm'. Later in 1970, Glashow, Iliopoulos and Maiani [31] classified particles so that there is symmetry between leptons  $[(e, \nu_e), (\mu, \nu_\mu)]$  and quarks  $[(u, d), (s, c)]$ . They introduced a new quantum number, weak isospin which need to be conserved for weak interactions and also suggested additional  $c$  quark that was not yet discovered. In 1974, two separate experimental groups, one led by S.C.C. Ting at the BNL AGS proton synchrotron and other lead by B. Richter at SLAC/SPEAR  $e^+e^-$  collider independently observed a narrow resonance of the  $c\bar{c}$  bound state ( $J/\psi$  particle) [32, 33]. The generational structure for leptons got extended with the discovery of  $\tau$  lepton by M. Perl et. al. at SLAC/SPEAR in 1975 [34]. This discovery again led to the asymmetry in the number of leptons and baryons and made physicists to search for a new family of quarks. Two years later in 1977, the observation of  $b\bar{b}$  bound state,  $Upsilon(\Upsilon)$  particle by Leon Lederman at Fermilab added new beauty/bottom ( $b$ ) quark [35] to the family of quarks. After a wait of 18 years, the last in the family of quarks the top ( $t$ ) quark was observed in 1995 at the CDF [36] and D0 [37]

experiments at Fermilab.

Discovery of hadron sub-structure suggested a new fundamental explanation of strong nuclear forces to replace Yukawa's meson mediation theory. A new theory, predicting a new particle, gluon, mediating these strong interactions was proposed during this period. The gluon was discovered, when a three-jet event was observed in electron positron collision at TASSO experiment [38] at PETRA collider in 1979. E. Fermi treated theory of weak interactions as contact interactions without introduction of any mediating particles, which proved to be very effective at low energies, however the results from Gargamelle experiments at CERN [39] differed with the theory at higher energies. S. Glashow [1], A. Salam [2], and S. Weinberg [3] proposed a theory of weak interactions which unified electrodynamics and weak interactions and demanded the existence of gauge bosons to mediate these interactions. One concern for this electroweak theory was that the  $W/Z$  bosons had to be massless for the theory to be consistent, while they needed to be heavy for interactions to be weak. The mass of these bosons was explained by the spontaneous symmetry breaking of weak interactions via Higgs mechanism proposed by Higgs [40–42], Englert & Brout [43], Guralnik, Kibble, & Hagen [44] in mid 1960's. The Higgs mechanism predicted a new particle, later called the Higgs boson. The charged weak bosons,  $W^\pm$  [45, 46] and neutral weak boson,  $Z$  [47–49] were later discovered in 1983 by the UA1 and UA2 collaborations in  $p\bar{p}$  collisions at CERN.

The observation of a new boson with properties similar to that of a Higgs boson by the ATLAS [50] and the CMS [51] collaborations with a mass of  $\sim 125$  GeV was an important milestone in the decades long hunt for understanding of the mechanism of electroweak symmetry breaking. In light of this observation at the LHC, the 2013 Nobel Prize in Physics was awarded to Francois Englert and Peter Higgs for the development of spontaneously broken local gauge theories and theoretical insights on the origin of mass.

The properties of the Higgs boson have been extensively studied by the ATLAS [52] and the CMS [53] collaborations. The mass of the Higgs particle has been measured to be  $m_H = 125.5 \pm 0.2(\text{stat})^{+0.5}_{-0.6}(\text{sys})$  GeV/c<sup>2</sup> by ATLAS with a combined signal strength of  $\mu = 1.30 \pm$

$0.12(\text{stat})^{+0.14}_{-0.11}(\text{sys})$  [52] where  $\mu = \sigma/\sigma_{SM}$  and  $m_H = 125.03 \pm 0.27(\text{stat}) \pm 0.15(\text{sys}) \text{ GeV}/c^2$  by CMS with a combined signal strength of  $\mu = 1.00 \pm 0.09(\text{stat}) \pm 0.07(\text{sys})$  [53].

According to our present knowledge, leptons and quarks are fundamental particles, i.e., they are point-like and do not appear to have sub-structures. Our present understanding of the elementary particles and their interactions is encapsulated in the SM of particle physics.

### 1.1.1 Fundamental Particles

The SM is the theoretical basis of modern particle physics which cohesively binds the amalgamation of last 60–70 years of data on elementary particles and their interactions. Summarizing the historical introduction, the SM in its present state, consists of ‘matter particles’: fundamental units of which matter is composed of, and the ‘force carriers’: mediators of the four forces known in physics, namely, strong, electromagnetic, weak and gravitational. The elementary particles can be classified into two classes: the fermions, particles obeying Fermi-Dirac statistics and the bosons, those obeying the Bose-Einstein statistics. The fermions are further categorized into leptons and quarks.

**Leptons:** There are six flavors of leptons: the electron ( $e$ ), muon ( $\mu$ ), tau ( $\tau$ ), and their corresponding neutrinos ( $\nu_e$ ,  $\nu_\mu$ ,  $\nu_\tau$ ) as shown in the left half of Table 1.1. Three of the leptons  $e$ ,  $\mu$ , and  $\tau$  carry a unit charge and interact via the electromagnetic and weak interactions, while the three neutrinos are chargeless and interact only via weak interaction. The SM in its present state does not assign mass term to neutrinos but recent experimental studies have confirmed that indeed they carry a small mass which accounts for the phenomena of neutrino oscillations [54–59]. Each lepton has its anti-particle with similar properties but opposite charge.

**Quarks:** They also come in six flavors: up ( $u$ ), down ( $d$ ), charm ( $c$ ), strange ( $s$ ), top ( $t$ ), and bottom ( $b$ ) and are listed in the right half of Table 1.1. Unlike leptons, quarks carry fractional electric charges – either  $+\frac{2}{3}e$  or  $-\frac{1}{3}e$ , where  $e$  is the charge of the electron. The  $u$ ,  $c$  and  $t$  have a charge of  $+\frac{2}{3}e$  while  $d$ ,  $s$ , and  $b$  have a charge of  $-\frac{1}{3}e$ .

The quarks interact via all the three interactions – strong, electromagnetic, and weak. They have an additional quantum number associated with them, called ‘color charge’. Each quark comes in three colors, often termed red, blue, and green. Colored quarks are not allowed to exist freely in nature, due to their property of confinement (explained in the next section). Quarks bind together via strong interactions to form color neutral composite objects called baryons and mesons. The baryons are made up of three quarks, e.g. proton ( $uud$ ), while anti-baryons are composed of three anti-quarks. The mesons are bound states of quark and anti-quark pairs, e.g.  $\pi^+$  ( $u\bar{d}$ ) and  $\pi^-$  ( $\bar{u}d$ ). Baryons and Mesons together are also known as hadrons. Table 1.1 lists the fundamental fermions and some of their important properties [60].

Generation	Leptons (spin = $\frac{1}{2}$ )			Quarks (spin = $\frac{1}{2}$ )		
	Flavor	Charge	Mass (MeV/c <sup>2</sup> )	Flavor	Charge	Mass (MeV/c <sup>2</sup> )
1	$e$	-1	0.511	$u$	+2/3	$\sim 2.3$
	$\nu_e$	0	$< 2.2 \times 10^{-6}$	$d$	-1/3	$\sim 4.8$
2	$\mu$	-1	105.7	$c$	+2/3	$\sim 1.27 \times 10^3$
	$\nu_\mu$	0	$< 0.17$	$s$	-1/3	$\sim 95$
3	$\tau$	-1	1777	$t$	+2/3	$\sim 173.21 \times 10^3$
	$\nu_\tau$	0	$< 15.5$	$b$	-1/3	$\sim 4.18 \times 10^3$

Table 1.1: Three generation of elementary particles in the SM [60].

### 1.1.2 Forces of interactions

All fundamental particles and anti-particles represented within the SM, experience some force of interaction with other matter particles. The forces of interaction known up to now can be classified as - electromagnetic, weak, strong and gravitation. The fourth physical force, gravity, is not addressed in the SM. The carrier of these fundamental forces are particles with integral spin, termed as bosons. The SM is a gauge theory, in which the interactions are described by an invariance under ‘gauge’ transformations. The term ‘gauge’ refers to the redundant degrees of freedom that exist in the Lagrangian. The quantum of electromagnetic force is photon. The weak force is mediated by the  $W^\pm$  and

$Z^0$  bosons. The strong force is mediated by 8 colored gluons. The important properties of the forces and their force-carriers are listed in Table 1.2 [60].

Force	Gauge Boson	Charge	Spin	Mass (GeV/c <sup>2</sup> )	Range
Strong	Gluons ( $g$ )	0	1	0	$10^{-15}$ m
Electromagnetic	Photon ( $\gamma$ )	0	1	0	$\infty$
Weak	$W^\pm$	$\pm 1$	1	80.38	$10^{-15}$ m
	$Z^0$	0	1	91.18	
Higgs field	Higgs ( $H$ )	0	0	$\sim 125$	

Table 1.2: Fundamental forces, gauge bosons and scalar field [60].

### 1.1.2.1 Electromagnetic Interaction

The electromagnetic force is the unified form of electric and magnetic forces, achieved by Maxwell in 1864. The gauge invariance of Maxwell's equations and the corresponding abelian U(1) gauge symmetry [61] defines electromagnetism. The quantum approach to electromagnetic interactions is referred to as Quantum Electrodynamics (QED) [18, 19, 21–24, 62]. Electromagnetic interactions are responsible for most of the extra-nuclear phenomena. These interactions bind the electrons with the nuclei to form atoms. Electromagnetic interactions are mediated by photons. Since the photon is massless, the interactions are long range. The strength of the electromagnetic force, which can be parameterized by a coupling constant,

$$\alpha(Q^2) = \frac{\alpha(\mu^2)}{1 - \frac{\alpha(\mu^2)}{3\pi} \log\left(\frac{Q^2}{\mu^2}\right)}, \quad (1.1)$$

where  $\mu$  is the renormalization scale. The coupling strength increases as the interaction energy increases (or, as the interaction distance decreases).

### 1.1.2.2 Weak Interaction

The weak force is responsible for the radioactive  $\beta$ -decay of nuclei. These interactions are mediated by massive gauge bosons,  $W^\pm$ ,  $Z^0$ . As the force carriers are massive, these are

short range forces ( $\sim$ fm) and active only within the nuclear dimensions. Weak interaction is classified as charged or neutral, depending on whether a charged or a neutral boson mediates the reaction. It is called ‘weak’ because its strength is about four orders of magnitude less than the strength of the electromagnetic force. It must be noted that the strengths of these forces depend both on the coupling strengths of the gauge bosons to the fermions, and on the masses of the gauge bosons. At low energies, the high mass of the weak bosons reduces the effective strengths of the weak force, but at high energies where on-shell weak bosons can be exchanged, the weak force is actually stronger than the electromagnetic force. In the SM, electromagnetic and weak interactions have been unified in the Glashow-Salam-Weinberg (GSW) model [1–3], and is known as ‘Electroweak’ force.

### 1.1.2.3 Strong Interaction

The strong interaction is described by the theory of Quantum Chromodynamics (QCD). The ‘Chromo’ in the name comes from the fact that quarks and gluons possess color charge. It is responsible for interaction between color charged particles and particles with non-zero color charge can interact with each other via the exchange of gluons. It is a short range force responsible for binding quarks to form hadrons as well as binding proton and neutrons to form nuclei. Gluons come in eight color states composed of color and anti-color. The properties of the color charge is explained by  $SU(3)$  gauge symmetry.

Asymptotic freedom and confinement describes the short and long range behaviour of partons inside the nucleons. The strength of a QCD interaction can be measured in terms of its coupling strength [63], given by:

$$\alpha_s(Q^2) = \frac{12\pi}{(11c - 2n_f)\ln\left(\frac{Q^2}{\Lambda^2}\right)} \quad (1.2)$$

where  $Q$  is the momentum transferred in the interaction,  $c$  is the number of quark color (i.e. 3),  $n_f$  is the number of quark flavors (i.e. 6) and  $\Lambda$  is the chromodynamics scale,

given by:

$$\Lambda^2 = \mu^2 \left[ \frac{-12\pi}{(11c - 2n_f)\alpha_s(\mu^2)} \right] \quad (1.3)$$

where  $\mu$  is the renormalization scale. Using Eq 1.2, it can be seen that, as  $Q^2 \rightarrow \infty$  (distance  $\rightarrow 0$ ),  $\alpha_s(Q^2) \rightarrow 0$ . In simple words, as we go towards higher and higher energies with high momentum transfer during the interactions, i.e.  $Q^2 \gg \Lambda^2$ , the coupling strength between partons<sup>1</sup> tend to decrease making quarks and gluons behave as free entities inside the nucleus. This condition termed as “asymptotic freedom” [64–66]. On the contrary, at low values of  $Q^2$ , quarks and gluons restrict themselves into bound states, the quarks and gluons can no longer be observed in isolated state. They are seen as hadronic bound states of quarks (known as baryons and mesons as mentioned earlier) and this attribute of the strong force is called “quark confinement”.

### 1.1.3 Electroweak Unification and Higgs Mechanism

The electromagnetic and weak interactions are described by a unified gauge theory with  $SU(2)_L \times U(1)_Y$  local gauge symmetry group, as explained by S. Glashow, A. Salam, S. Weinberg [1–3].  $SU(2)_L$  is the weak isospin gauge group describing transformations of the left-handed isospin doublets, while  $U(1)_Y$  is the weak hypercharge group, which is essentially a phase transformation. The Lagrangian for the massless fermions and gauge bosons is given by:

$$\mathcal{L}_{EW} = \mathcal{L}_F + \mathcal{L}_G = \sum_f^{\text{family}=1,2,3} \left[ \bar{L}^f i\gamma^\mu D_\mu L^f + \bar{\ell}_R^f i\gamma^\mu D_\mu \ell_R^f + \bar{Q}^f i\gamma^\mu D_\mu Q^f + \bar{u}_R^f i\gamma^\mu D_\mu u_R^f + \bar{d}_R^f i\gamma^\mu D_\mu d_R^f \right] - \frac{1}{4} W_{\mu\nu}^a W_a^{\mu\nu} - \frac{1}{4} B_{\mu\nu} B^{\mu\nu} \quad (1.4)$$

---

<sup>1</sup>Quarks and gluons together are also referred as partons.

and the associated covariant derivative needed for gauge invariance,  $D_\mu$ , couples the fermions with the gauge boson and is given by:

$$D_\mu = \partial_\mu + ig \frac{T^a}{2} W_\mu^a + ig' \frac{Y}{2} B_\mu \quad (1.5)$$

where,  $g$  and  $g'$  are the gauge coupling constants for the  $SU(2)$  and  $U(1)$  symmetries, respectively, and  $T^a$ ,  $a = 1, 2, 3$  are the three generators of  $SU(2)$ . For left-handed fermions,  $T^a$  are given by Pauli matrices<sup>2</sup>  $\sigma^a$ , while for right-handed fermions they are zero ( $T^{1,2,3} = 0$ ).  $Y$  is the weak hypercharge and related to the electric charge  $Q$  and third component of the weak isospin  $T_3$  by Gell-Mann-Nishijima relation,  $Q = T_3 + \frac{Y}{2}$ .

In Eq 1.4,  $Q$  and  $L$  are  $SU(2)$  doublets for the left-handed quark and lepton fields, respectively.  $\ell_R$  refers to the right-handed leptons, while  $u_R$ ,  $d_R$  are the right-handed quark fields for the up type and down type quarks, respectively. The right-handed fields are singlets under  $SU(2)$ . Using electron as an example,

$$L = \begin{pmatrix} \nu_e \\ e^- \end{pmatrix}_L \quad \text{and} \quad e_R^-, \quad (1.6)$$

or with quarks,

$$Q = \begin{pmatrix} u \\ d \end{pmatrix}_L \quad \text{and} \quad u_R, d_R. \quad (1.7)$$

The three gauge fields  $W_\mu^a$  ( $a = 1, 2, 3$ ) are related to the three generators of the non-abelian  $SU(2)$  gauge group, which are represented by three Pauli matrices,  $\sigma^a$ . Non-abelian refers to the fact that the generators of  $SU(2)$  do not commute. The gauge field associated to the generator of the  $U(1)$  symmetry group is represented by  $B_\mu$ . The associated gauge fields are required to maintain the symmetry of the Lagrangian under

---

<sup>2</sup>Pauli matrices are set of three  $2 \times 2$  complex matrices which are Hermitian and unitary.

$\sigma_1 = \begin{pmatrix} 0 & 1 \\ 1 & 0 \end{pmatrix}$ ,  $\sigma_2 = \begin{pmatrix} 0 & -i \\ i & 0 \end{pmatrix}$ ,  $\sigma_3 = \begin{pmatrix} 1 & 0 \\ 0 & -1 \end{pmatrix}$ .

the local gauge transformations. The field strength tensors corresponding to these gauge fields are given by:

$$W_{\mu\nu}^a = \partial_\mu W_\nu^a - \partial_\nu W_\mu^a + g\epsilon^{abc}W_\mu^bW_\nu^c, \quad (1.8)$$

$$B_{\mu\nu} = \partial_\mu B_\nu - \partial_\nu B_\mu. \quad (1.9)$$

where  $\epsilon^{abc}$  is the completely anti-symmetric tensor of rank 2.

The charged fields  $W_\mu^\pm$ , are the linear combinations of the  $W_\mu^a$  gauge fields:

$$W_\mu^\pm = \frac{1}{\sqrt{2}}(W_\mu^1 \mp iW_\mu^2), \quad (1.10)$$

while the neutral fields,  $A_\mu$  and  $Z_\mu$ , observed as the photon and  $Z$  boson are combinations of the  $B_\mu$  and  $W_\mu^3$  fields:

$$A_\mu = \frac{gB_\mu + g'W_\mu^3}{\sqrt{g^2 + g'^2}}, \quad (1.11)$$

$$Z_\mu = \frac{-g'B_\mu + gW_\mu^3}{\sqrt{g^2 + g'^2}} \quad (1.12)$$

These can also be parameterized in terms of the Weinberg (or weak mixing) angle,  $\theta_W$ , where,

$$\sin \theta_W = \frac{g}{\sqrt{g^2 + g'^2}}; \quad \cos \theta_W = \frac{g'}{\sqrt{g^2 + g'^2}} \quad (1.13)$$

such that:

$$\begin{pmatrix} A_\mu \\ Z_\mu \end{pmatrix} = \begin{pmatrix} \cos \theta_W & \sin \theta_W \\ -\sin \theta_W & \cos \theta_W \end{pmatrix} \begin{pmatrix} B_\mu \\ W_\mu^3 \end{pmatrix} \quad (1.14)$$

Notably, it relates the coupling strengths  $g$  and  $g'$  with the more familiar QED charge:

$$g = \frac{e}{\sin \theta_W}; \quad \frac{g}{g'} = \frac{\sin \theta_W}{\cos \theta_W} \quad (1.15)$$

The SM Lagrangian presented so far does not include a mass term, which is in clear disagreement with the experimental observation that, except for the photon and gluons, fermions and bosons are found to be massive. Adding an explicit mass term, invariant under  $SU(3)$  transformations would break the  $SU(2)$  symmetry. This is the crucial point in the electroweak theory that is addressed by the Higgs mechanism [41–44].

The Higgs mechanism proposed a way to generate mass terms for the vector gauge bosons without explicitly breaking the  $SU(2) \times U(1)$  gauge invariance of the Lagrangian. A scalar field, the Higgs field, with a specific potential is introduced in the model. It is a complex  $SU(2)$  doublet, with  $Y = 1$  under  $U(1)_Y$ , and is colorless. The potential has a non-zero ground state, and its vacuum expectation value (*vev*) breaks the  $SU(2)_L \times U(1)_Y$  electroweak symmetry spontaneously, yielding massless (Goldstone) bosons, which are immediately absorbed by the (unstable massless)  $W$  and  $Z$  bosons to appear as longitudinal polarization mode of the now massive  $W/Z$ . The remaining degree of freedom yields a massive scalar, called the Higgs boson. A detailed review of electroweak symmetry breaking can be found in Ref [67].

In the  $SU(2) \times U(1)$  case of the SM, one needs to generate mass terms for the three gauge bosons  $W^\pm$  and  $Z$  and a massless photon. So, at least three degrees of freedom for the scalar fields is needed. The simplest choice would be to use a isovector state with exactly three scalar fields, but such a configuration lacks a massless field. Hence, to illustrate the main idea of the spontaneous symmetry breaking, two complex scalar fields,  $\phi^+$  and  $\phi^0$ , that form an isospin doublet are considered, viz,

$$\Phi = \begin{pmatrix} \phi^+ \\ \phi^0 \end{pmatrix} = \frac{1}{\sqrt{2}} \begin{pmatrix} \phi_1 + i\phi_2 \\ \phi_3 + i\phi_4 \end{pmatrix}. \quad (1.16)$$

The Lagrangian for the Higgs field with mass term and four-point vertex (using the same covariant derivative  $D_\mu$  as in Eq 1.5 is given by:

$$\mathcal{L} = (D_\mu \Phi)^\dagger D^\mu \Phi - \mu^2 \Phi^\dagger \Phi - \lambda (\Phi^\dagger \Phi)^2 \quad (1.17)$$

For all values of  $\mu^2$  and  $\lambda$ , the Lagrangian of Eq 1.17 respects the  $SU(2) \times U(1)$  gauge symmetry. The shape of the potential depends on the choice of the parameters  $\mu^2$  and  $\lambda$ . The quartic coupling  $\lambda$  must be positive to ensure the stability of the vacuum so that the potential is bounded from below. So, we have two cases for  $\mu^2$ , viz.  $\mu^2 > 0$  and  $\mu^2 < 0$ . For  $\mu^2 > 0$ , the potential has a minimum at zero, i.e., the *vev* of  $\Phi$  is zero. However, for  $\mu^2 < 0$ , the ground state no longer corresponds  $\Phi = 0$ , but rather to a finite value  $\Phi^\dagger \Phi = \frac{-\mu^2}{2\lambda} = \frac{v^2}{2}$ , where  $v$  is the *vev* of the Higgs field. A example of the potential with a real scalar field is shown in Fig 1.1.

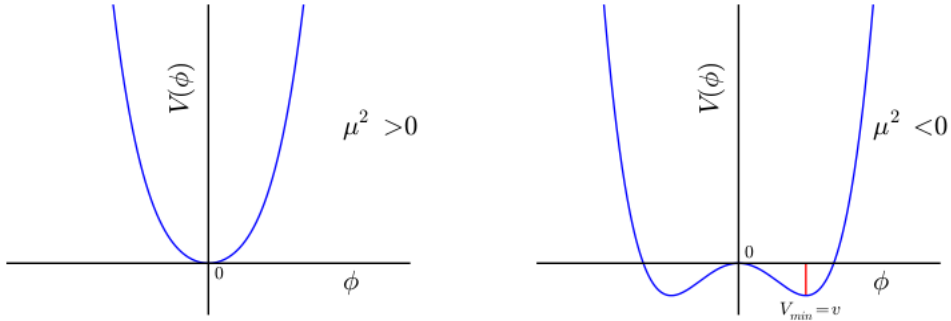


Figure 1.1: Example of electroweak symmetry breaking for the potential with real scalar,  $V(\phi) = \mu^2\phi^2 + \phi^4$ . The ground state for  $\mu^2 < 0$  no longer respect the symmetry  $\phi \rightarrow -\phi$ .

By chosing a particular ground state, the symmetry is broken spontaneously. As we need to keep the  $U(1)$  symmetry of electromagnetism, we choose the configuration where the expectation value of the charged Higgs-field vanishes, and ground state can be written as:

$$\Phi \equiv \langle \Phi_0 \rangle = \frac{1}{\sqrt{2}} \begin{pmatrix} 0 \\ v \end{pmatrix}, \quad v = \frac{\mu}{\sqrt{\lambda}} \quad (1.18)$$

We have chosen  $\phi_3 = v$  and  $\phi_1 = \phi_2 = \phi_4 = 0$ , a direction in  $SU(2)$  space. Now, considering a small perturbation to investigate the excitation of the field,

$$\Phi(x) = \frac{1}{\sqrt{2}} \begin{pmatrix} 0 \\ v + h(x) \end{pmatrix} \quad (1.19)$$

Using relations in Eq 1.12 and Eq 1.5, and solving for the kinetic term of the Lagrangian

we get,

$$|D_\mu \Phi|^2 = \frac{1}{2}(\partial_\mu h)^2 + \frac{1}{4}g'^2(v+h)^2(W_\mu^+W^{\mu-}) + \frac{1}{8}(g^2+g'^2)(v+h)^2Z_\mu Z^\mu \quad (1.20)$$

Finally, the Higgs mechanism breaks the symmetry, and generates the mass terms for the bosons weak field. The mass terms for the gauge bosons at the leading order sare:

$$m_\gamma = 0, \quad m_{W^\pm} = \frac{vg}{2}, \quad \text{and} \quad m_Z = \frac{1}{2}v\sqrt{g^2+g'^2} \quad (1.21)$$

where we have the relation  $m_W/m_Z = \cos\theta_W$ . A measurement of all the three parameters, mass of  $W$ , mass of  $Z$  and  $\cos\theta_W$ , allows the testing of SM predictions. We also get a real Goldstone boson,  $h$ , which is identified as the Higgs boson.

Plugging in the expansion around the *vev* into the potentio of the Lagrangian in Eq 1.17,

$$\mathcal{L} = -\lambda v^2 h^2 - \lambda v h^3 - \frac{\lambda}{4} h^4 \quad (1.22)$$

leads to a three-point, four-point Higgs boson vertex, and mass term where,  $m_h = \sqrt{2\lambda v^2}$ . The parameter  $\mu$  which defines the Higgs boson mass cannot be predicted by the theory. The recently discovered new boson at the Large Hadron Collider [50,51], which is a strong candidate for Higgs boson and has a mass of roughly 125 GeV, fixes the value of  $\mu$ .

Fermionic mass terms can also be generated using the same complex scalar doublet by adding Yukawa couplings to the Higgs field in the Lagrangian:

$$\mathcal{L}_{Yukawa} = \sum_f^{\text{family}=1,2,3} \left[ -y_\ell \bar{L} \Phi e_R - y_d \bar{Q} \Phi d_R - y_u \bar{Q} (-i\sigma_2) \Phi^* u_R + h.c. \right] \quad (1.23)$$

where  $u_R$ ,  $d_R$  ( $e_R$ ) are the quark (lepton)  $SU(2)_L$  doublets and singlets. The constants  $y_{\ell,d,u}$  are the free parameters of the model. After breaking the electroweak symmetry, these terms become:

$$\mathcal{L}_{Yukawa} = \sum_f^{\text{family}=1,2,3} \left[ -\frac{1}{\sqrt{2}} y_\ell \bar{\ell}_L (v+h) \ell_R - \frac{1}{\sqrt{2}} y_q \bar{q}_L (v+h) q_R \right], \quad (1.24)$$

such that the masses of the fermions are  $m_f = y_f v / \sqrt{2}$ . There are also terms with  $h \bar{f}_L f_R$  interactions with coupling strength proportional to the fermion masses.

## 1.2 Beyond the Standard Model

The SM of particle physics is one of the most successful theories in physics. It has passed all the tests and has been verified experimentally with tremendous precision. One of its latest triumphs is the discovery of a new boson [50, 51], which to date appears to be the Higgs boson as predicted by the SM. Despite the success SM has achieved, there are reasons to believe that it is far from the ultimate theory to explain the fundamental particles and their interactions. Some of the prominent issues that SM fail to address and motivates physicist to look beyond are listed below :

- Neutrinos are treated as massless particles within the SM<sup>3</sup>, but there have been experimental observations [54, 55, 57, 59] which suggests that they do have a non-vanishing mass.
- The SM gives no explanation for the large difference in the strength of fundamental forces. Also, the theory gives no reason for the wide range of masses for different SM particles.
- There is no explanation within the SM which may address the fact that there are three generations of fundamental fermions.
- The SM does not explain the asymmetry between the matter and antimatter required to get all of the observed baryonic matter in the universe.
- Finally, the cosmological and astrophysical observations concluded that the observed matter account for only about 5% of the energy and mass content of the universe. About 25% is attributed to the non-luminous dark matter and the remaining 70%

---

<sup>3</sup> $\nu_R$  are absent in Weinberg's paper [3] as there was no evidence for neutrino mass by that time.

are dark energy [68]. None of these last two issues find any explanation within the SM.

### 1.2.1 The Excited Quark Model

Physicists have come up with different ideas/models to address the questions that the standard model fails to answer. One of the directions which may shed light on some of these unanswered questions is the idea of quark compositeness, which suggests that quarks may not be fundamental particles but are composite entities of more fundamental particles (often referred to as “preons”) [69–72]. Simple motivation which makes us think towards this path comes from the historical developments, where we have always found something new when probed with higher energies.

Matter → Molecules → Atom → Nucleons → quarks/leptons → **What Next ???**

With the LHC<sup>4</sup> colliding protons at a center-of-mass energy of 8 TeV, the hunt for the more fundamental constituent if it exists, is still on. The SM does not give any insight to the wide range of fermion masses nor does it explain the replication of fermion families, as stated in earlier section. This has led to the speculation that quarks and leptons are not elementary particles but are composite objects. If compositeness of fermion exists, it may also proffer to explain parameters like particle mass, charge, which the SM had failed to explain.

The most compelling sign for substructure of quarks would be the discovery of an excited state of a quark, which we denote by  $q^*$ . To supplement the belief that compositeness would lead to an excited state, a simple analogy is considered. We know that the excited states of known particles are common in nature, for example, the excited state of hydrogen atom. Hydrogen atom in its ground state absorbs a photon and goes to its excited states. The excited hydrogen atom then radiates photons to reach to its ground state. Likewise, if quarks have sub-structure, we expect them to exhibit excited states. A gluon interaction could excite a quark and while returning to ground state, they would

---

<sup>4</sup>Large Hadron Collider, more details mentioned in Chapter 2

radiate either a photon or a gluon.

The preons, if exists, would experience an unknown force due to an asymptotically free but confining gauge interaction, which becomes very strong at a characteristic scale  $\Lambda$  also referred to as compositeness scale, forming bound states, that we see as quarks. Excited quarks may couple to ordinary quarks and leptons via contact interactions resulting from strong preon interactions for  $\Lambda \gg \sqrt{\hat{s}}$ . For  $\Lambda < \sqrt{\hat{s}}$ , excited quarks can be produced on-shell via gauge mediation. In this study, it is assumed that the LHC energy is larger than the compositeness scale,  $\Lambda$  and excited quark states have a mass scale comparable to that of the dynamics of the new binding force, i.e.,  $M_{q^*} = \Lambda$ . While we expect  $M_{q^*} \leq \Lambda$ , the equality has been assumed essentially to reduce the number of unknown parameters.

The simplest excited quark model [72] used in this study assumes the excited quarks to have both spin and isospin 1/2 and have their left- and right-handed components in weak isodoublets. The coupling of excited quarks,  $q^*$  to gluons,  $\gamma$ ,  $W^\pm$  and  $Z$  is vectorlike and is given by the Lagrangian [72],

$$\mathcal{L}_{gauge} = \bar{q}^* \gamma^\mu \left[ g_s \frac{\lambda^a}{2} G_\mu^a + g \frac{\tau}{2} W_\mu + g' \frac{Y}{2} B_\mu \right] q^* \quad (1.25)$$

where,  $g_s$ ,  $g = \frac{e}{\sin\theta_W}$  and  $g' = \frac{e}{\cos\theta_W}$  are the strong and electroweak gauge coupling constants;  $G_\mu^a$ ,  $W_\mu$ ,  $B_\mu$  describe the gluon,  $SU(2)$ , and  $U(1)$  gauge fields;  $Y$  is the weak hypercharge of excited states of quark with a value of 1/3. Assuming the mass of excited quarks to be of the order of  $\Lambda$ , the transition between the excited state (right-handed) and the ground state (left-handed) of quarks is constrained by gauge invariance and is given by an effective Lagrangian of the magnetic-moment type,

$$\mathcal{L}_{int} = \frac{1}{2\Lambda} \bar{q}_R^* \sigma^{\mu\nu} \left[ g_s f_s \frac{\lambda_a}{2} G_{\mu\nu}^a + g f \frac{\tau}{2} W_{\mu\nu} + g' f' \frac{Y}{2} B_{\mu\nu} \right] q_L + h.c., \quad (1.26)$$

where  $G_{\mu\nu}^a$ ,  $W_{\mu\nu}$  and  $B_{\mu\nu}$  are the field-strength tensors of the  $SU(3)$ ,  $SU(2)$  and  $U(1)$  gauge fields, respectively. The quantities  $\lambda_a$ ,  $\tau$ ,  $Y$  ( $g_s$ ,  $g$ ,  $g'$ ) are the corresponding generators (gauge coupling constants).  $\Lambda$  denotes the typical scale of these interactions. The un-

known dimensionless constants  $f_s$ ,  $f$ ,  $f'$  are determined by the dynamics of compositeness and are assumed to be of order unity.

In proton-proton collisions, excited quarks could be produced at the tree level predominantly by quark gluon scattering(Fig 1.2a), and then by quark anti-quark annihilation (Fig 1.2b). At the loop level, they would show their presence in gluon gluon fusion (Fig 1.2c). The loop level diagram is not considered in the study as its contribution would presumably be significantly smaller as compared to the tree level diagrams to have any meaningful effect on our analysis. The excited quark  $q^*$  then decays into a

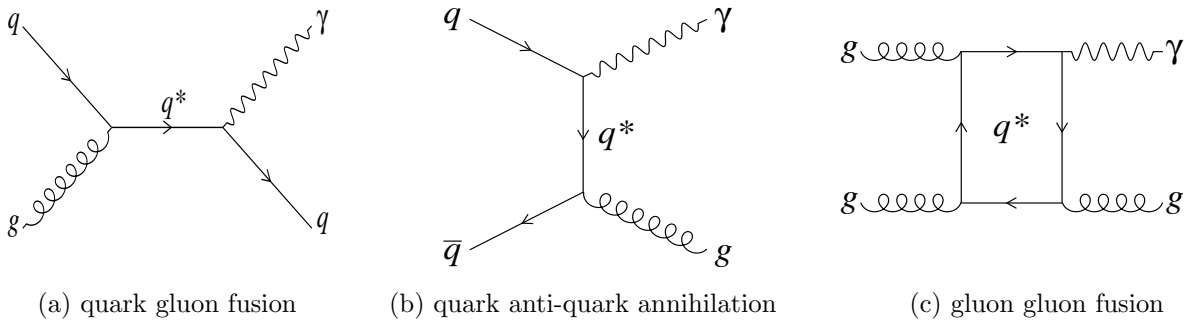


Figure 1.2: Some of the Feynman diagrams for  $pp \rightarrow q^* \rightarrow \gamma + \text{jet}$  final state.

ground-state quark and a gauge boson ( $g$ ,  $W$ ,  $Z$ ,  $\gamma$ ). Using Eq 1.26, assuming  $M_{q^*} > M_V$  ( $V = W^\pm, Z^0$ ) and neglecting the ground-state quark masses, the partial widths for various channels are given by,

$$\Gamma(q^* \rightarrow qg) = \frac{1}{3} \alpha_s f_s^2 \frac{M_{q^*}^2}{\Lambda^2}, \quad (1.27)$$

$$\Gamma(q^* \rightarrow q\gamma) = \frac{1}{4} \alpha f_\gamma^2 \frac{M_{q^*}^3}{\Lambda^2}, \quad (1.28)$$

$$\Gamma(q^* \rightarrow qV) = \frac{1}{8} \frac{g_V^2}{4\pi} f_V^2 \frac{M_{q^*}^3}{\Lambda^2} \left(1 - \frac{M_V^2}{M_{q^*}^2}\right) \left(2 + \frac{M_V^2}{M_{q^*}^2}\right), \quad (1.29)$$

with

$$f_\gamma = fT_3 + f'\frac{Y}{2}, \quad (1.30)$$

$$f_Z = fT_3\cos^2\theta_W - f'\frac{Y}{2}\sin^2\theta_W, \quad (1.31)$$

$$f_W = \frac{f}{\sqrt{2}} \quad (1.32)$$

where  $T_3$  is the third component of the weak isospin. Setting the compositeness scale  $\Lambda$  to be the  $q^*$  mass and assuming the SM coupling, i.e.,  $\Lambda = M_{q^*}$  and  $f_s = f = f' = 1$ , Table 1.3 shows the numerical values of the relative branching ratios of the  $q^*$ . The  $q^*$  final states are large transverse momentum jet-jet,  $\gamma$ -jet,  $Z^0$ -jet or  $W^\pm$ -jet pairs.

Decay Channel	BR	Decay Channel	BR
$u^* \rightarrow ug$	83.4%	$d^* \rightarrow dg$	83.4%
$u^* \rightarrow u\gamma$	2.27%	$d^* \rightarrow d\gamma$	0.57%
$u^* \rightarrow uZ^0$	3.39%	$d^* \rightarrow dZ^0$	5.07%
$u^* \rightarrow dW^-$	10.9%	$d^* \rightarrow uW^+$	10.9%

Table 1.3: The branching ratios (BR) of various decay channels of the  $q^*$  ( $u^*$ ,  $d^*$ ) of mass  $M_{q^*} = 1$  TeV.

In this study, we present a search for excited quark in the photon + jet final state. An encouraging fact for the present work is that the background processes for  $q^* \rightarrow \gamma + \text{jet}$  are well understood both theoretically as well as experimentally. It is assumed throughout the study that the compositeness scale  $\Lambda$  is less than the LHC center-of-mass energy and gauge interactions dominate over contact interactions. For  $\Lambda$  smaller than the LHC center-of-mass energy, excited quarks are produced dominantly through s-channel processes. The s-channel quark gluon scattering of excited quarks would give a resonance over the SM continuum in the  $\gamma + \text{jet}$  invariant mass distribution peaking at  $M_{\gamma j} = M_{q^*}$  while all other modes would give excess of events over the continuum prediction. The SM result will be recovered in the limit  $\Lambda \rightarrow \infty$  which also implies that higher the compositeness scale  $\Lambda$ , harder it is to observe the signal for new physics.

### 1.2.1.1 A Summary of Previous Searches

Searches for quark compositeness have been performed by various experiments of different generations at different energies and in several decay channels with no success. A summary of results from these experiments is reported in this section.

The ZEUS detector at the HERA experiment searched for heavy excited states of quarks in  $e^+p$  collisions at a center-of-mass energy of 300 GeV with an integrated luminosity of  $9.4 \text{ pb}^{-1}$  and excluded, at 95% confidence level, excited quarks with mass between 40 and 169 GeV [73]. The H1 detector at the same experiment also performed searches in various decay channels, but with a lower integrated luminosity ( $37 \text{ pb}^{-1}$ ) and reported the results in Ref. [74].

The CDF collaboration at the Tevatron experiment searched for excited quarks in the  $\gamma + \text{jet}$  and dijet decay channels in  $p\bar{p}$  collisions at  $\sqrt{s} = 1.8 \text{ TeV}$  and excluded the mass range of  $80 < M_{q^*} < 540 \text{ GeV}$  [75] and  $200 < M_{q^*} < 520 \text{ GeV} \& 580 < M_{q^*} < 760 \text{ GeV}$  [76], respectively, with 95% confidence level. The D0 collaboration at the Tevatron experiment searched in the dijet final state only [77] and excluded masses below 775 GeV at 95% confidence level. The ATLAS collaboration at the LHC experiment excluded excited quarks below 4.06 TeV with 95% confidence level in the dijet decay channel [78] in  $pp$  collisions at  $\sqrt{s} = 8 \text{ TeV}$  and below 3.5 TeV in the  $\gamma + \text{jet}$  decay channel [79]. The CMS collaboration at the LHC experiment has also excluded excited quarks below 3.19 TeV in the dijet final state with 95% CL in  $pp$  collisions at  $\sqrt{s} = 8 \text{ TeV}$  [80].

# Chapter 2

## The Experimental Apparatus

The Large Hadron Collider (LHC) [81,82] is the world's highest energy particle accelerator and collider, situated at the European Organization for Nuclear Research (CERN), on the French-Swiss border near Geneva, Switzerland. The Compact Muon Solenoid (CMS) [83] experiment is one of the two general purpose detectors that measures the properties of particles produced from proton-proton (pp) and heavy-ion collisions at the LHC. This chapter briefly describes the details of the design and performance of the CERN accelerator complex and the CMS experiment.

### 2.1 The Large Hadron Collider

In the last few decades, the standard model of particle physics has been tested experimentally to excellent precision and is a well established theory explaining the interactions of the fundamental particles. Many of these precise measurements were carried out at the Large Electron-Positron (LEP) collider at CERN. As suggested by the de Broglie relation,  $\Delta E \cdot \Delta x \simeq \hbar$ , to probe increasingly smaller constituents, higher and higher energy is required. The maximum energy that can be attained by a particle orbiting in a circular path is limited by the energy loss due to synchrotron radiations given by

$$-\Delta E = \frac{4\pi\alpha}{3r} \beta^3 \gamma^4 \quad (2.1)$$

where  $r$  is the radius of circular path,  $\beta = v/c \approx 1$ , as particles travel with velocity very close to the speed of light and  $\gamma = E/mc^2$  with  $m$  being mass of the accelerated particles. This synchrotron effect can be reduced either by increasing the radius of the collider (a linear one would be optimal) or by using heavier particles. For financial reasons, there was a strong motivation to re-use the the LEP tunnel. Thus, according to Eq 2.1, the other efficient way to increase center-of-mass energy is to increase the mass of the accelerated particles, i.e., protons for LHC. Since the rest mass of protons is about 2000 times more than the rest mass of electrons, the energy loss due to synchrotron radiation for protons is decreased by a factor of  $(2000)^4 \approx 10^{13}$  compared to that of electrons. The LHC is also designed to include the heavy ion collisions but the differences in proton and ion beams on various aspects limit the luminosity and beam lifetime [82].

As protons are not elementary particles but have a sub-structure, pp collision phenomenology is very different from lepton collisions. A proton is made up of constituent partons – quarks and gluons, with a given constituent carrying only a fraction of the total proton energy. In a collision, typically only one each of the parton are engaged in a hard scattering process with the effective center-of-mass energy of the hard scattering,  $\sqrt{\hat{s}}$ , being determined by the momentum fractions  $x_1, x_2$  carried by partons, and given by  $\sqrt{\hat{s}} = \sqrt{x_1 x_2 s}$ , where  $\sqrt{s}$  is the center-of-mass energy of proton beams. In each proton-proton collision there is a probability to produce different process depending on its cross section and momentum exchange between the colliding partons.

The LHC [81,82] is a two ring superconducting accelerator and collider, located in the 27 km circular underground tunnel originally built for the LEP collider on the French-Swiss border. The tunnel has a diameter of 3.7 m and the depth varies between 50 m and 175 m (according to the land topology). It houses a twin-bore magnet which provides a magnetic field to both the proton beams in the same structure. To keep the proton beams on track, a magnetic field of 8.3 T is needed, which is achieved by using superconducting dipole magnets operating at a temperature of 1.9° K. About 37 million Kg of superfluid Helium is used to cool the Niobium-Titanium windings of the magnets to reach the superconducting

state. The LHC has 1232 dipole magnets each of which weights 30 tonnes and is 15 m long. The LHC is also installed with eight Radio Frequency (RF) cavities for each beam to correct for the synchrotron radiation losses. These cavities operate at 4.5° K, with each cavity delivering 2 MV at 400 MHz.

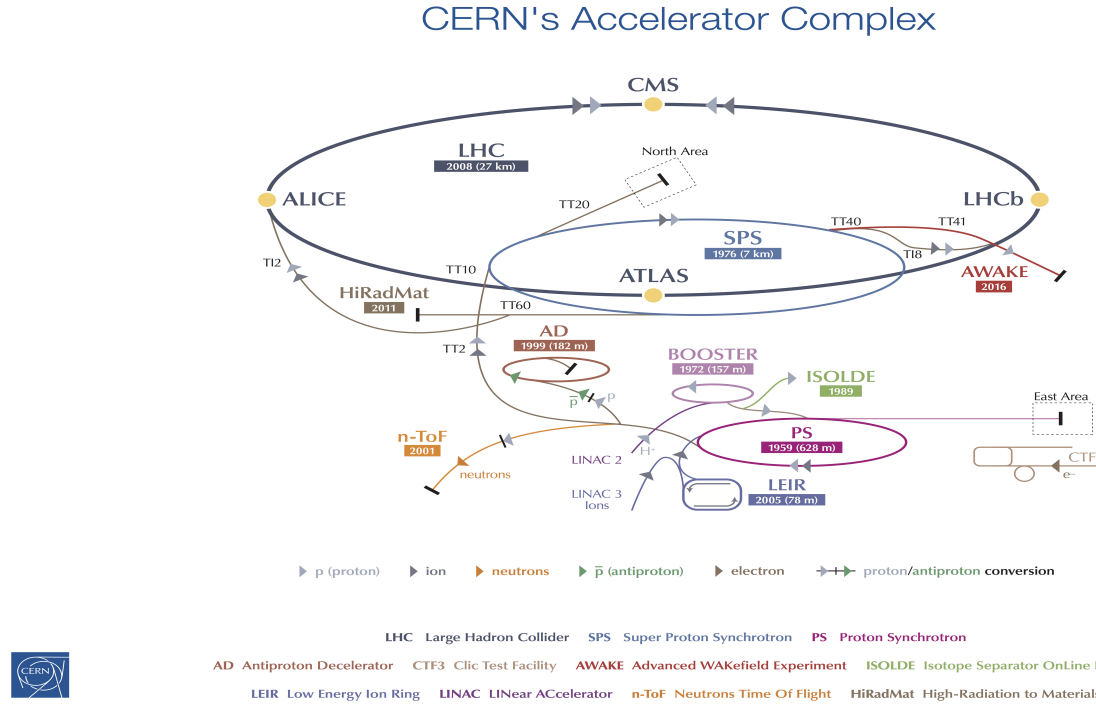


Figure 2.1: Picture showing the LHC ring and a series of accelerators which boost the proton (ion) beam to different energy levels [84].

Before two proton beams collide in the LHC at the desired center-of-mass energy, the beams have to be accelerated in several steps, as with the presently available resources, it is experimentally challenging to reach an energy of 4 TeV (or designed 7 TeV) per beam in a single step. Protons are first accumulated using hydrogen atoms contained in a simple bottle of hydrogen gas after stripping off electrons by applying an electric field. Protons are then accelerated in LINAC2, a linear accelerator consisting of RF cavities, to an energy of 50 MeV. These are then transferred to the Proton Synchrotron Booster (PSB), which accelerates the beam to 1.4 GeV. Then the proton beams are accelerated up to 25 GeV in the Proton Synchrotron (PS) and up to 450 GeV in the Super Proton Synchrotron (SPS). Finally, these are injected into the LHC rings and accelerated to an energy of 4 TeV

resulting in a center-of-mass energy of 8 TeV. The entire CERN accelerator complex houses several experiments and facilities as illustrated in Fig 2.1. Details of these can be found in Ref. [84].

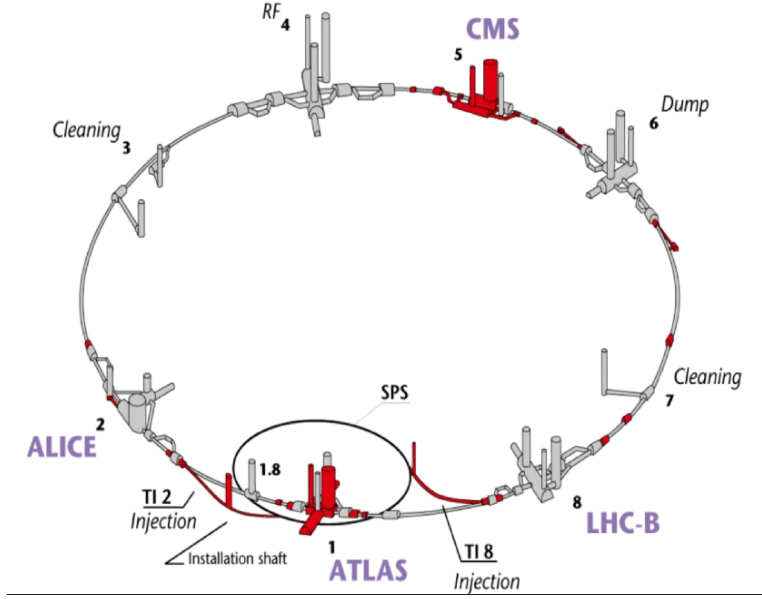


Figure 2.2: Layout of LHC ring [85].

The LHC tunnel is geometrically organized in eight crossing points, flanked by eight straight sections, and arcs. Each straight section has a length of 528 m and can serve as an experimental insertion, a point where two beams travelling in opposite directions can collide. A schematic representation of the LHC tunnel is depicted in Fig 2.2. The insertion points are labeled with integer numbers increasing in counter-clockwise direction. The LHC hosts four major detectors. A Toroidal LHC ApparatuS (ATLAS) [86] and Compact Muon Solenoid (CMS) [87] are the two general purpose detectors situated at points 1 and 5 insertion regions respectively. At point 2 and 8 lie respectively, the experiments, A Large Ion Collider Experiment (ALICE) [88] and Large Hadron Collider beauty (LHCb) [89]. These two points also serve as the injection system for both the beams, one for the beam in clockwise direction and other for the beam in the counter-clockwise direction. Point 3 and 7 houses the collimation system while point 4 has two resonant frequency (RF) cavity system, one for each beam. Collimation system involves efficient cleaning of the beam halo during the LHC beam cycle, which limits the beam lifetime [90]. Point 6 is used as

beam dump, where the beams are vertically extracted from the machine using horizontally deflecting kicker magnets and vertically deflecting double steel septum<sup>1</sup> magnets.

The LHC is designed to reach a center-of-mass energy up to 14 TeV. For any physics process the number of events generated by LHC collision is given by

$$N = \mathcal{L}\sigma, \quad (2.2)$$

where  $\mathcal{L}$  is the instantaneous machine luminosity and  $\sigma$  is the production cross section for a specific process. Assuming a Gaussian distributed beam in the  $x$ - $y$  plane, the machine instantaneous luminosity depends on various beam parameters, given by,

$$\mathcal{L} = F \frac{N_b^2 n_b f_{rev} \gamma_r}{4\pi \epsilon_n \beta^*} \quad (2.3)$$

where  $N_b$  is the number of particles in each bunch,  $n_b$  is the number of colliding bunches for each beam,  $f_{rev}$  is the revolution frequency,  $\gamma_r$  is the relativistic gamma factor,  $\epsilon_n$  is the normalized transverse beam emittance, defined as the smallest opening the beams can be squeezed through. A low emittance beam implies that the particles are confined to a very small phase space thus having the likelihood of higher particle interaction.  $\beta^*$  is referred as the distance from the focus point where the beam width is twice as much to that at the focus point.  $F$  is the geometrical reduction factor due to the non-zero beam crossing angle at the interaction point (IP), and is defined as,

$$F = \left( 1 + \left( \frac{\theta_c \sigma_z}{2\sigma^*} \right) \right) \quad (2.4)$$

where,  $\theta_c$  is the crossing angle at the IP,  $\sigma_z$  is the rms bunch length, and  $\sigma^*$  is the transverse rms beam size at the IP.

It takes the protons about  $89\mu s$  to circulate once in the LHC beam pipe. The LHC ring can accommodate a maximum of 2808 proton bunches with a spacing of 25 ns and the rms

---

<sup>1</sup>Septum magnets are modified Lambertson-type septa with an all welded construction. More details about these can be found in Ref. [82]

beam size at the IP5 is  $16.7\mu\text{m}$ . In 2012, the LHC operated with 1380 bunches spaced at 50 ns each and containing up to  $1.7\times 10^{11}$  protons at an energy of 4.0 TeV. The 2012 proton-proton (pp) collision parameters  $\epsilon_n$ ,  $\beta^*$  and  $F$  at the CMS interaction point were  $2.5\mu\text{m}$ ,  $0.6\text{ m}$ , and  $0.8$ , respectively, yielding a peak instantaneous luminosity of  $7.7\times 10^{33}\text{ cm}^{-2}\text{s}^{-1}$ . These parameters were optimized to give a high instantaneous luminosity and a stable beam with a long life time. It was difficult to further increase the instantaneous luminosity beyond a certain point as maximum particle density per bunch is limited by the non-linear beam-beam interactions when the bunches of two beams collide with each other. Also, the mechanical aperture of the magnets limits the minimum value that  $\beta^*$  can attain at the IPs and the maximum value crossing angle can take in the experimental interaction regions. During the 8 TeV run in 2012, the LHC delivered an integrated luminosity of  $23.3\text{ fb}^{-1}$  of pp collision data to the ATLAS and CMS experiments, of which  $21.8\text{ fb}^{-1}$  were recorded<sup>2</sup> by the CMS detector and  $19.7\text{ fb}^{-1}$  was certified to be good for the physics analysis. The time-evolution of the total integrated delivered and recorded luminosities, during the 8 TeV run, is illustrated in Fig 2.3. This thesis is based on  $19.7\text{ fb}^{-1}$  of pp data collected by CMS detector in 2012.

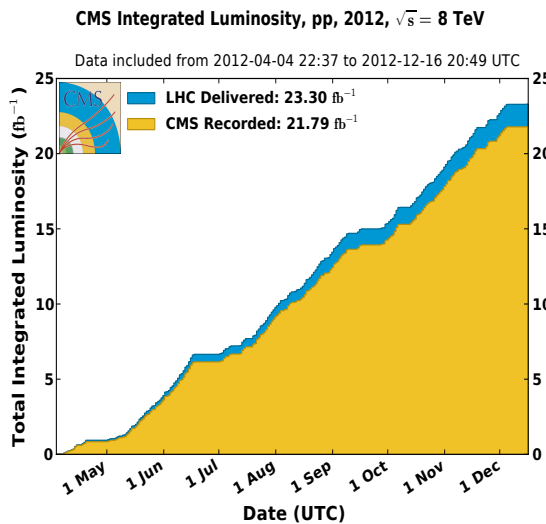


Figure 2.3: Total integrated luminosity delivered to the CMS experiment for pp collisions by the LHC during the 2012 run at  $\sqrt{s} = 8\text{ TeV}$  [91].

<sup>2</sup>During data taking, at times a sub-detector goes into error state due to several reasons and the data taking has to be stopped to take the sub-detector out and start a new run. Such situations lead to losses in the recorded data when compared to the delivered data.

## 2.2 The Compact Muon Solenoid

The Compact Muon Solenoid (CMS) experiment [83] consists of a multi purpose  $4\pi$  steridian detector and is installed at point 5 of the LHC ring, near the village Cessy in France.

As mentioned in the previous section, the LHC is designed to collide proton beams at  $\sqrt{s} = 14 \text{ TeV}$ , with an instantaneous luminosity of  $10^{34} \text{ cm}^{-2}\text{s}^{-1}$ . The large pp total cross section, high beam intensity and short bunch spacing pose very challenging requirements on the detectors in terms of radiation tolerance, high granularity, time-resolution and online data reduction. The conceptual design of the CMS detector was geared towards the detection of the SM Higgs boson and search for new particles, which led to excellent reconstruction efficiencies and energy resolutions for electrons, muons, photons, and hadrons [87]. The requirements for the CMS detector to meet the goals of the LHC physics program, coping with the demanding environmental conditions can be summarized as follows:

- Good identification and momentum resolution of muons over a wide range of momenta in the barrel region ( $|\eta| < 2.5$ ), and a good dimuon mass resolution ( $\sim 1\%$  at  $100 \text{ GeV}/c^2$ ), and the ability to determine the charge of muons with  $p_T < 1 \text{ TeV}/c$ .
- A tracker system with an excellent charged particle momentum resolution and reconstruction efficiency. The pixel detector is placed close to the interaction region for efficient triggering and offline tagging of  $\tau$ 's and  $b$ -jets.
- An electromagnetic calorimeter with a good energy resolution and a good mass resolution ( $\sim 1\%$  at  $100 \text{ GeV}/c^2$ ) for diphoton and dielectron final states. It was also designed to be efficient in  $\pi^0$  rejection, and isolation of photons and leptons at high luminosities.
- Good  $E_T^{\text{miss}}\text{<sup>3</sup>}$  and dijet mass resolution, requiring hadron calorimeters with a hermetic geometric coverage and with fine lateral segmentation.

---

<sup>3</sup> $E_T^{\text{miss}}$  is referred to as the missing transverse momentum and is defined in Section 2.2.1

The design of the CMS detector is similar to the structure of an onion. It consists of several layers of detectors, each one specially designed and optimized to measure and identify different classes of particles. The main feature of the CMS experiment is a 3.8 T superconducting solenoid magnet. Within the field volume are the tracker system, electromagnetic calorimeter, and hadronic calorimeter. A muon detection system is placed outside the field volume of the solenoidal magnetic field embedded inside iron yoke and having return field for muon momentum measurement. A schematic view of the detector system is shown in Fig 2.4. In the following sections, the different components of the CMS detector are described in detail.

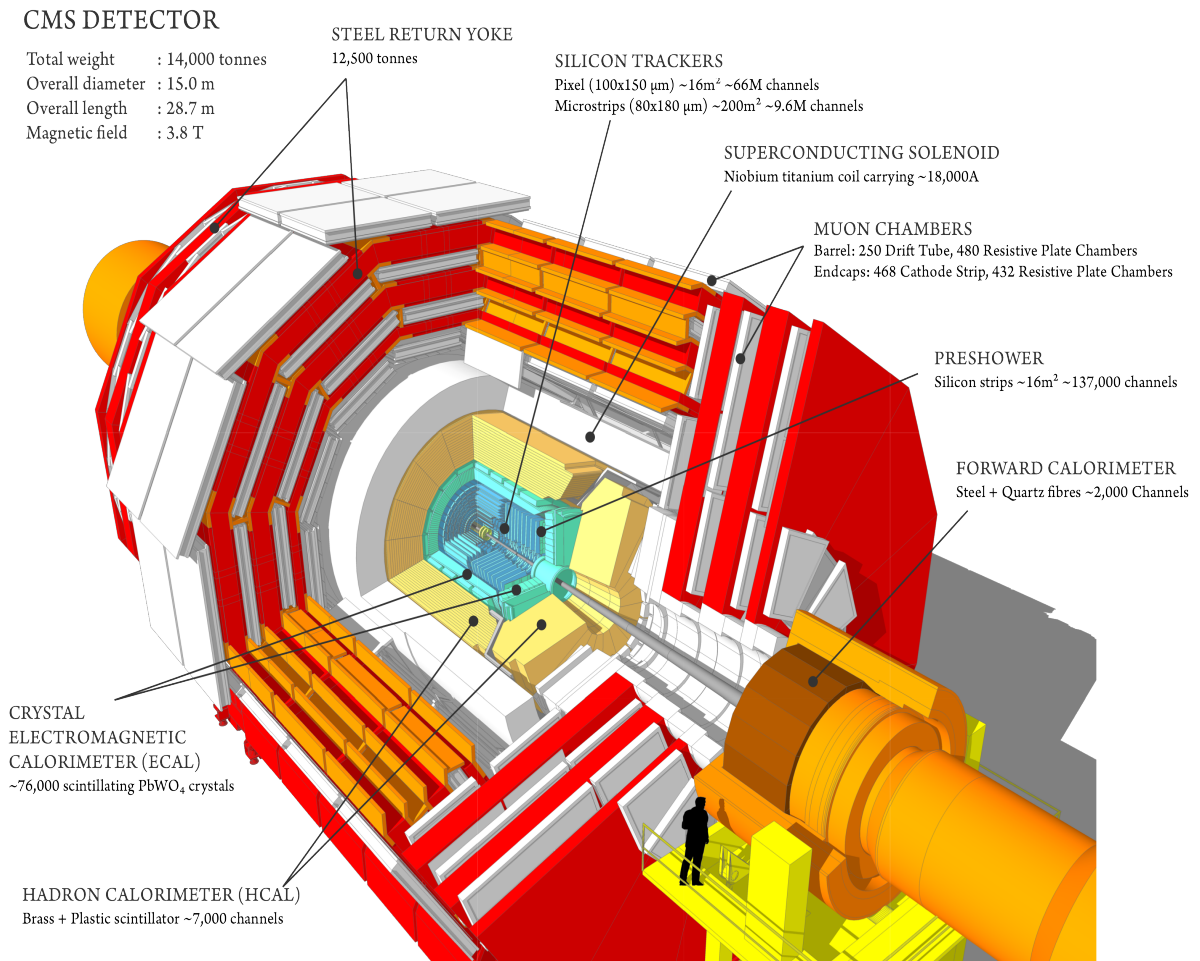


Figure 2.4: Sectional view of the CMS detector [85].

### 2.2.1 Coordinate System

The CMS follows a right-handed coordinate system, with origin defined to be the nominal collision point at the center of the detector. The  $x$ -axis points radially towards the center of the LHC ring, the  $y$ -axis vertically upwards while the  $z$ -axis points west, along the beam direction towards the Jura Mountains from LHC point 5. The polar angle  $\theta$  is measured from the  $z$ -axis, while the azimuthal angle  $\phi$  is measured from the  $x$ -axis in the  $x - y$  plane. The radial coordinate,  $r$ , is defined in the  $x - y$  plane. Instead of  $\theta$ , it is often more handy to use rapidity  $y$ , defined as:

$$y = \frac{1}{2} \ln \left( \frac{E + p_z}{E - p_z} \right), \quad (2.5)$$

where  $E$  and  $p_z$  are the measured energy and  $z$ - component of the momentum carried by the particle. The key reason why rapidity is a crucial quantity is because the rapidity differences are invariant with respect to Lorentz boost along the beam axis. But another quantity, known as pseudorapidity and defined as:

$$\eta = -\ln \left[ \tan \left( \frac{\theta}{2} \right) \right], \quad (2.6)$$

is preferred at the hadron colliders. For highly relativistic particles the two quantities are almost identical,  $y \simeq \eta$ . The rapidity in terms of pseudorapidity is given by

$$y = \ln \left( \frac{\sqrt{m^2 + p_T^2 \cosh^2 \eta} + p_T \sinh \eta}{\sqrt{m^2 + p_T^2}} \right). \quad (2.7)$$

The angular separation of two events,  $(y_2 - y_1, \phi_2 - \phi_1)$  is invariant with respect to boosts along the beam axis and the angular distance between two objects, as observed from the origin of the CMS detector, is expressed as:

$$R = \sqrt{(\Delta\eta)^2 + (\Delta\phi)^2}. \quad (2.8)$$

In collider experiments, the incoming particles collide head-on and have no transverse momentum before scattering and therefore by momemtum conservation, the final state particles must have zero total transverse momentum. Hence, the momentum and energy of the object are measured transverse to the beam direction, denoted by  $p_T$  and  $E_T$ , respectively, where  $p_T = \sqrt{p_x^2 + p_y^2}$  and  $E_T = E \sin\theta$ . The missing transverse momentum is defined as the negative vector sum of all particles detected by the detector,  $\vec{E}_T^{\text{miss}} \equiv -\sum \vec{p}_T$ . Momentum conservation dictates that  $\vec{E}_T^{\text{miss}}$  is equal, in the limit of a perfect detector efficiency and resolution, to the vector sum of transverse momentum of all undetected particles such as neutrinos or some new particle and the energy lost in nuclear processes.

### 2.2.2 Magnet

The choice of the magnet is crucial for ensuring good performance for a high energy physics experiment. Precise measurement of the charged particle momenta at a wide range of energies requires high bending power that can be achieved using strong magnetic field. For a charged particle in a uniform magnetic field,  $B$ , the momentum of the particle is given by,  $p = \gamma mv = qBr$ , where  $q$  is its charge,  $m$  is its mass and  $r$  is the bending radius of the particle. The trajectory of a charged particle in the magnetic field is an arc of radius  $r$  and path length  $L$ . The sagitta of the trajectory, defined as the perpendicular distance from the midpoint of the arc's chord to the arc itself and is given by  $s = \frac{L^2}{8r} = \frac{qBL^2}{8p}$ . Assuming that the particle crosses the full solenoid,  $L$  is equal to the radius of the solenoid. The  $p_T$  resolution depends on the magnetic field and solenoid radius as,  $\frac{dp}{p} \propto \frac{p}{BL^2}$ .

Therefore, for improvement in the resolution both a large size and a strong magnetic field is needed. The CMS design [92] having a solenoid of 6 m in diameter (and also a large tracker that defines the measurable path length) and a strong magnetic field of 3.8 T meets the requirement.

The CMS magnet [92] consists of two main parts, the coil and the yoke. The coil forms the superconducting solenoid which utilizes a 4-layer winding made from a stabilized reinforced NbTi conductor to give a magnetic field of 3.8 T. The yoke comprised of 11

large elements, 5 barrel wheels and 6 endcap disks, that returns magnetic flux yielding a field of about 2 T. The yoke was designed to achieve a balance between the outer diameter of the yoke and the size of the muon system<sup>4</sup> [83]. At full current, the energy stored in the magnetic field is  $\sim 2.7$  GJ.

### 2.2.3 Tracking System

The tracker is the innermost sub-system of the CMS detector. It is designed to measure precisely and efficiently the trajectories of charged particles from the interaction point, and reconstruct both primary and secondary vertices. It not only reconstructs the paths of muons, electrons, and charged hadrons, but also the tracks coming from the decay of very short-lived particles such as  $b$ - and  $c$ -quarks, with high momentum resolution and efficiency.

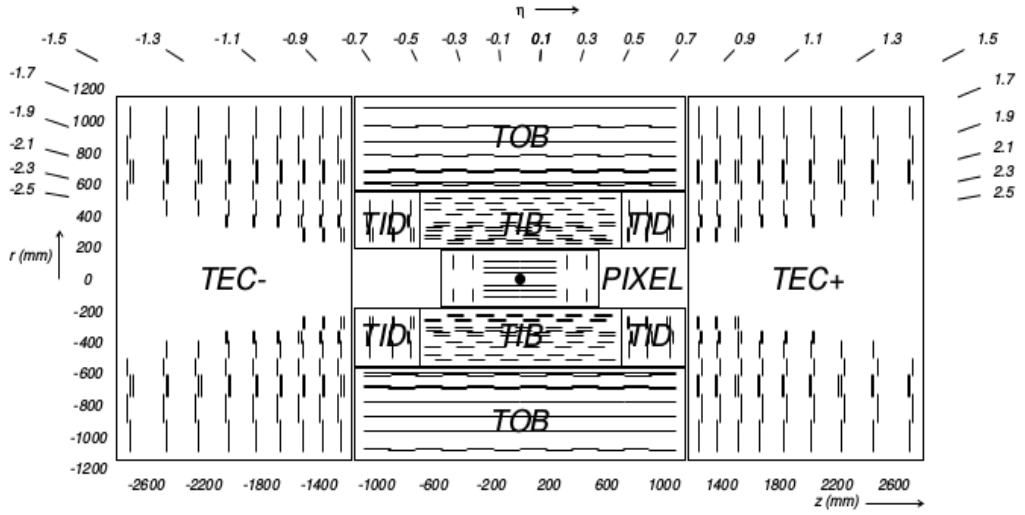


Figure 2.5: Schematic view of the CMS tracker in the  $r - z$  plane [83]. Each line depicts a detector module and double lines represents back-to-back modules. Abbreviations TEC, TIB, TID, TOB, etc. are described later in text.

A tracker system [83, 93] covering the region  $|\eta| < 2.5$  and employing more than  $200 \text{ m}^2$  of active Si sensors is shown in Fig 2.5. It surrounds the interaction point and has a length of 5.8 m and a diameter of 2.5 m. The CMS solenoid provides a homogeneous magnetic field of 3.8 T over the full volume of the tracker. At high luminosity, 20 overlapping pp

<sup>4</sup>Muon system is described in more detail in Section 2.2.5

collisions at the LHC would, on an average, result in 1000 particles traversing the tracker for every bunch crossing, i.e. every 25 ns. Therefore, a detector featuring high granularity and fast response is needed to cope with the large levels of occupancy and radiation. In addition, the intense particle flux will also cause severe radiation damage to the tracking system. These requirements on granularity, speed and radiation hardness necessitate a tracker design based entirely on silicon detector technology.

The tracks in the CMS are seeded by the hits in the tracker detector. The compatible hits are added to update the trajectory until either the detector boundary is reached, or no additional compatible hits<sup>5</sup> can be found. The collection of hits is then used to obtain the best estimate of the track parameters. However, the large amount of material within the tracker volume affects the overall event topology and reconstruction due to electron bremsstrahlung, conversions of photons to electron pairs and nuclear interactions. Therefore, it is important to estimate the amount of material of the CMS tracker. This is shown in Fig 2.6 — both in units of radiation length ( $X_0$ ) and nuclear interaction length

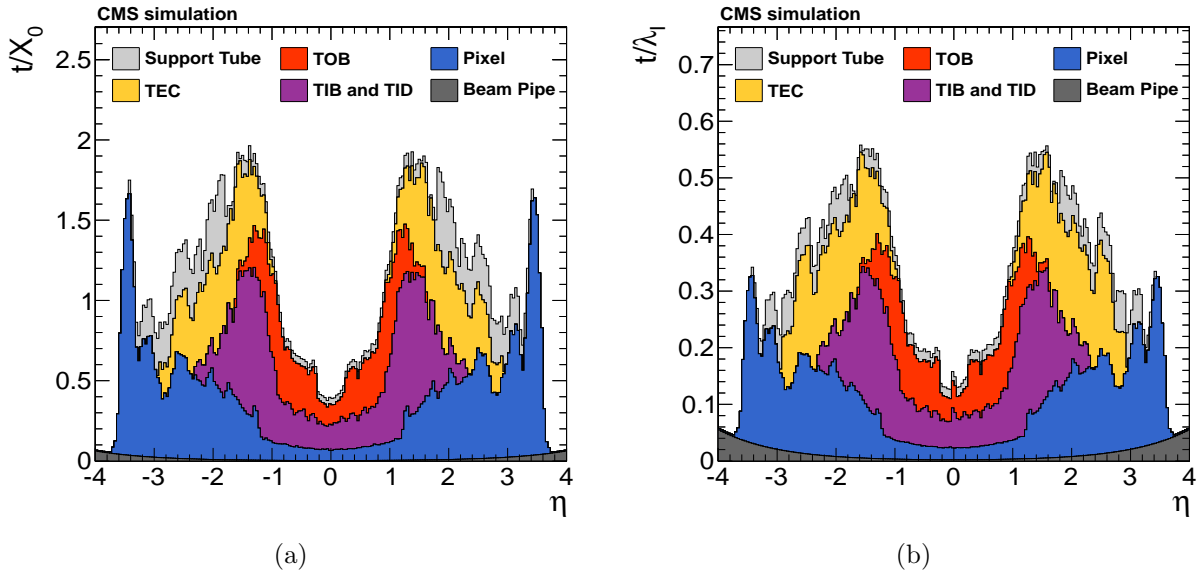


Figure 2.6: Total thickness of the tracker material traversed by a particle produced at the nominal interaction point, as a function of pseudorapidity, expressed in units of (a) radiation length  $X_0$  and (b) nuclear interaction length  $\lambda_I$  [94].

<sup>5</sup>Hits compatible with the extrapolation of parameters for a track, growing trajectory of a track, and their covariance matrix in the detector material.

$(\lambda_I)$  as a function of pseudorapidity, as estimated from simulation within about  $\sim 10\%$  accuracy [93–95]. The  $X_0$  corresponds to the mean distance over which an electron loses a fraction  $1/e$  of its energy. It also corresponds to  $7/9$  of the mean free path for pair production of a photon. At  $\eta = 0$ , the tracker material budget corresponds to about  $0.4X_0$ , while at the boundary between the barrel and the endcaps, the material budget reaches a value of  $1.8X_0$  due to cabling and other services like mechanical support in this region. The CMS tracker is composed of a pixel detector and a silicon strip tracker which are described in details in the sections to follow.

### 2.2.3.1 Pixel Detector

The pixel detector [83, 93] is the part of the tracking system closest to the interaction region with a pseudorapidity coverage of  $|\eta| < 2.5$ , as shown in Fig 2.7. Being very close to the interaction vertex and beam direction, it is inundated with a very large particle flux. It contains about 66 million Si pixels, allowing it to provide precise and highly accurate tracking points in three dimensional space,  $(r, \phi$  and  $z)$  for all emerging particles. This is essential for reconstruction of secondary vertex from decays of  $b$  – quark and tau leptons and forming seed tracks for the reconstruction of outer tracks. The pixel cells, of size  $100 \times 150 \mu\text{m}^2$ , are used to attain an occupancy level of  $\sim 10^{-1}/(\text{pixel} \times \text{bunch-crossing})$ . The pixel has a zero-suppressed analog pulse height read-out scheme that improves position resolution and helps in separating signal from noise hits as well as identifying large hit clusters from overlapping tracks.

The layout of the pixel system consists of three barrel layers (BPIX) with two endcap disks (FPIX). The 53 cm long BPIX layers are located at mean radii of 4.4, 7.3 and 10.2 cm, whereas the FPIX extends from 6 to 15 cm in radius and are placed at 34.5 and 46.5 cm on both sides of the nominal interaction point. The BPIX (FPIX) layers contain 48 million (18 million) pixels covering a total area of  $0.78$  ( $0.28$ )  $\text{m}^2$ . The forward detectors are tilted at  $20^\circ$  in a turbine-like geometry to induce charge sharing [96]. The pixel detector has a spatial resolution in the range of  $15 - 20 \mu\text{m}$  [93]. Unfortunately, they would need to be

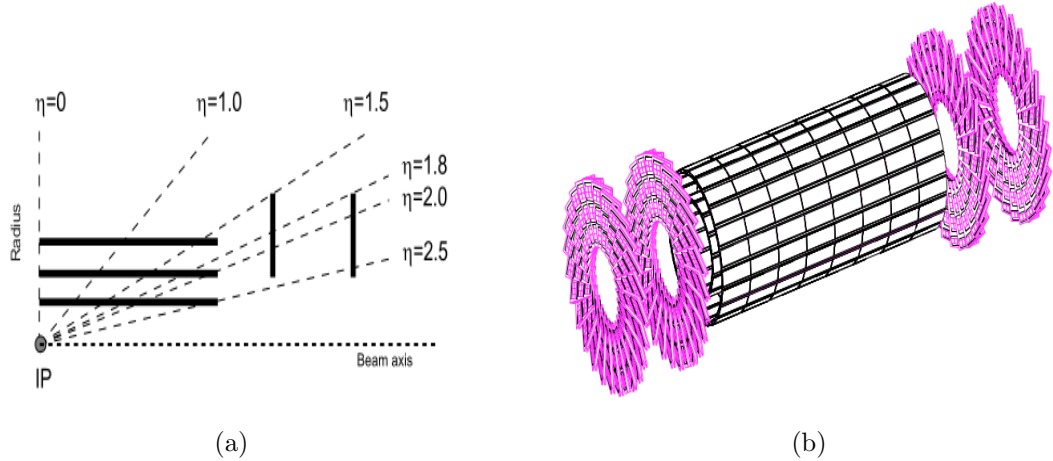


Figure 2.7: (a) Hit coverage and (b) geometrical layout of the CMS pixel detector [83].

replaced during the time period of the experiment, due to radiation damage.

### 2.2.3.2 Silicon Strip Detectors

The silicon strip tracker [83,93] is composed of 15148 detector modules distributed among the four different subsystems – Tracker Inner Barrels (TIB), Tracker Inner Disks (TID), Tracker Outer Barrels (TOB) and Tracker EndCaps (TEC). Each module carries either one thin ( $320\mu\text{m}$ ) or two thick ( $500\mu\text{m}$ ) silicon sensors. The dimension of the strips increases with increasing distance from the interaction point so that the occupancy level is kept to  $\sim 1\%$ . The occupancy is defined as the number of strip measurements in an event divided by the number of all active strips. The silicon detectors work in much the same way as the pixels – a charged particle crosses the material, knocks out electrons from the atom and within the applied electric field, gives a very small pulse of current lasting a few nanoseconds. The schematic longitudinal view of the silicon strips in terms of different layers and their arrangements in  $\eta$  and  $z$  plane is shown in Fig 2.8 .

The TIB and TID are composed of four barrel layers and three disks at each end. The silicon strip tracker provides up to four  $r - \phi$  measurements with a position resolution of  $23\mu\text{m}$  in the two inner layers and  $35\mu\text{m}$  in the two outer layers [83]. The TIB and TID are surrounded by the six layers of TOB, providing a resolution of  $53\mu\text{m}$  in the first

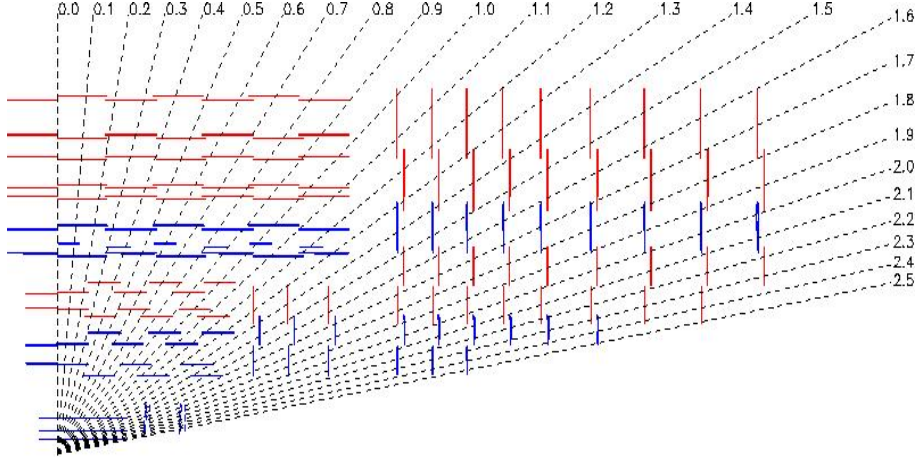


Figure 2.8: A Schematic layout of the silicon microstrip detector [83].

four layers and  $35\mu\text{m}$  for the outer two layers [83]. Beyond  $z = 118\text{cm}$  TEC provides additional forward coverage up to  $|\eta| < 2.5$ , giving nine  $\phi$  measurements per trajectory and extending up to  $282\text{cm}$  [83].

#### 2.2.4 Calorimeter System

A calorimeter is a detector which measures the energy of a particle. The CMS calorimeters are designed to measure the energy of electrons, photons and hadrons (jets) produced in collisions. The CMS calorimeter is divided into electromagnetic and hadronic sections. The electromagnetic calorimeter (ECAL) is used to measure the energy of particles which interact electromagnetically such as photons and electrons whereas the hadronic calorimeter (HCAL) is designed to measure the energy of strongly interacting particles. Hadrons interact via strong force leading to showers that has both electromagnetic and hadronic component. The hadronic component of the shower scales with the nuclear interaction length and can not be contained within the ECAL. Muons, though interact via electromagnetic force, behave in a very different way. They loose energy primarily through ionization, with energy losses of the order of  $1 - 2\text{ MeV/g/cm}^2$  and, therefore, different sub-system is needed for the detection of muons. Interacting with matter via the weak force, neutrinos typically pass through the matter unimpeded and undetected, and can be observed only indirectly as an imbalance in event energy in the transverse plane. The

measurement of this imbalance, termed as missing transverse energy, plays a critical role for new physics searches, such as compositeness, supersymmetry, extra dimensions etc.

#### 2.2.4.1 Electromagnetic Calorimeter

The ECAL [83, 97] is a homogeneous, hermetic calorimeter made up of 61200 lead tungstate ( $\text{PbWO}_4$ ) scintillating crystals mounted in the central barrel part, accompanied by 7324 crystals in each of the two endcaps. It covers the pseudorapidity region up to  $|\eta| < 3$ , and is complemented, in the forward region ( $1.653 < |\eta| < 3.0$ ) by Si-Pb preshower, as shown in Fig 2.9. In order to fulfill the scientific goals of the CMS, the ECAL was designed to have a high energy resolution for  $e/\gamma$  objects. To achieve this, the ECAL was positioned inside the CMS magnet so that the amount of energy loss due to the material upstream can be minimized. Within the LHC environment, it is important

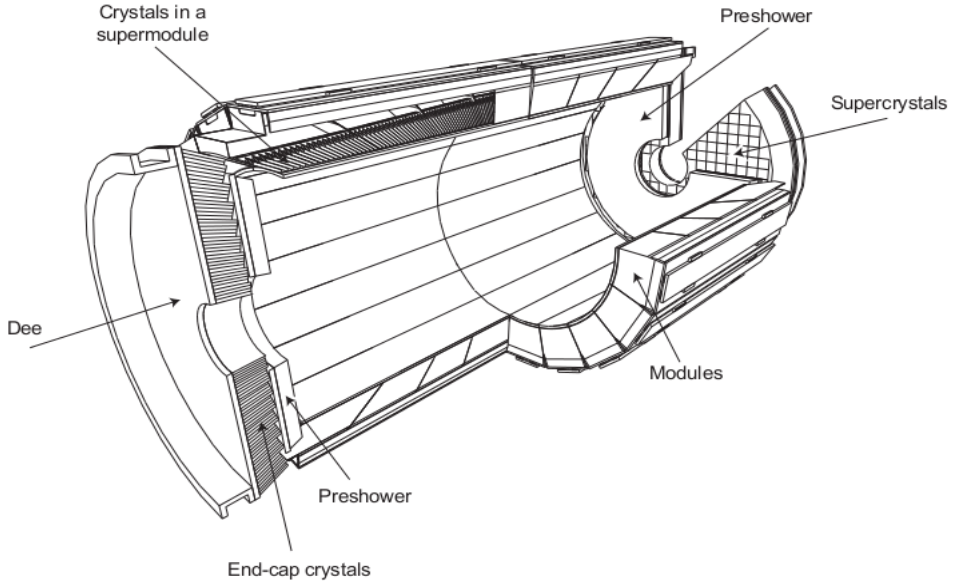


Figure 2.9: A schematic design of the CMS ECAL showing the arrangement of crystals, supermodules and endcaps with the preshower in front [83].

to design a calorimeter which is fast, has fine granularity and is radiation tolerant. The  $\text{PbWO}_4$  crystals have a large density ( $8.28 \text{ g/cm}^3$ ), a small radiation length  $X_0$  (0.89 cm), and a small Moli  re radius (2.2 cm), which makes them an appropriate choice for a compact and high granular calorimeter. The total amount of material between the interaction

point and the ECAL increases from  $0.4 X_0$  close to  $\eta = 0$  to almost  $2 X_0$  near  $|\eta| = 1.4$ , before falling again to about  $1.3 X_0$  around  $|\eta| = 2.5$ . Therefore, the resolution of the ECAL depends on the  $p_T$  and  $\eta$  of the object, and whether the electron or photon undergoes bremsstrahlung.

The ECAL barrel (EB) covers the region  $|\eta| < 1.48$ , and has an internal surface radius of 1290 mm. It is made up of 61,200 trapezoidal crystals. Each crystal has a frontal area of approximately  $22 \times 22 \text{ mm}^2$  and a length of 230 mm ( $25.8 X_0$ ), which leads to a granularity of 0.0174 in  $\eta$  and  $\phi$ . A half-barrel consists of 18 supermodules, each containing 1700 crystals and covering  $20^\circ$  in  $\phi$ . Photodetectors are placed in front of the crystals to collect the light and convert it into signals which can be read out by the electronics chain. Since the light yield from the  $\text{PbWO}_4$  crystals is relatively low, amplification of the signal needs to be done, and hence silicon avalanche photodiodes (APDs) are used. In addition to intrinsic gain, APDs are also insensitive to magnetic fields and have high radiation resistance and are, thus, suitable for EB.

The endcaps (EE) cover the region  $1.48 < |\eta| < 3.00$ , are located at  $|z| > 3154 \text{ mm}$  and are composed of 4 half disks. Each half-disk is made up of 3,662 trapezoidal crystals each having a frontal area of  $28.6 \times 28.6 \text{ mm}^2$  and a length of 220 mm ( $24.7 X_0$ ). The crystals in each disk are organized into 138 standard  $5 \times 5$  supercrystal units with 52 mm wide voids in between the groups. The crystals are arranged in a quasi-projective geometry pointing  $\pm 1300 \text{ mm}$  beyond the nominal interaction point. Photodetectors used in the EE are Vacuum phototriodes (VPTs). The VPTs can be operated in a very high radiation environment and hence are used in the EE.

A preshower detector is a pair of sampling calorimeters designed to distinguish neutral pions from real photons and improves the position measurement of electrons and photons with high granularity. Each calorimeter consists of two planes of silicon sensors interleaved with a total of  $3 X_0$  of lead and is located in front of the EE and covers the region  $1.65 < |\eta| < 2.60$ .

The ECAL energy resolution for electromagnetic showers below 500 GeV, can be

parametrized as :

$$\left(\frac{\sigma}{E}\right)^2 = \left(\frac{S}{\sqrt{E}}\right)^2 + \left(\frac{N}{E}\right)^2 + C \quad (2.9)$$

where  $S$  is the intrinsic stochastic term,  $N$  is the noise term and  $C$  is the constant term with details as follows :

- Stochastic term ( $S$ ) : This includes contribution from event-to-event fluctuation in the lateral shower containment, photostatistics contribution, fluctuations in the energy deposited in the preshower absorber (where present) with respect to what is measured in the preshower silicon detector. The contribution of these fluctuations to the energy resolution of the calorimeters follow Poissonian distribution, hence the resolution scales as  $1/\sqrt{E}$ .
- Noise term ( $N$ ) : The three contributions to the noise term include : electronics noise; digitization noise; and pileup noise. The signal amplitude in the test beam is reconstructed using a simple digital filter. The noise measured, after this amplitude reconstruction, for channels in barrel supermodules is  $\sim 40$  MeV/channel in the highest gain range. This noise includes both electronics and digitization noise and varies as  $1/E$ . The noise from the pileup is found to be very small.
- Constant term ( $C$ ): The most important contributions to the constant term include: non-uniformity of the longitudinal light collection, inter calibration errors, and leakage of energy from the back of the crystal.

The test beam results [83, 98] using the energy measurement in  $3 \times 3$  crystal lattice, lead to the following values for the various terms :  $S = 2.8\%$ ,  $N = 124$  MeV, and  $C = 0.3\%$  in the barrel regions and  $S = 5\%$ ,  $N = 500$  MeV and  $C = 0.3\%$  for the endcap regions.

#### 2.2.4.2 Hadronic Calorimeter

The hadronic calorimeter [83, 99] is a sampling calorimeter surrounding the ECAL, which is used in conjunction with the ECAL to measure the energy and direction of hadronic

particles and to estimate the missing transverse momentum ( $E_T^{\text{miss}}$ ). The HCAL is composed of four sub-detectors – HCAL Barrel (HB) [100], HCAL Endcaps (HE) [101], HCAL Outer (HO) [102], and HCAL Forward (HF) [103] as shown in Fig 2.10. The HCAL consists of plastic scintillator tiles read out with embedded wavelength-shifting (WLS) fibres interleaved with overlapping brass plates for the absorber material.

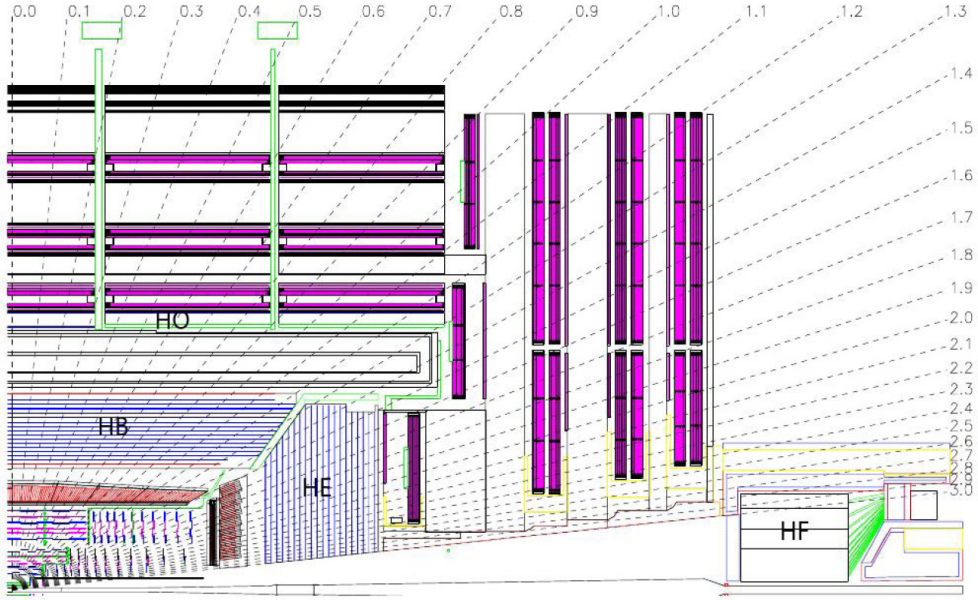


Figure 2.10: A schematic design of the CMS HCAL showing the barrel section (HB), endcap section (HE), the tail catcher outside the solenoid (HO) and the forward section (HF) [87].

The HB detector consists of 36 identical azimuthal wedges covering the region  $|\eta| < 1.3$ . Each wedge is segmented into 16 azimuthal plates, bolted together in such a way that there is no projective dead material. The absorber is made of brass (70% Cu and 30% Zn), except for the first and last layers which are made of stainless steel for structural strength. It is restricted between the outer extent of the ECAL ( $R = 1.77$  m) and the inner extent of the magnet ( $R = 2.95$  m), which constrains the total amount of material that can be put in to absorb the hadronic shower. Therefore, to ensure adequate sampling of the hadronic showers, the calorimeter was extended outside of the solenoid with a tail catcher called HO, which uses the solenoid as an additional absorber layer. The total thickness of the calorimeter system is thus extended to a minimum of  $11.8\lambda_I$ . The HE covers the region  $1.3 < |\eta| < 3.0$ . The active medium uses the tile and wavelength shifting

fibre concept to bring out the light, which is then read out by means of hybrid photo diodes (HPDs). Up to  $|\eta| < 1.6$ , the HCAL towers have a size of  $\Delta\eta \times \Delta\phi = 0.087 \times 0.087$ , while for  $|\eta| > 1.6$ , the size increases to  $\Delta\eta \times \Delta\phi \sim 0.175 \times 0.175$ .

To cope with the exceptionally high radiation dose (up to about 10 mSv/h), the HF calorimeters (located only 11 m away from the interaction point) covering the region  $3.0 < |\eta| < 5.0$  uses more robust, minimal-maintenance quartz fibres as the active material and steel as the absorber material. The HF is designed to improve the measurement of  $E_T^{\text{miss}}$  and to enable identification and reconstruction of very forward jets which constitute distinguishing characteristics of several important physics processes. A signal is generated in the HF when a charged particle traverses a quartz fiber with a velocity greater than speed of light in the fiber, resulting in Cherenkov radiation.

For the CMS HCAL, the resolution is parametrized as [87, 104] :

$$\left(\frac{\sigma}{E}\right)^2 = \left(\frac{A}{\sqrt{E}}\right)^2 + (B)^2, \quad (2.10)$$

with the parameters, for both HB [100] and HE [101], being  $A = 0.847 \text{ GeV}$  and  $B = 0.074$ . Corresponding values for the HF [103] are  $A = 1.98 \text{ GeV}$  and  $B = 0.09$ .

The CMS calorimeter system is non-compensating, i.e. its response to electrons is not same as to that to hadrons of the same energy. Experimentally, the  $e/h$  ratio is not directly accessible. Instead, the ratio of the responses to pion and electron ( $\pi/e$ ) was measured in test beams [105] and is related to the  $e/h$  ratio by the formula :

$$\frac{e}{h} = \frac{1 - f_{em}}{\pi/e - f_{em}}, \quad (2.11)$$

where  $f_{em}$  is the electromagnetic fraction of the shower energy. For test beam particles with energies above  $\sim 8 \text{ GeV}$ , the  $h/e$  ratio was found to be  $1.4 \pm 0.1$ . An event-by-event correction scheme was developed [105, 106]. A linear response (within 1.3%) to hadrons of momenta between 5 and 350 GeV was achieved.

## 2.2.5 Muon System

The muon system [107] forms the last component of the CMS detector following the super conducting solenoid. The CMS has been designed to provide good muon identification, momentum resolution and efficient trigger on muons within  $|\eta| < 2.4$  and  $p_T \leq 1 \text{ TeV}$ .

The muon system uses three different technologies to detect muons: drift tubes (DT) in the barrel region ( $|\eta| < 1.2$ ), cathode strip chambers (CSC) in the endcap region ( $|\eta| > 1.2$ ) and resistive plate chambers (RPC) in both, the barrel and the endcaps. The RPCs provide a lower spatial resolution but a faster response than the DTs or CSCs. The DTs/CSCs and the RPCs provide two independent and complementary sources of information for the first level trigger<sup>6</sup> to ensure a robust, flexible and precise trigger decision. A diagram showing the mechanical layout of the three muon detection systems can be found in Fig 2.11.

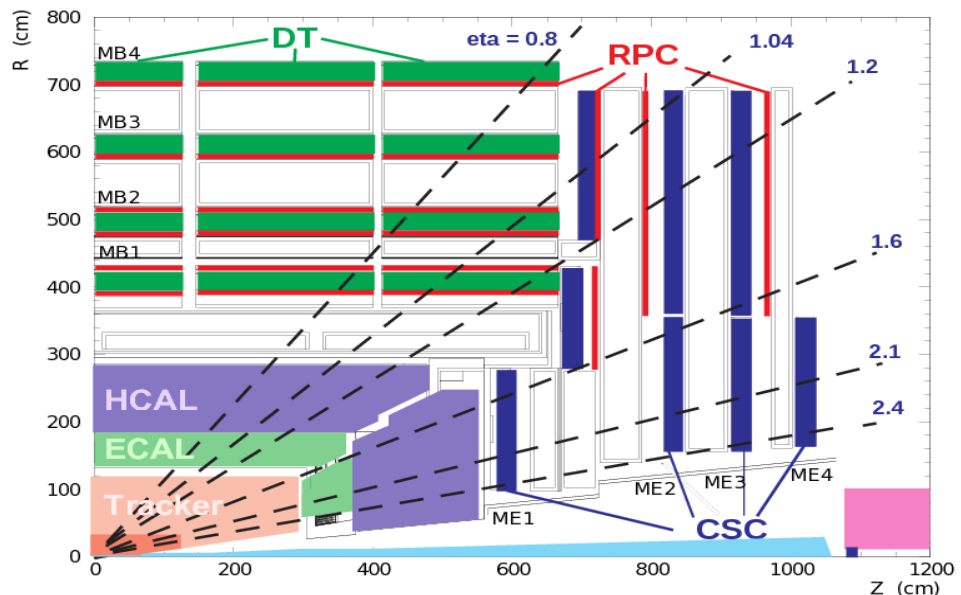


Figure 2.11: A schematic design of one quadrant of the muon system in the  $r - z$  plane showing the position of three sub-detectors used for muon detection [85].

<sup>6</sup>More detail about trigger system is given in Section 2.3

### 2.2.5.1 Drift Tube Chambers

In the barrel region, where the muon flux is low and the magnetic field uniform, four layers of muon stations are used, occupied by drift tube (DT) chambers covering up to  $|\eta| < 1.2$ . The three innermost stations are comprised of 12 chambers each, which measure muon coordinates in the  $r - \phi$  plane and provide a measurement in the  $z$ -direction, while the outermost station measures only the  $\phi$ -view. The DT chambers consist of individual drift tube cells that contain a  $50\text{ }\mu\text{m}$  diameter anode wire and two electrode plates that create the drift electric field. The walls of the cell are grounded, acting as cathodes. The cells are filled with a gas mixture (85% Ar and 15%  $\text{CO}_2$ ) and the wire and electrodes are operated with a voltage difference of about 1.8 kV. The transverse dimension of the cells was chosen to be 21 mm to optimize drift time, gain and number of channels. With these design parameters, the DT achieve a gain of  $10^5$ , resulting in a drift time of 380 ns and a linear relationship between drift time and drift path which is essential for the chamber to provide triggering capabilities. Figure 2.12 shows the basic design of a DT cell.

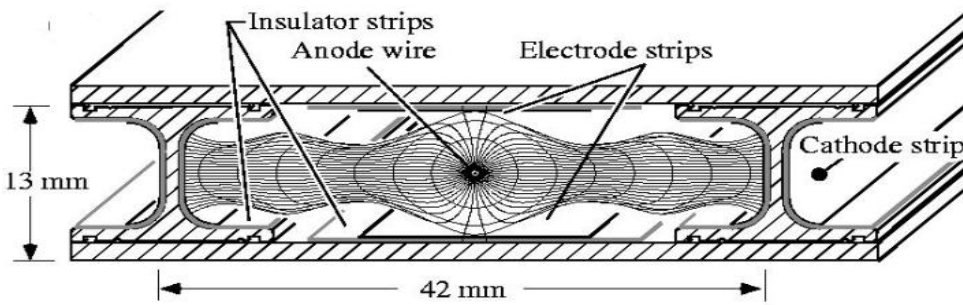


Figure 2.12: Individual drift tube cells and pictorial representation of its operation principle [87].

### 2.2.5.2 Cathode Strip Chambers

In the endcap regions, where the magnetic field is large and non-uniform, cathode strip chambers (CSC) are installed providing a coverage in the region  $0.9 < |\eta| < 2.4$ . The CSCs are multi-wire proportional chambers consisting of six planes of anode wires interleaved among seven cathode panels. The gold-plated tungsten wires run azimuthally, defining the track's radial component, while the strips are milled on cathode panels and run lengthwise at a constant  $\Delta\phi$  width. The angular ( $\phi$ ) position of the track is estimated by extrapolating the charge that is induced on the strips as shown in Fig 2.13. The nominal gas mixture is 40% Ar, 50% CO<sub>2</sub> and 10% CF<sub>4</sub>. Addition of CF<sub>4</sub> helps to avoid polymerization on wires. The wires give very fast signals that provide very good time resolution while the development of the avalanche on the strips gives very good position resolution. The CSCs can operate at high rates and in large and non-uniform magnetic fields without requiring precise monitoring of gas, pressure or temperature and can provide trigger and precision position measurement in the same device. The CSC system comprises of 468 trapezoidal chambers covering 10° or 20° in the  $\phi$ -direction.

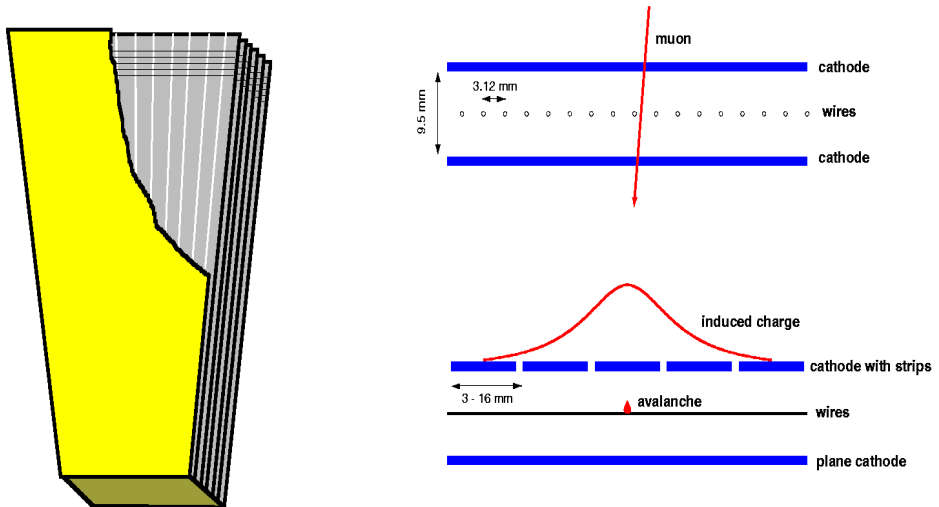


Figure 2.13: Operation principle of the Cathode Strip Chamber [85].

### 2.2.5.3 Resistive Plate Chambers

In order to improve the performance of the muon trigger, an additional system of resistive plate chambers (RPCs) is installed, spanning both the barrel and the endcap regions. The RPC system has 480 barrel and 432 endcap chambers. Two rectangular section RPCs per DT chamber are installed in the barrel region and two trapezoidal ones per CSC chambers are installed in the endcap regions. They are parallel plate gaseous detectors that combine adequate position resolution with a very high operational speed. The RPC is able to tag the presence of an ionizing particle in a time-frame much shorter than the typical bunch crossing time, which makes it an ideal trigger device since, together, they can associate the correct bunch crossing (25 ns between two bunch crossings) with the muon. The CMS RPC chamber consists of two gaps operated in an avalanche mode with read-out strips in-between. The total induced signal is the sum of the induced signal in both gaps. The RPCs need intensive monitoring of temperature, humidity and pressure to ensure stability of conditions for proper operation.

The CMS muon system consists of about  $25000\text{ m}^2$  of detection planes and about a million readout channels. For a stand alone muon system, for  $p_T$  up to 200 GeV at low  $\eta$ , the offline muon momentum resolution [83] is  $\sim 9\%$  (due to multiple scattering in the detector material before the first muon station). It however, varies between 15 – 40% at  $p_T \sim 1\text{ TeV}$  depending on  $\eta$ . Adding information from the inner tracker, i.e., considering a global muon, improves the momentum resolution by an order of magnitude at low  $p_T$ . At high  $p_T$  (1 TeV) the global muon has a momentum resolution of about 5%.

## 2.3 Trigger and Data Acquisition Systems

At the nominal design LHC luminosity of  $10^{34}\text{ cm}^{-2}\text{s}^{-1}$ , a bunch crossing rate of 40 MHz (or 25 ns) will result in  $\sim 10^9$  interactions per second, leading to  $\sim 100\text{ TB}$  of data to be stored. It is, thus, almost impossible to store information about each interaction for offline processing. Hence, for reducing the data in real time and still keeping potentially

interesting events, an automated system, commonly referred to as the trigger system [108] is designed along with a Data AcQuisition (DAQ) system [109] to operate at the unprecedented LHC rate. The frequency of events to be recorded for offline processing is of the order of a few 100 Hz achieved by the two-layer trigger system. The first is a Level-1 trigger (L1), implemented in the hardware, based on custom electronics and is designed to reduce the incoming average data rate to a maximum of 100 kHz. The second level, called High Level Trigger (HLT), is a software based decision taking system, relying on thousands of commercial processors in an event filter farm. The data event passing both levels of triggering system is recorded for offline physics analysis. A brief description of the L1 and HLT systems is given in sections to follow. To reduce the output rate further,

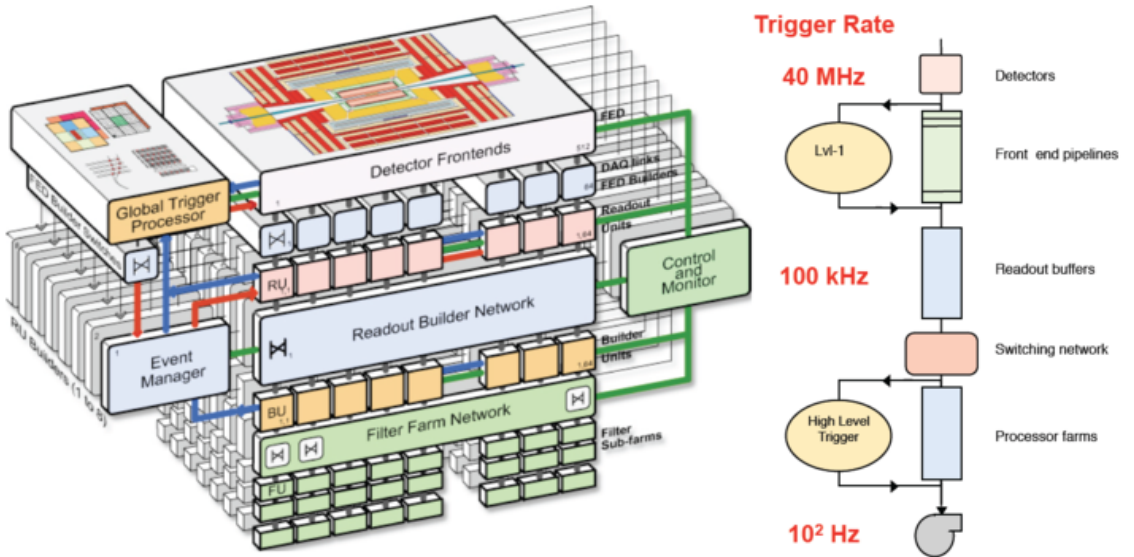


Figure 2.14: Schematic diagram of architecture of CMS DAQ and trigger system [85].

at both the L1 and HLT levels, algorithms can be *prescaled* to accept only a fraction of the events which pass the selection criteria defined by a specific algorithm. The HLT is a part of the DAQ system that manages the overall flow of the data. The DAQ system also includes detector front-end electronics, readout modules, an event builder network, as well as management and monitoring systems. The diagram of the complete DAQ system along with the trigger system is shown schematically in Fig 2.14.

### 2.3.1 Level-1 Trigger

The L1 trigger [108] is implemented in the form of custom hardware processors which use only low resolution, coarsely segmented data from calorimeters and muon systems while holding the high resolution data in pipelined memories in the front end electronics. The L1 pipeline data storage time is  $3.2\mu\text{s}$ , the time in which the L1 trigger decision is transmitted to the detector electronics. The purpose of the L1 trigger is to perform sufficient reduction from the input crossing rate of  $\sim 40\text{ MHz}$  to provide an output rate of few  $100\text{ kHz}$ . The hardware components of the L1 trigger consist of field-programmable gate-array (FPGA) technology, as well as ASICs and programmable lookup tables (LUTs).

A block diagram depicting the schematic overview of the L1 trigger system is shown in Fig 2.15. At each bunch crossing, the calorimeters produce separate ECAL and HCAL trigger primitives based on energy deposited in the respective calorimeters, which are then processed in the Regional Calorimeter Trigger (RCT) before being sent to the Global Calorimeter Trigger (GCT). The GCT sorts electron, photon, and jet candidates (including jets coming from hadronic decays of  $\tau$  leptons) and calculates global quantities like  $E_{\text{T}}^{\text{miss}}$  and  $H_{\text{T}}$  which are fed into the CMS Global Trigger (GT). In muon subsystems, the

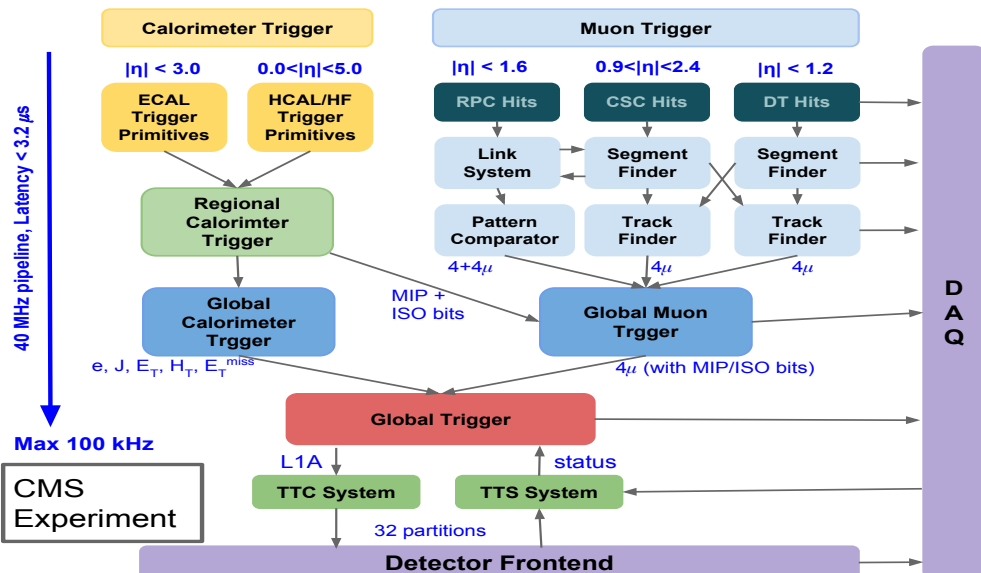


Figure 2.15: Architecture of CMS Level-1 trigger system [108].

DTs and CSCs create the track segments using the hit patterns in the chambers and send them to a track-finder to select the top 4-muon candidates per subsystem. The RPCs, using a different approach, compare patterns of 4-barrel and -endcap muons. Exchanging track segments information among muon subsystems helps close geometric gaps in the muon coverage and raise overall muon trigger efficiency. Finally, 16 muon candidates are passed to the Global Muon Trigger (GMT) system for sorting and removal of duplicates. The GMT then sends the top 4-global muon candidates taking information from the RCT on calorimeter deposits around the muon candidates enabling the use of isolated muon triggers to GT.

The GT receives all the trigger objects from GCT and RCT systems. It then applies programmable topological cuts and different energy thresholds on these objects and issues the final Level-1 Accept (L1A) decision. The L1A is then sent to the Trigger Timing and Control (TTC) system for distribution to the detector front-end electronics. The TTC interfaces with the LHC to provide orbit and clock information. The GT sends out command via the TTC to keep the detectors and their electronics and all the links in sync, stop a run, start a run, etc.

### 2.3.2 High Level Trigger

The High Level Trigger (HLT) [109] receives and processes the events accepted by the L1 trigger by using a software based system composed of an event filter farm of commercial CPUs with filters and builder units. The goal of the HLT is to reduce the incoming rate of 100 kHz by a factor of  $\mathcal{O}(10^3)$ , leading to an output rate of the order of few 100 Hz. The HLT makes use of full resolution and granularity of the detector to run complex algorithms for offline reconstruction of the events. The average processing time is roughly 40 ms, with some events requiring up to a second. At this stage, the information from the tracker is also used for isolation and trigger selection. The full event information is analyzed via a predetermined set of algorithms with programmable structures and thresholds known as *trigger paths*, constituting a *trigger menu*. A *trigger path* is nothing but a set of

algorithms that reconstruct one or more physics candidates and applies selection criteria to these reconstructed candidates and their various isolation and kinematical quantities. The algorithms in each path are executed in increasing order of complexity to reduce the input rate before CPU-expensive reconstructions, such as the particle-flow algorithm. Events satisfying any one of the HLT trigger paths are sent to the storage manager where the event data is stored locally on disks until transferred to the CMS Tier-0 center at CERN for offline processing and permanent storage. More details about the HLT designed for this analysis are prescribed in Chapter 5.

### 2.3.3 DAQ

The CMS Data Acquisition System (DAQ) [109] collects data fragments from respective detector front-ends to form a full event in two stages before transporting them between the L1, HLT, and the storage center. The architecture of the CMS DAQ is schematically shown in Fig 2.14. It sustains an input rate of 100 kHz, for a data flow of about 100 GB/s. It provides necessary computing power for the HLT to perform its operations. The DAQ system utilizes up to eight slices that work autonomously and can handle an event rate up to 12.5 kHz. The Trigger-Throttling-System (TTS) is designed to protect the system against the back-pressures, which may occur when the buffer overflows in the sub-detectors Front-End Drivers (FEDs) due to variation in event size or rate, leading to loss of synchronization. The TTS gives a quick feedback from any sub-detector FEDs to the GT processor to control trigger rates before the buffer overflows. Furthermore, *prescales* could be adjusted to optimize the available DAQ capacity and performance during operation.

## 2.4 Software and Computing

The CMS users have access to a collection of softwares of the CMS experiment based on object oriented structures in C++ and python, referred to, in the whole, as the CMS

software framework (CMSSW) [87]. The single framework supports a variety of applications covering the entire range of experimental work including simulation, calibration and alignment, and reconstruction modules that process event data in order to perform physics analysis. The CMSSW event processing model is composed of one executable, known as cmsRun, and various plug-in modules that are managed by the framework. All the codes needed in the processing of events (calibration, reconstruction algorithms, etc.) are contained in the modules. The same executable is used for both the detector and Monte Carlo (MC) simulated data.

The CMS offline computing system has to support the storage, transfer and manipulation of the recorded collision data. The CMS application software performs a variety of event processing, selection and analysis tasks. The main concept of the CMS data model is the “Event”. The “Event” provides access to the information stored in the recorded data. The “Events” are physically stored as ROOT files. The “Event” is used by a variety of physics modules which perform well-defined functions of reconstruction or analysis of the Event. The modules execute independently from one another.

The CMS computing system has several event formats with differing levels of detail and precision in order to achieve the required level of data reduction. The RAW format contains the full recorded information from the detector and also a record of the trigger selection. The RAW data is permanently archived in safe storage with size of 1.5 MB/event. For simulated data, the size of the RAW dataset is about 2 MB/event due to additional Monte Carlo information. The Reconstructed (RECO) data is derived from the RAW data and provides access to reconstructed physics objects for physics analysis in a convenient format. The RECO events contain high-level physics objects such as jets, photons, muons, electrons,  $b$  – jets, etc, with a size of the order of 250 kB/event. The Analysis Object Data (AOD) is the compact analysis format with a reduced size of  $\sim 50$  kB/event, which is produced by filtering of RECO data to be used by almost all the physics analyses.



# Chapter 3

## Event Simulation and Data Samples

Analysis of data collected by experiments requires the knowledge of how various particles (also referred to as physics objects at various occasions in this thesis) behave in the detector, which can be foreseen by simulating the events. Even before the experiment begins, the simulation chain provides valuable inputs for the very design of the experiment, along with its various sub-detectors, and guides the reach for most interesting physics program in pursuit of new physics. Predicting the results of pp collisions involves the modelling of several aspects, such as the structure of the proton, the scattering cross section, the decay of unstable particles, and the hadronization of quarks and gluons into jets. These algorithms are based on random numbers weighted by the probability of the underlying processes occurring in particle collisions and are referred to as “event generation”. Event generation forms the first step in the simulation chain. There are several event generators or Monte Carlo (MC) generators [110,111] as they are often called, available for a wide range of collider experiments, such as PYTHIA [112], MADGRAPH [113], and HERWIG++ [114] to name a few. The details of implementation of the underlying physics processes are different in each of these generators, but the fundamental idea of simulating events to match the real collision scenario remains the same.

After generation of events, the response of the detector to physics objects must be modelled. The generated events are passed through detector simulation to obtain the effect of

material on various particles. The information for the input event received after detector simulation are used for the reconstruction of various physics objects and are analyzed using the program used for analyzing experimental data. The simulation data along with the experimental data are important for estimating efficiencies, expected backgrounds, determining uncertainties, and adjusting the trigger parameters. The simulation and experiment are, thus, interleaved through an iterative loop and the interpretation of the experimental data depends, to some degree, on the assumptions made in the simulation tools.

This chapter describes the methods and tools used for simulating pp collision events in the CMS detector. A description of the MC generators and event simulation used to model the signal process  $pp \rightarrow q^* \rightarrow \gamma + \text{jet}$ , and potential physics backgrounds has been given.

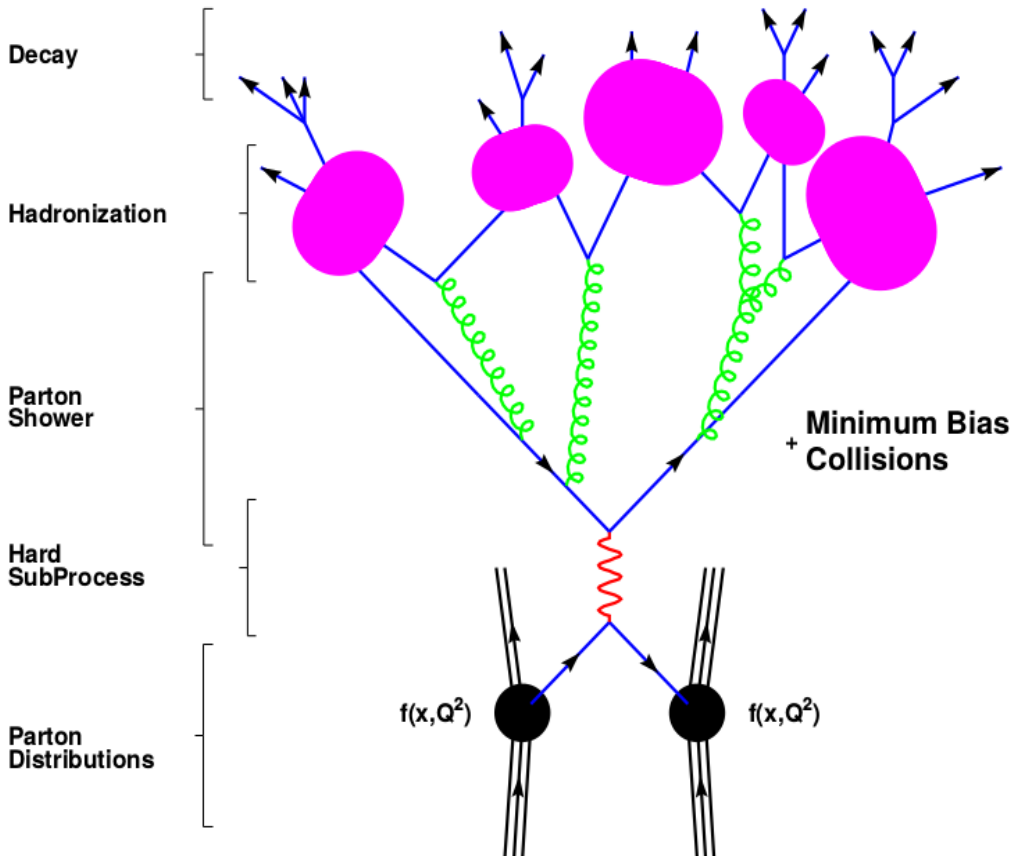


Figure 3.1: Illustration of a generated event depicting incoming partons undergoing interaction via a hard scattering process, and outgoing partons showering and hadronizing.

## 3.1 Event Generation

Event generation forms the first step in the simulation process and is usually performed in various steps following a modular approach.

### 3.1.1 Hard Scattering and QCD Radiation

The simulation starts with partons from the colliding protons interacting via hard scattering as shown in Fig 3.1 from Ref [111], producing SM particles such as quarks, leptons, photons, or some new hypothetical particle (say *preon*) [69–71] as predicted by new physics models. The cross section and the differential kinematic distribution for a  $2 \rightarrow 2$  sub-process in hadronic collisions at tree level are calculated as follows:

$$\sigma(ab \rightarrow cd) = \sum_{ab} \int_0^1 \int_0^1 f_a(x_1, \mu_F^2) f_b(x_2, \mu_F^2) \hat{\sigma}_{ab \rightarrow cd} \left( \hat{s}, \alpha_s(\mu_R^2), \frac{Q^2}{\mu_F^2}, \frac{Q^2}{\mu_R^2} \right) dx_1 dx_2 \quad (3.1)$$

where  $\hat{s}$  is given by the relation  $\hat{s} = x_1 x_2 s$ , with  $s$  being center-of-mass energy of the collider,  $Q$  is the characteristic hard scale of the interaction,  $\mu_F$  is the factorization scale, and  $\mu_R$  is the renormalization scale. Both the  $\mu_{R,F}$  scales are arbitrary parameters of a fixed order calculation. At all orders of the perturbative expansion, the cross section must be independent of them (i.e.  $\partial\sigma/\partial\mu_R = \partial\sigma/\partial\mu_F = 0$ ). For all practical calculations of cross sections at a fixed order, it is assumed that  $\mu_R = \mu_F = Q$ . The function  $f_a(x_1, \mu_F^2)$  represents the probability density for finding a parton  $f_a$  in the proton, also referred to as the Parton Distribution Function (PDF), carrying a fraction  $x_1$  of the initial proton momentum when the factorization scale is  $\mu^2$ . There is also a possibility for parton  $f_a$  to carry momentum fraction  $x_2$  and parton  $f_b$  to carry  $x_1$ . The  $\hat{\sigma}_{ab \rightarrow cd}$  represents the parton level cross section for the hard process leading to  $cd$  final state from the initial partons  $a$  and  $b$ . The fully differential parton level cross section is calculated as the product of the corresponding matrix element squared, averaged over initial state spin and color degrees of freedom, sum over the spins of the final state particles, and the parton flux. The cross section is computed using Eq 3.1 with MC integration techniques and considering

uniformly distributed random numbers for variables,  $\theta$ ,  $\phi$ ,  $x_1$ , and  $x_2$ .

Our understanding of the QCD is incomplete in the sense that a derivation from first principles of parton distributions does not yet exist, although some efforts are being made in lattice QCD studies. It is, thus, necessary to rely on parameterizations, where experimental data are used along with evolution equations [115] for the  $Q^2$  and  $x$  dependence. The PDFs are determined by global fits to data from deep inelastic scattering, Drell-Yan processes, and jet production at high energies. The PDFs used in the analysis described in this thesis is from the Coordinated Theoretical Experimental Project on QCD (CTEQ) group [116]. In particular, the parametrization, CTEQ6L1 [117, 118], which provides an accurate description to the collision data, has been used.

### 3.1.2 Parton Shower, Underlying Event and Hadronization

In processes that contain charged and/or colored objects in the initial- and/or final-state, gluon and/or photon radiation may give a large correction to the overall topology of the event. After a hard scattering event has been generated, higher order effects are added by using parton shower simulation, which allows partons to split in pairs of other partons (for example,  $g \rightarrow q\bar{q}, q \rightarrow qg$ ). The resulting partons may branch further, leading to a large number of quarks and gluons, which are grouped together into color singlet (or colorless) hadrons known as hadronization, in accordance with the quark confinement model. A schematic diagram depicting the entire process is shown in Fig 3.1.

Perturbative QCD, formulated in terms of quarks and gluons, is valid only at short distances. At long distances, QCD becomes strongly interacting and perturbation theory can not be applied. Hadronization process takes place over relatively larger distances (low momentum exchange) when compared to the hard scattering, so it cannot be modeled by pQCD. A common model used for this is the Lund String Model [119], which is briefly described below.

Lund String model is based on probabilistic and iterative approach. It starts with color field as a one-dimensional ‘string’ between two colored quarks as illustrated in Fig 3.2.

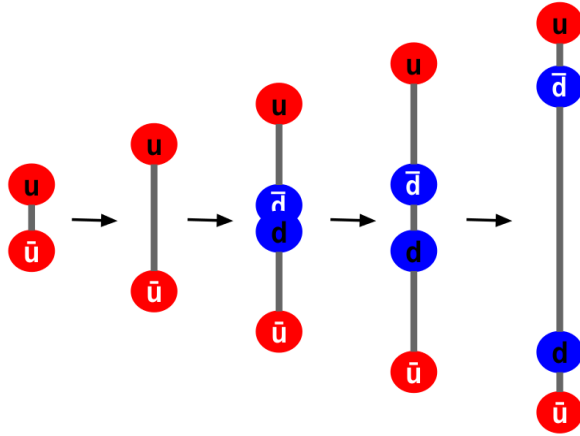


Figure 3.2: Hadronization of an initial state of two quarks where another quark pair is created from the energy stored in the color field.

As the partons ( $u$  and  $\bar{u}$ ) move apart from their common production vertex, the string is stretched between the  $u$  and the  $\bar{u}$ . The transverse dimensions of the string are of the order of the hadronic size ( $\approx 1 \text{ fm}$ ) and are assumed to be uniform along its length. From hadron spectroscopy, the amount of energy per unit length (also sometimes referred to as the string constant) of the string is inferred to be  $\kappa \approx 1 \text{ GeV/fm}$ . As the  $u$  and  $\bar{u}$  move apart, the potential energy of the string increases, and the string may break by creating a new  $q\bar{q}$  (say,  $d\bar{d}$ ) pair, so that we have two color singlet systems  $u\bar{d}$  and  $d\bar{u}$ . The string break up process proceeds until only colorless hadrons remain and then, these themselves may decay into leptons or stable hadrons. The final system of particles emerges aligned roughly along the original  $u\bar{u}$ -axis.

One more important thing that needs to be modelled for generating a real collision-like event is the modelling of the underlying event. The partons left over in the proton after a parton is pulled out to participate in the hard scattering event is referred to as the Beam remnant. They have small  $p_T$  ( $\sim 1 \text{ GeV}$ ), but are connected through color fields to the hard scattering. In MC generators such as PYTHIA, these beam remnants are allowed to interact ( multi parton interaction), shower and decay themselves. The result of these beam remnant interactions is generally referred to as the “underlying events”.

### 3.1.3 Monte Carlo Event Generators

As mentioned earlier, several MC event generators exist in the present day world. Many of these are general-purpose ones while others deal with specific processes. Some of the general-purpose generators include PYTHIA [112], MADGRAPH [113], HERWIG++ [114], ALPGEN [120], and SHERPA [121]. The text in the following subsections briefly describes the details of some of the MC simulation programs used to model the signal and background processes for the search of excited quarks depending on the peculiarity of the respective final states.

#### 3.1.3.1 Pythia

PYTHIA [112] is one of the oldest and well established general purpose MC event generators used for lepton and hadron colliders. It uses the Lund string fragmentation model [119] to describe hadronization and consists of a library of about 240 different hard scattering processes involving 2 incoming partons and 1 or 2 outgoing particle at the LO. It is able to simulate all the generation steps explained earlier. Initial- and final-state showers are added to provide more realistic configurations. The signal samples ( $pp \rightarrow q^* \rightarrow \gamma + \text{jet}$ ), and SM backgrounds QCD  $\gamma + \text{jet}$  and dijet used in this analysis are generated using PYTHIA event generator and are described in more detail in Chapter 5.

#### 3.1.3.2 Madgraph

PYTHIA is an effective event generator for describing  $2 \rightarrow 2$  process but most of the processes observed in experimental collisions have additional hard particles in the final state. The MADGRAPH [113] matrix element generator allows one to simulate amplitude for any process up to 9 particles in the final state. It automatically generates the amplitudes for relevant sub-processes via the ALOHA package [122]. Events are passed as parton level files in the standard event format known as Les Houches format (LHE files) [123]. These LHE files are then passed to PYTHIA for the parton showering and hadronization before passing them to detector simulations. The matching of matrix element (ME) to

parton shower (PS) also happen at this point and it is important to perform the merging to avoid double counting of emissions in overlapping phase space regions. Two methods available to perform the merging are, CKKW algorithm [124], and MLM scheme [125].

The MADGRAPH samples used in this thesis contain LO calculations for pp collisions leading to  $W\gamma$ ,  $W$ +jets, and  $Z\gamma$  in the final state. These backgrounds are discussed in more detail in Chapter 5.

## 3.2 Detector Simulation

The theoretical predictions form an integral part in the planning of the CMS experiment and help define the experimental strategies and design of the detector including software needed for the operation. These predictions need to reproduce the interaction processes taking place in hadron collisions and the interaction of the emerging particles with the various detector systems as closely as possible. After simulating hard scattering to final state particles, further simulation is performed on their interaction within the CMS detector. The complexity of the detector requires very sophisticated programs to properly reproduce the detector behavior in the presence of particles from proton collisions. The detailed simulation is performed within the CMSSW [87] framework using the GEANT4 [126] toolkit. The GEANT4 package relies on accurate description of all aspects of the detector including full geometry, material of the detecting devices and the dead material (e.g. cables, support, cooling etc) to simulate the response to the interacting particle. The core of GEANT4 is a set of physics models to handle the interactions of particles with material over a wide ranges of energy (from few hundreds of eVs to a few TeV). Taking particles from the event generator as input, it propagates them through the detector taking into account the magnetic field (for charged particles) and any interactions between the particle and material such as bremsstrahlung, multiple scattering and photon conversion. Then, the response of detector is built further by emulating the response of the readout and trigger electronics of the detector to the simulated hits, through the pro-

cess of digitization. Noise and other effects are also considered during this step. Finally, a raw output similar to that of the real data event format is obtained. All subsequent stages, such as event reconstruction as described in the next chapter, uses the same input collection and behave identically whether running on simulated events or real data.

### 3.3 Simulated Samples

The complete set of the signal and background MC samples used in this thesis are listed in Table 3.1 and Table 3.2 respectively. All the MC samples were simulated and reconstructed using the CMSSW version 5\_3\_8-patch1.

The  $q^*$  signal MC were generated using PYTHIA 6.426 with the underlying event tune Z2\*. This tune is described in more detail in Ref. [127,128]. To generate  $q^*$  of  $M_{q^*} = 1 \text{ TeV}$  and coupling,  $\Lambda = 1.0$  following set of parameters were used :

```
'MSEL      = 0      !User selected',
'MSTP(6)  = 1      ! excited quark',
'MSUB(147) = 1      ! dg--> d*',
'MSUB(148) = 1      ! ug--> u*',
'PMAS(343,1) = 1000. ! d* mass',
'PMAS(344,1) = 1000. ! u* mass',
'RTCM(41)  = 1000. ! Scale parameter Lambda',
'RTCM(43)  = 1.0    ! f=1   SM coupling',
'RTCM(44)  = 1.0    ! fprime=1 SM coupling',
'RTCM(45)  = 1.0    ! f_s=1 SM coupling',
'4000001:ALLOFF          !Turn off all u* decays',
'4000001:ONIFMATCH 1 22 !Turn on u*->u Photon',
'4000002:ALLOFF          !Turn off all d* decays',
'4000002:ONIFMATCH 2 22 !Turn on d*->d Photon',
```

Here, MSUB=147, 148 refers to the gauge interaction production by quark-gluon fu-

Signal Samples	Events	Cross section (pb)	Couplings
QstarToGJ_M-700_TuneZ2star_8TeV-pythia6	60065	24.85	1.0
QstarToGJ_M-1000_TuneZ2star_8TeV-pythia6	60192	4.18	1.0
QstarToGJ_M-1200_TuneZ2star_8TeV-pythia6	60120	1.552	1.0
QstarToGJ_M-1500_TuneZ2star_8TeV-pythia6	60138	4.124×10 <sup>-1</sup>	1.0
QstarToGJ_M-1700_TuneZ2star_8TeV-pythia6	60256	1.843 ×10 <sup>-1</sup>	1.0
QstarToGJ_M-2000_TuneZ2star_8TeV-pythia6	120105	5.858 ×10 <sup>-2</sup>	1.0
QstarToGJ_M-2500_TuneZ2star_8TeV-pythia6	120127	9.768×10 <sup>-3</sup>	1.0
QstarToGJ_M-3000_TuneZ2star_8TeV-pythia6	120032	1.755×10 <sup>-3</sup>	1.0
QstarToGJ_M-3500_TuneZ2star_8TeV-pythia6	160095	3.241×10 <sup>-4</sup>	1.0
QstarToGJ_M-4000_8TeV-pythia6	159703	6.045×10 <sup>-5</sup>	1.0
QstarToGJ_M-4500_8TeV-pythia6	306561	1.170×10 <sup>-5</sup>	1.0
QstarToGJ_M-700_fhalf_8TeV-pythia6	59013	6.249	0.5
QstarToGJ_M-1000_fhalf_TuneZ2star_8TeV-pythia6	60196	1.064	0.5
QstarToGJ_M-1500_fhalf_TuneZ2star_8TeV-pythia6	60053	1.05×10 <sup>-1</sup>	0.5
QstarToGJ_M-2000_fhalf_TuneZ2star_8TeV-pythia6	120012	1.484×10 <sup>-2</sup>	0.5
QstarToGJ_M-2500_fhalf_TuneZ2star_8TeV-pythia6	120054	2.425×10 <sup>-3</sup>	0.5
QstarToGJ_M-3000_fhalf_TuneZ2star_8TeV-pythia6	120059	4.304×10 <sup>-4</sup>	0.5
QstarToGJ_M-3500_fhalf_TuneZ2star_8TeV-pythia6	160008	7.586×10 <sup>-5</sup>	0.5
QstarToGJ_M-4000_fhalf_8TeV-pythia6	159808	1.258×10 <sup>-5</sup>	0.5
QstarToGJ_M-4500_fhalf_8TeV-pythia6	160000	1.929×10 <sup>-6</sup>	0.5

Table 3.1: MC samples of excited quarks ( $q^*$ ) simulated and reconstructed at  $\sqrt{s} = 8$  TeV, with number of generated events, cross-sections, and coupling strengths.

sion [72],  $\text{RTCM} = 41$  is the compositeness scale parameter  $\Lambda$ , and  $\text{RTCM} = 43, 44, 45$  corresponds to coupling  $f$ ,  $f'$  and  $f_s$  to SU(2), U(1), and SU(3) groups respectively. Signal samples with  $q^*$  mass ranging from 700 GeV up to 4.5 TeV and two set of coupling scenarios,  $f = 0.5, 1.0$  were generated and used for this study. All the coupling multipliers are assumed to be equal throughout the thesis, i.e.,  $f = f' = f_s$ . A complete list of all the samples with total number of generated events and corresponding cross section is shown in Table 3.1.

The SM  $\gamma + \text{jet}$  background samples are generated using the same version of PYTHIA as used for generating  $q^*$  signal samples, with the sub-process choice of  $\text{MSEL} = 10$ . This specifically turns on the simulation of the following sub-processes :  $q\bar{q} \rightarrow \gamma g$ ,  $q\bar{q} \rightarrow \gamma\gamma$ ,  $qg \rightarrow q\gamma$ ,  $\bar{q}g \rightarrow \bar{q}\gamma$ ,  $gg \rightarrow \gamma\gamma$ , and  $gg \rightarrow g\gamma$  in the hard interaction of the proton collision. The inclusion of box diagrams lead to numerically unstable cross sections. Thus, for quark masses below the  $\hat{s}$  scale, the simplified massless expressions are used, which yields a fairly accurate approximation [112]. These events are generated in various  $p_T$  bins as can also

be seen from the name of the samples. The samples are listed in Table 3.2 with prefix *G\_Pt* in their name along with the total number of generated events and corresponding cross sections in units of picobarn (pb).

Signal Samples	Events	Cross section (pb)
G_Pt-120to170_TuneZ2star_8TeV_pythia6	2000043	$1.08 \times 10^2$
G_Pt-170to300_TuneZ2star_8TeV_pythia6	2000069	$3.01 \times 10^1$
G_Pt-300to470_TuneZ2star_8TeV_pythia6	2000130	$2.14 \times 10^0$
G_Pt-470to800_TuneZ2star_8TeV_pythia6	1975231	$2.12 \times 10^{-1}$
G_Pt-800to1400_TuneZ2star_8TeV_pythia6	1973504	$7.08 \times 10^{-3}$
G_Pt-1400to1800_TuneZ2star_8TeV_pythia6	1984890	$4.51 \times 10^{-5}$
G_Pt-1800_TuneZ2star_8TeV_pythia6	1939122	$1.87 \times 10^{-6}$
QCD_Pt-120to170_TuneZ2star_8TeV_pythia6	5985732	$1.56 \times 10^5$
QCD_Pt-170to300_TuneZ2star_8TeV_pythia6	5814398	$3.41 \times 10^4$
QCD_Pt-300to470_TuneZ2star_8TeV_pythia6	5978500	$1.76 \times 10^3$
QCD_Pt-470to600_TuneZ2star_8TeV_pythia6	3994848	$1.14 \times 10^2$
QCD_Pt-600to800_TuneZ2star_8TeV_pythia6	3996864	$2.70 \times 10^1$
QCD_Pt-800to1000_TuneZ2star_8TeV_pythia6	3998563	$3.55 \times 10^0$
QCD_Pt-1000to1400_TuneZ2star_8TeV_pythia6	1964088	$7.38 \times 10^{-1}$
QCD_Pt-1400to1800_TuneZ2star_8TeV_pythia6	2000062	$3.35 \times 10^{-2}$
QCD_Pt-1800toInf_TuneZ2star_8TeV_pythia6	977586	$1.83 \times 10^{-3}$
WGToLNuG_TuneZ2star_8TeV-madgraph	4802358	$5.54 \times 10^2$
WJetsToLNu_TuneZ2Star_8TeV-madgraph	18393090	$3.75 \times 10^4$
ZG_Inclusive_8TeV-madgraph_v2	6321549	$1.72 \times 10^2$

Table 3.2: Background MC samples simulated and reconstructed at  $\sqrt{s} = 8$  TeV.

The SM QCD dijet samples are also generated with PYTHIA 6.426 and has the subprocess, MSEL=1. This include sub-processes :  $q_i q_j \rightarrow q_i q_j$ ,  $\bar{q}_i \bar{q}_j \rightarrow \bar{q}_i \bar{q}_j$ ,  $q_i \bar{q}_i \rightarrow q_k \bar{q}_k$ ,  $q_i \bar{q}_i \rightarrow gg$ ,  $q_i g \rightarrow q_i g$ ,  $gg \rightarrow q_k \bar{q}_k$ ,  $gg \rightarrow gg$ . All of these are LO  $2 \rightarrow 2$  processes with cross sections  $\propto \alpha_s^2$ . Initial- and final-state radiations are added using parton showering [112] to generate multijet events. These samples are also generated in different  $p_T$  bins and are listed in Table 3.2 with prefix *QCD\_Pt*.

All the other backgrounds viz.  $W\gamma$ ,  $W$ +jets, and  $Z\gamma$  are generated using MADGRAPH and are listed in the last three rows of the Table 3.2 with number of generated events and their respective cross sections.

## 3.4 Data Samples

This thesis is based on the data sample recorded by the CMS detector during the year 2012 in stable proton-proton collisions at a center-of-mass energy of  $\sqrt{s} = 8 \text{ TeV}$ , corresponding to an integrated luminosity of  $19.7 \text{ fb}^{-1}$ . Only certified runs and luminosity sections were selected based on the official golden JSON file mentioned in Table 3.3, which means that a good functioning of all the CMS sub detectors is mandatory. The events are triggered

Data Sample	Label	Run Range	Luminosity (fb $^{-1}$ )
/Photon/Run2012A-22Jan2013-v1	A	190456-193621	0.876
/SinglePhoton/Run2012B-22Jan2013-v1	B	193833-196531	4.421
/SinglePhoton/Run2012C-22Jan2013-v1	C	198022-203742	7.055
/SinglePhotonParked/Run2012D-22Jan2013-v1	D	203768-208686	7.369
Total 2012 Data		190456-208686	19.712
JSON file			
Cert_190456-208686_8TeV_22Jan2013ReReco_Collisions12_JSON.txt, located at -			
<a href="https://cms-service-dqm.web.cern.ch/cms-service-dqm/CAF/certification/Collisions12/8TeV/Reprocessing/">https://cms-service-dqm.web.cern.ch/cms-service-dqm/CAF/certification/Collisions12/8TeV/Reprocessing/</a>			

Table 3.3: List of datasets with corresponding Run Range, Luminosity, and JSON file. All the datasets uses AOD tier of the data format.

by the single photon trigger, hence is the name *SinglePhoton* for the dataset. The dataset is divided into four periods labeled as A, B, C, and D, and includes run numbers from 190456 to 208686 as listed in Table 3.3. The events considered for the analysis are taken from the AOD tier of data format and are processed using 5\_3\_8\_patch3 version of the CMSSW.



# Chapter 4

## Event Reconstruction and Object Identification

Particles emanating from parton-parton interaction in the CMS detector and impinging on various layers of the detector leave behind distinct signatures in different detector material via strong and electromagnetic interactions, enabling an event-by-event reconstruction. Reconstruction, here, means the creation of physics quantities and objects from either the raw data measured by the DAQ system or from the simulated electronic response. These data, in either case, are called *digi*s. All charged particles leave signals in silicon strips and pixels as they traverse the tracker. Electrons, photons and some neutral hadrons deposit most of their energy in the ECAL via electromagnetic showers, whereas all charged and most of the neutral hadrons shower in the HCAL. Muons having a mass of about 200 times that of the electrons, lose very small amount of energy as they pass through the matter and are also referred to as minimum ionizing particles, mostly leave the calorimeters without showering. An illustration of particle interactions within the CMS detector is shown in Fig 4.1.

The CMS experiment makes use of various reconstruction algorithms [129], broadly divided into three steps as shown in Fig 4.2, to interpret the raw digital information coming from the detector channels and yield the physics objects with associated charge, energy

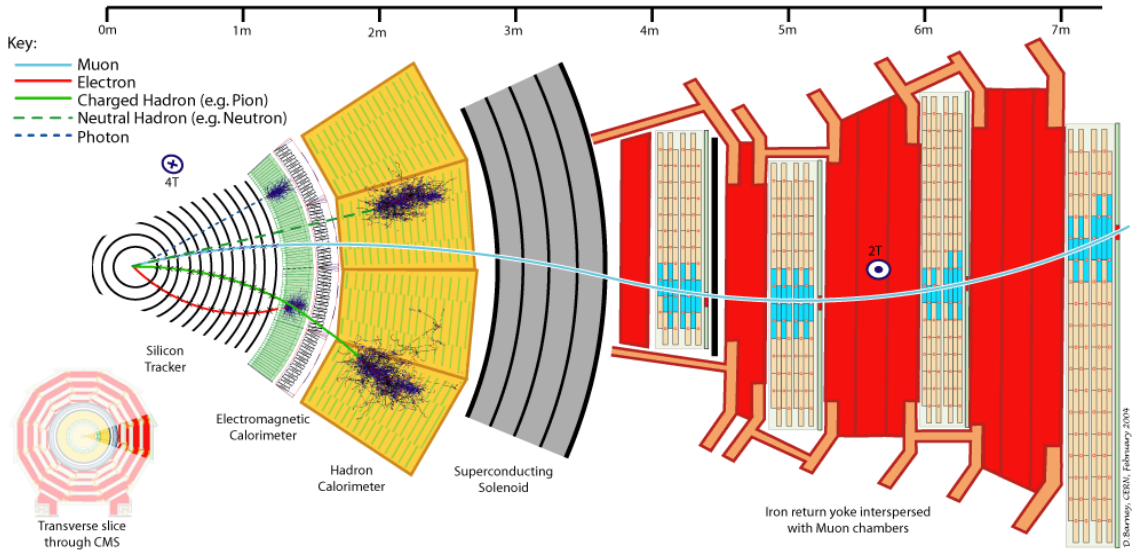


Figure 4.1: Transverse view of the CMS detector, showing particle identification [85].

and position measurements, with these, in turn, to be used in a wide range of physics analyses. First, a local reconstruction in individual sub-detector modules is performed, which produces reconstructed hits (in short “*rechit*”) representing position measurements in case of tracker and muon system, or clusters representing energy deposited in case of the calorimeters. Subsequently, information from different sub-systems, such as tracker, calorimeters, and the muon system, is used to reconstruct physics objects such as electrons from tracks; and photons and jets from calorimeter clusters, etc. Finally, a holistic approach, known as the particle-flow event reconstruction (PF) [130, 131] is used, where information from all sub-detectors is linked in an attempt to individually and coherently reconstruct and identify particles such as photons, leptons, pions, etc., in a given event. Composite objects, such as jets,  $E_T^{\text{miss}}$ , hadronically decaying  $\tau$  leptons, are then finally created using these PF particles.

In this chapter, we begin with the description of track reconstruction in the tracker system, followed by the primary vertex reconstruction. Then, we concentrate on describing the reconstruction and identification of photons and jets in the calorimeters, for these are the physics objects of interest used in “Search for excited quarks in a photon and jet final state”, presented in this thesis.

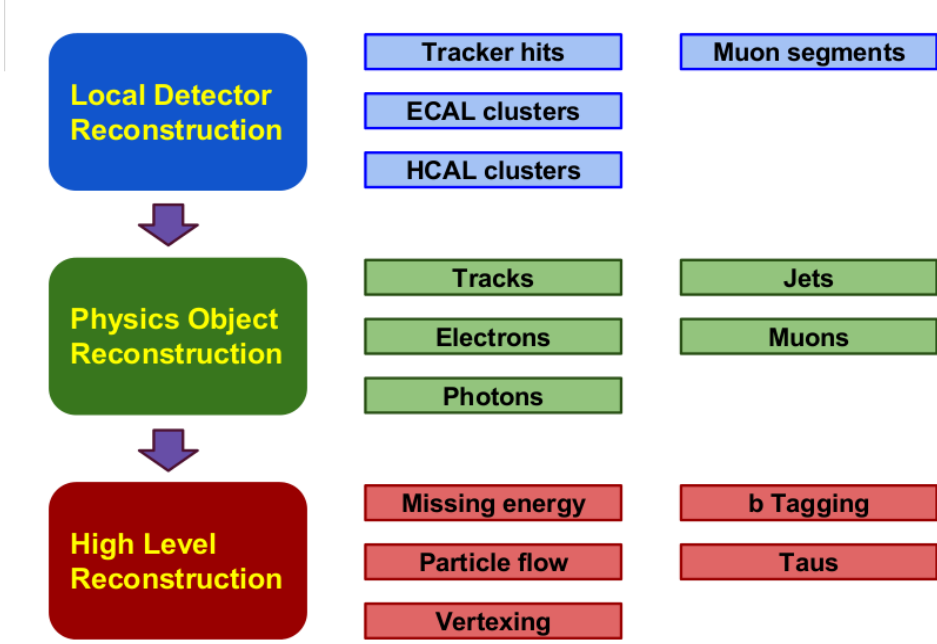


Figure 4.2: Flowchart of event reconstruction algorithms.

## 4.1 Track Reconstruction

The reconstructed tracks of charged particles form the most fundamental objects in the reconstruction of collision events, subsequently contributing to the reconstruction of electrons, muons, taus, and hadronic objects as well as determination of primary interaction and displaced vertices. For each bunch crossing, few hundreds to a thousand charged particles travel through the CMS tracker system. In such an environment, the tracking software aims to perform efficient reconstruction over a wide range of transverse momenta from 100 MeV to 1 TeV, while keeping the misidentification rate low. These challenges are overcome by using the Combinatorial Track Finder (CTF) algorithm [94, 132] iteratively.

The tracking is done in several steps or iterations (6 in this case). The basic idea is to search for tracks with relatively large  $p_T$ , produced near the interaction region. After each iteration, hits associated with tracks found in all preceding iterations are not considered so as to reduce the combinatorial complexity and simplify subsequent iterations in the search for low- $p_T$  tracks. Iteration-0 starts by reconstructing the highest quality tracks with  $p_T > 0.8$  GeV, identified as those having highest  $p_T$ , consistent with the primary

vertex, and contain three pixel hits (indicating the track went through each layer of the pixel detector). In iteration-1, remaining high  $p_T$  tracks with only two pixel hits and close to the interaction point are reconstructed. Iteration-2 collects low  $p_T$  tracks originating from the primary vertex. These first three iterations reconstruct prompt tracks with an efficiency of  $\sim 90\%$  for charged hadrons and  $\sim 99.5\%$  for muons. Finally, Iterations-3 to 5 reconstruct the tracks that originate outside the luminous region of the collision and are not found in previous iterations.

Each iteration is composed of four logical steps – seed generation; pattern recognition or track finding; track fitting; and ambiguity resolution or track selection. While we describe these below, further details can be found in Ref. [94].

- *Seed generation:* The seed defines the initial trajectory parameters and associated uncertainties of possible tracks. A track seed is built from either two or three hits in different layers of the pixel detector and is used to make an initial estimate of the trajectory parameters, i.e., track  $p_T$ , its position and associated uncertainties. The trajectory of charged particles follow a helical path.
- *Pattern recognition or track finding:* The Kalman filter algorithm<sup>1</sup> [133] makes use of the track parameters given by the trajectory seed for track finding. It extrapolates the trajectory of each track seed outwards by adding the collection of hits from successive layers of the tracker. The hits are fit using the Kalman filter technique and a  $\chi^2$  test as defined in Ref. [94] is used to check the compatibility of the hits with the extrapolated trajectory.
- *Track fitting:* Once the candidate track has been found in the pattern recognition stage, tracks are fit again to remove any bias introduced at the seeding step and obtain a final estimate of the trajectory parameters. First, a Kalman filter fit is performed on the first few hits of the track candidates. Then, the result of this

---

<sup>1</sup> Kalman filter is an estimation technique, that provides efficient means (recursively) to infer the state of a process, such that the mean squared error of the estimated parameter is minimized. The filter is so effective that it can estimate the parameters precisely even when the modelled system is unknown. More details about the same can be found in Ref. [133]

fit and the innermost hit is used to initialize a Kalman filter fit to the entire track candidate. The result is finally smoothed by averaging its result with a second fit performed in the reverse direction (the outermost hit to the innermost). A check is also done to find if there are any spurious hits (outliers) associated with the track. The outliers are found based on the probability that a pixel is consistent with the track, after taking into account the charge distribution of the hit in the pixel. The outlier hits are removed from the track, and the process is repeated until no outliers exist.

- *Track selection, or Ambiguity resolution:* In an event, there is a finite probability that the track finding procedure may yield a few fake tracks, namely reconstructed tracks not associated with charged particles. The fake rate (fraction of reconstructed tracks that are fake) can be substantially reduced by using certain quality requirements. Track quality criteria including requirement on the number of layers in a track, the  $\chi^2$  per degree of freedom (number of tracker layers that have hits) of the track, and its transverse and longitudinal impact parameters are used to remove fake tracks. After passing the above selection criteria, the track candidate is finally referred to as a track, or otherwise discarded.

## 4.2 Reconstruction of Primary Vertices

Interaction vertices or primary vertices (PV) are determined from the track collection. It is done in three steps. First, the tracks are selected, second, the clustering of tracks is done corresponding to a vertex, and finally, each group of tracks is fit to determine the position of the vertices.

The location of the primary interaction vertex is reconstructed using pixel tracks with  $p_T$  in excess of 1 GeV and a transverse impact parameter less than 1 mm with respect to the beamspot [134]. These tracks are then clustered along the beam axis ( $z$ -direction) by requiring a separation of at least 1 cm between clusters. The clustering determines how

many primary vertex candidates exists and how to assign the tracks to them. Finally, each cluster of tracks assigned to a primary vertex candidate is fit with the Adaptive Vertex Fitter (AVF) [135] to determine the PV parameters, including its position. The AVF is an iterative Kalman Filter where tracks in each vertex are weighted according to their compatibility with the PV. This adaptive vertex fitter does not reject outlying tracks. Instead it down-weights outliers with a weight, given by:

$$w_i(\chi_i^2) = \frac{\exp(-\chi_i^2/2T)}{\exp(\exp(-\chi_i^2/2T) + \exp(-\chi_c^2/2T))} \quad (4.1)$$

where  $w_i$  is the probability that a track,  $i$  belongs to a vertex. The constant  $\chi_c^2$  is the threshold where the weight has a value 1/2. Below this value, a track is considered a outlier. The variable  $T$  is a parameter that controls the shape of the functional dependence. More details of vertex reconstruction can be found in Refs. [94, 135, 136]. The vertex candidates are finally sorted in decreasing order according to the sum of their track  $p_T^2$ . The candidate with largest sum is considered as the primary vertex. The PV resolution is  $10 - 12 \mu\text{m}$  in all the three dimensions.

## 4.3 Photons

Photons produced in pp collisions or from decay of other particles deposit their energy in the crystals of the ECAL via electromagnetic interactions. The photon reconstruction algorithms [137] reconstruct the energy and momentum of the photon candidates from these ECAL crystals.

### 4.3.1 Photon Reconstruction

The reconstruction of photons [137] begins with the recovery of the energy deposited by them into the ECAL. In the absence of any material in-between the collision point and the calorimeters, about 97% of the photon energy would be contained in a  $5 \times 5$  cluster of the ECAL crystals. For electrons too, one uses a similar reconstruction technique

with additional information from the tracker system. The presence of material in front of the ECAL causes electrons and positrons to undergo bremsstrahlung and photons to convert into  $e^+e^-$  pairs. As bremsstrahlung emissions have effects analogous to that of pair-production, the same clustering algorithms are employed for both electron and photon reconstruction. The solenoidal magnetic field causes the energy reaching the ECAL to spread in the  $\phi$ -direction, whereas the distribution of energy in the  $r - z$  plane is unaffected due the magnetic field. To account for this energy spread, electrons and photons are reconstructed from clusters of the ECAL crystals, called superclusters (SCs). The main aim of the clustering algorithms is to group neighboring crystals to collect energy deposited by the electromagnetic shower in the ECAL. Two different clustering algorithms, namely, “Hybrid Clustering algorithm” and “Multi5  $\times$  5 algorithm” are used to find SCs, respectively in EB and EE, based on the differences in position and geometry of the crystals [137–139].

#### 4.3.1.1 Hybrid Algorithm

The clustering in the EB region takes advantage of the  $\eta - \phi$  geometry of the crystals. The algorithm [138, 139] works by collecting energy within a rectangular window spread in the  $\phi$ -direction, and crystals sorted in the decreasing order of  $E_T$ . We give, below, a brief description of the algorithm.

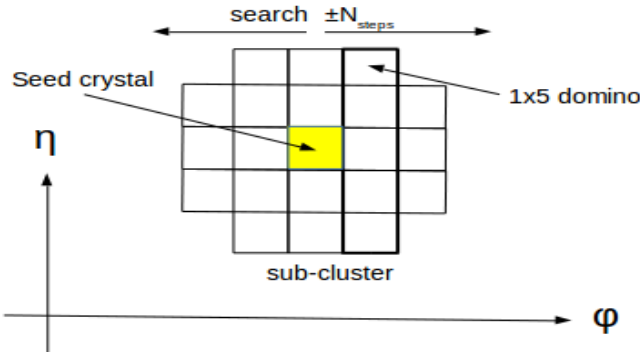
- Hybrid clustering algorithm starts with a search for a seed crystal, defined as the crystal with the highest energy deposit, with the requirement that  $E_{T,seed} > E_{T,seed}^{\min}$ . Clustering terminates if no such crystal is found.
- Once the seed crystal is found, arrays of  $1 \times 5$  crystals (also called dominos) with energies greater than  $E_{array}^{\min}$  are added in  $\phi \times \eta$  plane around the seed crystal, in a range of  $N_{steps}$  crystals in both directions of  $\phi$ .
- The adjoining arrays are then grouped into clusters, where each cluster is required to have a seed array with energy in excess of  $E_{seed-array}^{\min}$  in order to be added to the

final cluster, known as the supercluster (SC).

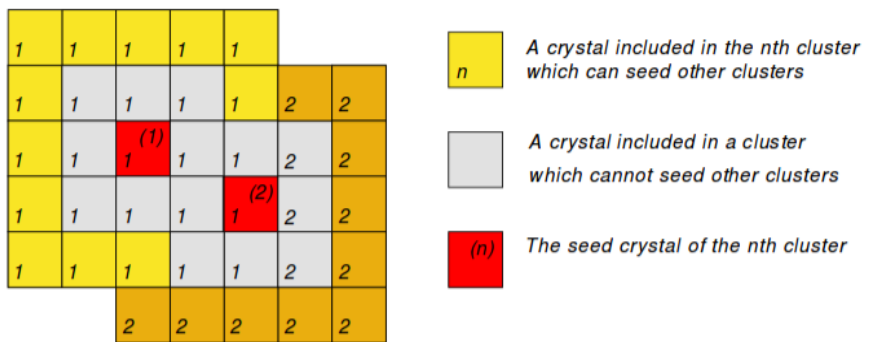
The values for various parameters used in the algorithm defined above are listed in Table 4.1 and the procedure is illustrated in Fig 4.3a.

Parameter	Value
$E_{T,\text{seed}}^{\min}$	1 GeV
$N_{\text{steps}}$	17 crystals
$E_{\text{array}}^{\min}$	0.1 GeV
$E_{\text{seed-array}}^{\min}$	0.35 GeV

Table 4.1: Parameter values used in Hybrid algorithm.



(a) A depiction of Hybrid Clustering algorithm used in EB region.



(b) Two overlapping Multi5x5 clusters. Crystals with yellow colour can potentially seed further multi5x5 clusters.

Figure 4.3: Schematic overview of clustering algorithms in barrel and endcap ECAL regions [139].

#### 4.3.1.2 Multi5 $\times$ 5 Algorithm

The hybrid algorithm [138, 139] can't be applied in the EE region, since unlike the EB region the crystals are not arranged in an  $\eta - \phi$  geometry in this region. Thus, the Multi5  $\times$  5 algorithm, which tries to implement the same idea in a different fashion, is used. As described below, it also operates on crystals sorted in descending order in deposited  $E_T$ .

- First, search for a crystal which does not already belong to a cluster and begin the clustering procedure with a seed crystal satisfying  $E_{T,seed} > E_{T,EEseed}^{\min}$ .
- Check if the energy deposited in the seed crystal is a local maximum by comparing it to those deposited in the four nearest neighbors on each side in a Swiss Cross pattern. If it is not, go back to previous step.
- Cluster a 5  $\times$  5 matrix of crystals around the seed crystal, including only those crystals that do not already belong to a cluster.
- To collect overlapping deposition due to bremsstrahlung, the outer 16 crystals of the 5  $\times$  5 matrix are allowed to seed new matrices but the crystals already included in a cluster can not belong to another one.

Finally, superclusters are built by summing up all the clusters satisfying  $E_{T,cluster} > E_{T,cluster}^{\min}$  and lying within a range  $\eta \pm \Delta\eta_{road}$  and  $\phi \pm \Delta\phi_{road}$  around each seed crystal. The parameter values used for this algorithm are listed in Table 4.2 and its pictorial representation is shown in Fig 4.3b.

Parameter	Value
$E_{T,EEseed}^{\min}$	0.18 GeV
$E_{T,cluster}^{\min}$	1 GeV
$\Delta\eta_{road}$	0.07
$\Delta\phi_{road}$	0.3 rad

Table 4.2: Parameter values used in Multi5  $\times$  5 algorithm.

The ECAL endcap region, i.e.,  $(1.6 < |\eta| < 2.5)$  is covered by the ECAL preshower (ES) detector. Electrons and photons traversing in this region deposit some of their energy in the preshower, so this energy needs to be measured and must be added to each cluster. To get the total energy of the showering particle for each super cluster the corresponding energy of the ES strips, found at the position of intersection formed by extrapolating the position of the SC towards the interaction point, is added to it.

Regardless of the clustering algorithm, the position of the supercluster is estimated through a weighted average of the position of all the crystals, where each crystal contributes with a weight,  $w_i = \max(0, 4.7 + \ln(E_i/E_{SC}))$  [140]. The superclusters are subsequently promoted to photon candidates and the direction of the photon momentum is estimated by connecting the position of the supercluster to that of the primary vertex in the event. If several primary vertices are found, the one with the highest scalar sum of track  $p_T^2$  is chosen.

#### 4.3.1.3 Energy Corrections

Measuring the energy of electromagnetic objects with very high resolution is essential for precision measurement of the SM parameters and searches beyond the SM. A precise measurement of energy deposition in the calorimeters can also help improve measurement of  $E_T^{\text{miss}}$ , which is another important quantity for various new physics searches. Numerous factors can effect ECAL energy resolution, such as interaction of electromagnetic particles with the material of the tracker system, leading to bremsstrahlung and pair-production and, thus, energy loss. The role of the supercluster energy correction [139] is to compensate for these energy losses and to control energy scales and achieve a homogeneous response in the full calorimetric volume. The reconstructed photon energy is given by:

$$E_\gamma = F_\gamma \times G \times \sum_{i=1..N} c_i \times A_i \quad (4.2)$$

where,  $A_i$  are the digital amplitudes in the ADC counts;  $c_i$  are the inter-calibration terms that equalize the responses of the different crystals;  $G$  is the global energy scale defined in such a way that sum of amplitudes of a  $5 \times 5$  crystal matrix multiplied by  $G$  amounts to the total energy of an incident unconverted photon. The factor  $F_\gamma$  represents a correction term to the supercluster energy and receive contribution from three types of effects, as described below:

- **Variation of shower containment** as a function of the position in the detector is parametrized by a function  $C_{EB}(\eta)$ . It is important only in the EB region, where the non-uniformities in the lateral shower leakage need to be corrected because of the off-pointing geometry of the crystals.
- **Variations in algorithm response** to different SC topologies are corrected through a function,  $f_{brem}$ , where,  $brem$  is the energy loss due to bremsstrahlung, characterized by

$$brem = \frac{\sqrt{\sum_i \frac{E_i}{E_{SC}} (\phi_i - \phi_{SC})^2}}{\sqrt{\sum_i \frac{E_i}{E_{SC}} (\eta_i - \eta_{SC})^2}} \quad (4.3)$$

where the sum  $i$  runs over all the crystals in the SC and  $\eta_{SC}, \phi_{SC}$  refers to the SC position. This function is almost insensitive, within certain limits, to the amount of material in front of the calorimeter. This contribution is  $\lesssim 7\%$  in the EB region, and  $\lesssim 20\%$  in the EE region [139].

- **Residual variations** due to non-uniform distribution of material in the detector, and the energy dependence of the energy-collection efficiency need to be corrected with a factor  $f(E_T, \eta)$ .

### 4.3.2 Photon Identification

The most significant background to direct photon final state are QCD processes, where jets fragment to light neutral mesons, such as  $\pi^0$  and  $\eta$ , which, subsequently, decay into a pair of overlapping photons. Thus, in order to maintain purity of the photon signal

selection, the separation of the prompt photon component from this background at high energies must be done with great purity.

Even though an event-by-event discrimination of signal photons from the background is not possible, a separation of signal and background is possible on a statistical basis. An effective instrument used to segregate signal from background is based on the topology of the deposited energy in the calorimeter. Several variables sensitive to differences between signal and background photons can be constructed and are classified under the heading “shower shape variables”. The electromagnetic shower from neutral mesons contributing to the background are produced in jets, and thus are always surrounded by some hadronic activity. The resultant showers are wider than one produced from a prompt photon because of the overlapping nature of two showers merging into one from two photons emanating from neutral meson. The jet backgrounds can, therefore, be reduced by requiring the reconstructed supercluster in the ECAL to be isolated, i.e., limiting the amount of energy carried by other particles surrounding them. The following sections briefly describes different types of variables used to identify and isolate prompt photons.

#### 4.3.2.1 Shower shape variables

The shower topology is an important discriminator to distinguish prompt photons from photons coming from neutral mesons. Several variables can be computed to parametrize the differences between the events due to prompt photons and those coming from neutral hadrons in jets.

**Hadronic over Electromagnetic ratio (H/E) :** It is defined as the ratio of the energy deposited in the HCAL behind the photon supercluster and the photon energy as measured by the ECAL. The ratio H/E is the energy deposited in the single closest HCAL tower to the supercluster position inside a cone of radius 0.15 in the  $\eta - \phi$  plane centered on the photon direction to the energy deposited in the ECAL for that supercluster. Since the ECAL has sufficient depth (measured in  $X_0$ ) to contain the shower within it and the probability of shower leakage into the HCAL is very small, this is a good discriminator.

**Rectangular ratios :** The hypothesis of a single photon shower against multiple overlapping showers can be tested by searching for a double peak structure in the topology of the supercluster. The simplest of variables sensitive to this feature can be computed as the ratio of energy deposited in a  $n \times m$  crystal window around the supercluster seed crystal to the energy deposited in a  $n' \times m'$  window or the total supercluster energy. Two such variables used are called  $R_1$  and  $R_9$ , where  $R_1$  is defined as the ratio of seed crystal energy to the supercluster energy while  $R_9$  is the ratio of energy deposited in a  $3 \times 3$  window to the supercluster energy.

**Shower profile :** A sophisticated way to look at a possible double peak structure is to determine the lateral extension of energy deposits in the  $\eta$ -direction. A variable,  $\sigma_{i\eta i\eta}$ , defined as the energy weighted standard deviation of a single crystal  $\eta$  within a  $5 \times 5$  crystal lattice centered at the crystal with maximum energy, gives the transverse shape of the electromagnetic cluster. It is computed with logarithmic weights and is expressed as:

$$\sigma_{i\eta i\eta}^2 = \frac{\sum (\eta_i - \bar{\eta})^2 w_i}{\sum w_i}, \quad (4.4)$$

where  $\bar{\eta} = \frac{\sum w_i \eta_i}{\sum w_i}$  and  $w_i = \max \left[ 0; 4.7 + \log \left( \frac{E_i}{E_{5 \times 5}} \right) \right]$

where the sum runs over the  $5 \times 5$  crystal matrix around the most energetic crystal in the supercluster, and the  $\eta$  distances are measured in units of the crystal size in the  $\eta$ -direction. This variable helps in discriminating the clusters belonging to the prompt photon for which the distribution is narrow and symmetric when compared to misidentified photons, for which there is a tail in the lower side of the distribution.

**Conversion safe electron veto :** This variable requires that there be no charged particle track with a hit in the pixel detector not matched to a conversion vertex [137], pointing to the direction of photon cluster in the ECAL. It helps to distinguish photons from electrons.

#### 4.3.2.2 Isolation based variables

The fact that prompt photons arising from the interaction vertex are not produced in association with other particles can be used to construct various isolation sums. The signal photon candidates can be extracted by simply allowing a maximum threshold to the amount of allowed activity surrounding the photon candidates in various sub detectors. These isolation sums can be expressed as the total amount of energy/momentum carried by particles estimated using particle flow algorithm, surrounding the photon candidate. Three types of sums : the total energy carried by the charged hadrons, the neutral hadrons and the photons, have been employed in this thesis. All the three sums are evaluated in a cone of radius  $R = \sqrt{\Delta\eta^2 + \Delta\phi^2} = 0.3$  around the photon candidate. Respective veto regions are defined for each isolation sum, with the motive to isolate the energy deposits due to the photon candidates.

**Particle Flow Charged Hadron Isolation:** Sum  $p_T$  of all charged hadrons within a hollow cone of  $0.02 < \Delta R < 0.3$  around the supercluster to isolate showers arising from non-converted or late converted photons having no associated track in the tracker system.

**Particle Flow Neutral Hadron Isolation:** Sum  $p_T$  of all neutral hadrons within a cone of  $\Delta R = 0.3$  around the supercluster because the clusters having energy deposition from neutral hadrons will lead to a broader distribution of energy compared to isolated photons, as well as leakage in the HCAL.

**Particle Flow Photon Isolation:** Scalar sum  $p_T$  of all photons within a cone of  $\Delta R = 0.3$  excluding a strip in  $\eta$  of 0.015 around the supercluster, to separate from converted photons going in to  $e^+e^-$  and having a broader spread in  $\eta$ -direction.

#### 4.3.2.3 Anomalous ECAL energy deposits

Anomalous energy deposits (such as noise) in the ECAL are a source of background while identifying photons from pp collisions. These deposits of energy are caused by direct ionization of an Avalanche Photo-diode (APD) by a highly ionizing particle such as a proton [141]. In such a case, the entire energy is deposited in a single crystal and this

is referred to as a “spike”. The rate of these spikes scales with  $\sqrt{s}$  at a level which is consistent with the increase in charged particle multiplicity from pp collisions [142].

The pulse shape of a signal and timing of the shower development in the ECAL allows distinction between the energy deposits by true electromagnetic showers and those from direct ionization of an APD. While the “spikes” due to electronic noise in APD peaks instantaneously and deposits most of the energy in a single crystal, the signal from electromagnetic showers take time to develop and attain a maximum spread over several crystals.

#### 4.3.2.4 Beam Halo

Protons from LHC beams may collide with atomic nuclei of gas atoms or other material along the beam line. These interactions results in a “halo” of particles which tend to be nearly parallel to the beam direction. These “halo” particles are composed of mainly baryons, mesons, and muons. Muons from beam halo can penetrate through large amounts of detector material including the endcaps of the CMS. These muons may also interact with material in CMS and create photons from bremsstrahlung. The resulting photons from these interactions can be detected by the ECAL and tend to be relatively isolated. Photons coming from pp collisions at the interaction point are reconstructed with a  $t_{seed}^2 \approx 0$ , while those resulting from beam halo tend to have a negative  $t_{seed}$ .

## 4.4 Jets

The quarks and gluons jets have played an important role in establishing QCD as the theory of the strong interactions within the SM. A jet is referred to as collimated spray of hadrons, reflecting the configuration of quarks and gluons at short distances. Thus, by analysing the energy and angular distributions of the jets, the properties of the strong forces acting between them can be studied. Clustering the energy deposits or momentum measured by tracker system from a large collection of particles into one or more jets is

---

<sup>2</sup> $t_{seed}$  is the timing of the seed crystal, the highest energy crystal in the cluster.

done by a jet clustering algorithm. Jet reconstruction algorithms provide a set of rules, based on proximity, for clustering of particle tracks or calorimeter towers into jets. A good jet reconstruction algorithm needs to address the following set of issues:

- It should be simple and easy to implement in an experimental analysis and theoretical calculations and should be independent of detector structure.
- It should yield a finite cross section at any order in perturbation theory and also be relatively insensitive to hadronization effects.
- It should be infrared and collinear safe.
- It should be fully specified, including defining in detail any pre-clustering, merging and splitting.

Infrared and collinear safety is a fundamental requirement for jet algorithms. Infrared safety ensures that adding a soft gluon would not effect the jet clustering results while collinear safety take cares that the splitting of one parton into two partons leads to similar results in jet clustering. The configurations of infrared and collinear safety are shown separately in Fig 4.4. For the analyses presented in this thesis, jets are reconstructed and identified using the “particle-flow” (PF) [130] event reconstruction and anti- $k_T$  jet [143] clustering algorithm, which are described in brief detail in the sections to follow.

#### 4.4.1 Particle Flow Reconstruction

The “particle flow” (PF) [130] approach is an attempt to identify and reconstruct individually each particle originating from the pp collisions via coherent use of all sub-detectors. The PF algorithm is designed to maximally exploit the high efficiency tracking and high granularity calorimetric (especially ECAL) system of the CMS detector. The PF jets are composed of individually identified charged hadrons, photons, electrons, and neutral hadrons in the barrel region, i.e., within the reach of the ECAL and the tracker. It leads

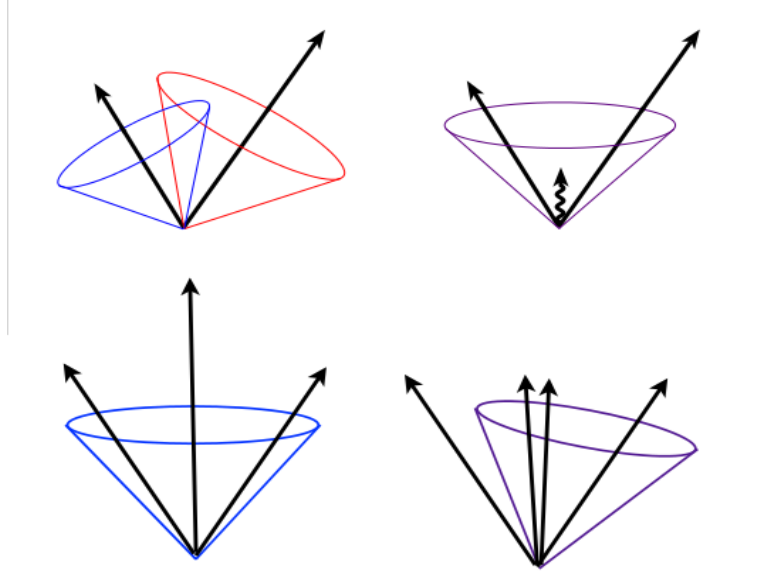


Figure 4.4: Infrared safety (top) : Addition of a soft gluon. Collinear safety (bottom) : Splitting of one parton into two collinear partons.

to an optimal determination of the direction, energy, and type of particle in each event. The PF algorithm consists of mainly three steps.

The *first step* begins with making *building bricks/elements* of the PF algorithm, i.e., reconstruction of charged particle tracks and clusters of calorimeter energy deposits. Tracks are obtained as described in Section 4.1, while the clusters are built using a dedicated PF clustering algorithm tuned to achieve high detection efficiency. The clustering procedure starts with a search for seeds, which correspond to energy deposits in calorimetric channels with a local maxima. The nearest neighboring channels are then added to it, forming *topological clusters*. Energy deposits in each calorimeter channel is required to be above predetermined thresholds both for ECAL and HCAL in order to avoid contributions from electronic noise fluctuations. Finally, the positions and energies of clusters are determined iteratively by re-weighting the individual channel contributions as per the channel-cluster distance [144].

The *second step* constitutes the reconstruction of PF *blocks* in the PF event reconstruction. As a single particle impinging the detector can result in multiple PF *elements* in the form of clusters and tracks, and in order to eliminate the possibility of double

counting within the PF collection, they need to be connected via a mechanism called *link algorithm*. All the tracks are extrapolated starting from the last hit measured in the tracker system, to the ECAL and HCAL, at depths compatible with the electron and hadron shower profile respectively, and clusters that are found to include the extrapolated tracks within their boundaries, are linked to the track. A link between ECAL (including the preshower detector) and HCAL clusters is also made when the position of the cluster in ECAL lies within the envelope of the HCAL cluster. Going further, tracks from the tracker system are also linked to the tracks in the muon system forming the global and tracker muon candidates. A resultant block is usually composed of  $\leq 3$  elements, and the quality of a block is defined by the compatibility of its constituent elements, either as the  $\eta - \phi$  distance in the case of track-to-cluster and cluster-to-cluster links or a global fit  $\chi^2$  for track-to-muon-track links. The limited size of each PF block renders the PF particle identification performance almost independent of event complexity [130].

The *third step* refers to the reconstruction and identification of each PF particles based on these PF *blocks*. The detailed reconstruction in the context of each particles is explained in [130].

#### 4.4.2 Anti- $k_{\mathrm{T}}$ Clustering Algorithm

The anti- $k_{\mathrm{T}}$  algorithm [143] is an infrared and collinear safe clustering algorithm used as the default jet reconstruction algorithm. The anti- $k_{\mathrm{T}}$  is a special form of  $k_{\mathrm{T}}$  algorithm [145], that is a clustering based, sequential recombination algorithm. For a given set of input objects, it evaluates two distance measures for each object, namely, the distance  $d_{ij}$ , between  $i^{\mathrm{th}}$  and  $j^{\mathrm{th}}$  objects, and the distance  $d_{iB}$ , between the  $i^{\mathrm{th}}$  object and the beam line  $B$ , shown in Eq 4.5 to 4.7.

$$d_{ij} = \min(k_{\mathrm{T}i}^2, k_{\mathrm{T}j}^2) \frac{\Delta R_{ij}^2}{R^2} \quad (4.5)$$

$$d_{iB} = k_{\mathrm{T}i}^2 \quad (4.6)$$

$$\Delta R_{ij}^2 = (\eta_i - \eta_j)^2 + (\phi_i - \phi_j)^2 \quad (4.7)$$

where  $k_T$  is the object transverse momentum,  $\eta$  and  $\phi$  are object pseudo-rapidity and azimuthal angle, respectively, and  $R$  is the predefined jet radius. The functioning of  $k_T$  algorithm can be briefly summed up as follows:

- Make list of particles and compute distances  $d_{ij}$  and  $d_{iB}$ .
- If  $d_{ij}$  is smaller, entities  $i$  and  $j$  are combined into a jet and return to first step.
- Otherwise, if  $d_{iB}$  is smaller, the entity  $i$  is pronounced as jet and removed from the list and return to first step.
- Repeat until no particles are left.

The distance measurement can also be generalized as,

$$d_{ij} = \min(k_{Ti}^{2p}, k_{Tj}^{2p}) \frac{\Delta R_{ij}^2}{R^2} \quad (4.8)$$

$$d_{iB} = k_{Ti}^{2p} \quad (4.9)$$

where,  $p$  is the parameter that is 1 for  $k_T$  algorithm and it implies that soft particles are clustered first. When  $p = -1$ , it refers to the anti- $k_T$  algorithm, and in this case hard particles are clustered first rather than soft particles. For  $p = 0$ , an energy independent clustering algorithm known as Cambridge/Aachen (CA) algorithm [146] is obtained. The behaviors of different jet algorithms are illustrated in Fig 4.5. Figure 4.5 also illustrates SIScone jet algorithm that is based on the search for stable cones. Other than being infrared and collinear safe, the anti- $k_T$  jet algorithm also gives the best shape which helps in applying topological selections. The CMS supports anti- $k_T$  algorithm with cone sizes  $R = 0.5$  and  $R = 0.7$ .

#### 4.4.3 Jet Energy Calibrations

Energy measurement of the reconstructed jet is, typically, different from the corresponding true particle jet energy, owing mainly to non-uniform and non-linear response of the

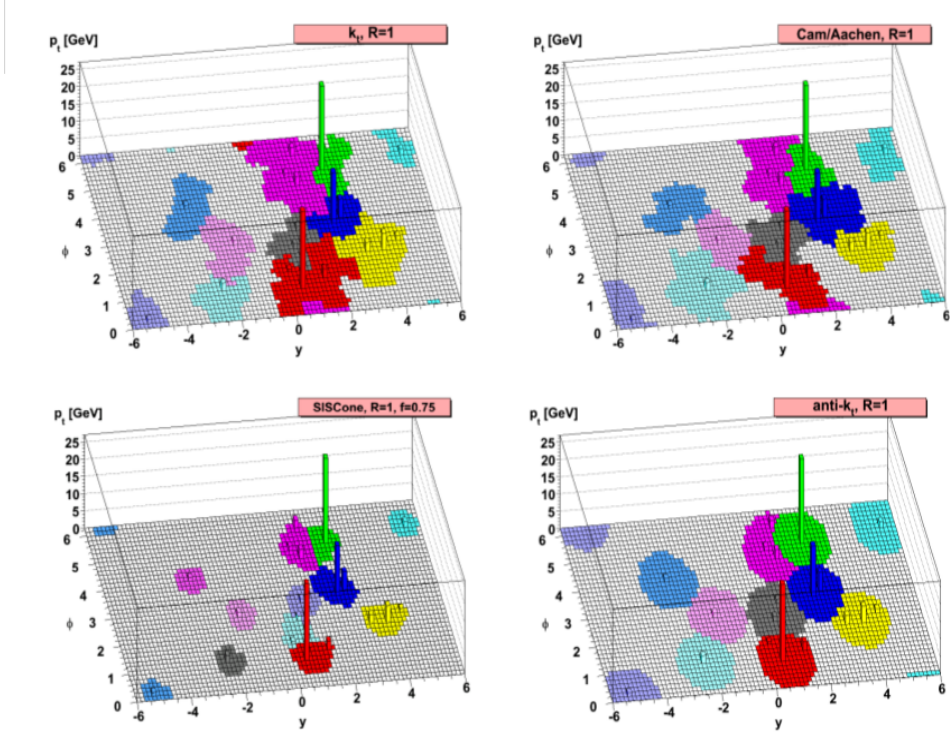


Figure 4.5: The behaviors of different jet algorithms in parton level [143].

calorimeters. In addition, electronic noise and event pile-up too add to the discrepancy in energy measurement. The motive of jet energy correction (JEC) is to relate, on an average, the jet energy measurement in the detector to the energy of the corresponding particle jet. For jet energy correction, a multi-level factorized approach is undertaken, where each correction has a unique effect and is applied in a fixed order [147]. These corrections are derived both from data-driven and MC-truth methods for *in-situ* calibration. The correction factors listed below are applied to the jets in a sequential manner.

- **L1 Offset** : It is required to remove energy contribution coming from pile-up and underlying events [148]. The median jet  $p_T$  is used to compute the energy density arising from these effects for each event, which is then multiplied by the jet area before subtracting it from the jet  $p_T$ .
- **L2 Relative ( $\eta$ )** : It is a relative correction applied to the pile-up subtracted jet energy, to make the jet response flat as a function of pseudorapidity.
- **L3 Absolute ( $p_T$ )** : Once the jet energy has been corrected for  $\eta$  dependence, another

correction is applied to make the jet response flat in  $p_T$  also.

- L2L3 Residual : Finally, after all above corrections, a factor is applied only to data events to deal with small, residual difference between the data and MC, based on the *in-situ* measurements of the relative and absolute jet energy scales.

#### 4.4.4 Jet Identification

Once the jet has been reconstructed and all the corrections applied, it is now important to identify good reconstructed jets and to discriminate them from the fake jets due to electronic noise or other detector artifacts. For this job, a set of variables has been defined [149], which are listed below:

- Charged hadron fraction – fraction of energy deposited by the charged hadrons in the HCAL.
- Neutral hadron fraction – fraction of energy deposited by the neutral hadrons in the HCAL.
- Charged electromagnetic fraction – fraction of energy deposited in the ECAL by the charged constituents of the jet.
- Neutral electromagnetic fraction – fraction of energy deposited in the ECAL by the neutral constituents of the jet.
- Number of constituents or number of particles in the jet.
- Charged multiplicity – number of charged particles (charged constituents) in the jet.



# Chapter 5

## Search for excited quarks in $\gamma + \text{jet}$ final state

This chapter describes in detail the steps used in the eponymous analysis using  $19.7 \text{ fb}^{-1}$  of proton-proton collision data collected by the CMS experiment at  $\sqrt{s} = 8 \text{ TeV}$ .

To test the excited quark model [71, 72, 150] against the SM, the cross section in terms of the number of events as a function of  $\gamma + \text{jet}$  mass must be estimated. To compute this information, the data and simulated MC samples stored in AOD format need to be processed. As explained in Section 2.4, AOD is a small subset of the full event information containing kinematic variables, identification and isolation information of all the physics objects: photons, jets, muons, electrons, vertices, etc. As millions of events need to be analyzed and processed to select the events of interest, local computing resources via interacting methods is not feasible. Hence, a technique known as grid computing [151], is employed to process the data and simulated MC events using CMS Remote Analysis Builder (CRAB) [152], the official CMS analysis software that avoids the complexity of submitting, checking and retrieving analysis jobs. For this analysis, Fermilab Tier-3, T3-US.FNALLPC is used as the storage element and for processing the generic AOD samples into analysis specific ‘Ntuples’. The histograms of all the necessary observables are prepared by processing these Ntuples.

## 5.1 Signal : Excited quarks

In this analysis, we search for excited quarks ( $q^*$ ) decaying to a high  $p_T$  photon and a hard jet. The possible physics processes that can contribute to the above final state in a pp collider are mentioned in Section 1.2.1, with corresponding Feynman diagrams shown in Fig 1.2. Among all the allowed processes, only  $qg \rightarrow q\gamma$  channel is used for this study and receives both s- and t-channel contribution as depicted in Fig 5.1. The production of  $q^*$  via s-channel quark gluon scattering would give a resonance in the invariant mass spectrum of  $\gamma + \text{jet}$  and is expected to give a bump over the SM predictions in the  $\gamma + \text{jet}$  invariant mass distribution. The t-channel is expected to give an excess of events with respect to the SM predictions and would add to the effect of s-channel contribution<sup>1</sup>.

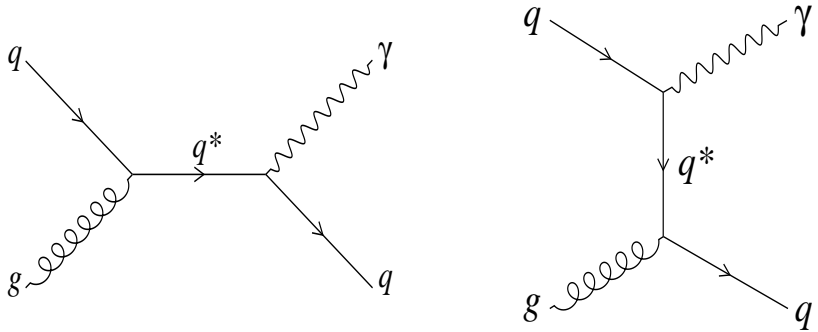
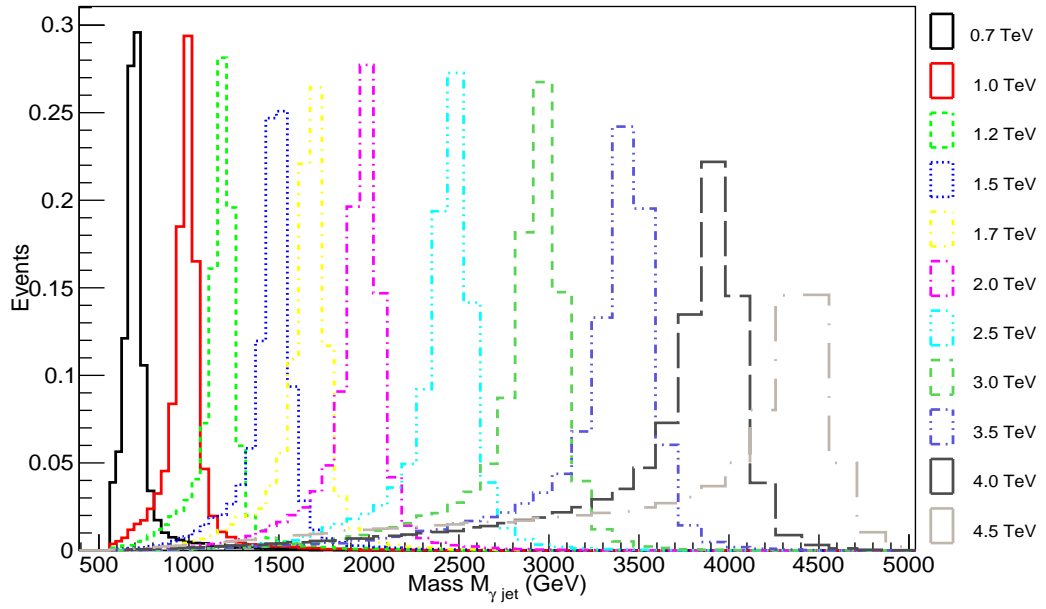


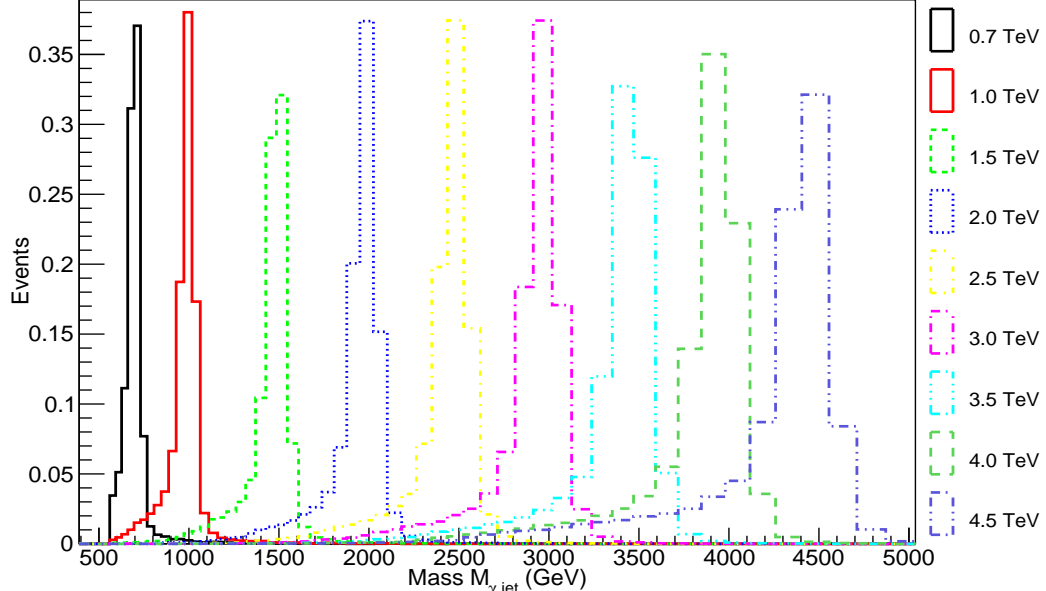
Figure 5.1: Feynman diagrams for  $qg \rightarrow q^* \rightarrow q\gamma$  final state via (left) s- and (right) t-channel processes.

A wide range of  $q^*$  masses ( $M_{q^*}$ ) and a couple of coupling strength ( $f$ ) scenarios have been considered in the analysis. As mentioned earlier in Section 1.2.1, this analysis made use of the assumption that the compositeness scale  $\Lambda$  is same as the  $M_{q^*}$  and all the coupling multipliers,  $f_s$ ,  $f$ ,  $f'$  are same, denoted by  $f$ . For  $f = 1.0$ ,  $M_{q^*} = 0.7, 1.0, 1.2, 1.5, 1.7, 2.0, 2.5, 3.0, 3.5, 4.0$ , and  $4.5 \text{ TeV}$  and for  $f = 0.5$ ,  $M_{q^*} = 0.7, 1.0, 1.5, 2.0, 2.5, 3.0, 3.5, 4.0$ , and  $4.5 \text{ TeV}$  are explored. The above set of choice is not unique and is chosen to scan the maximum number of mass points within the limitations of computing infrastructure. A complete list of PYTHIA generated signal samples with respective cross sections is given

<sup>1</sup>Note that this division into the two channels is a not a gauge invariant one and hence lacks physical meaning. However, it serves to highlight the feature of the distribution.



(a) Coupling strength,  $f = 1.0$



(b) Coupling strength,  $f = 0.5$

Figure 5.2: Invariant mass plot normalized to unity for all the  $q^*$  mass points.

in Table 3.1. They are generated with Z2\* [127, 128] event tune and CTEQ6L1 [117, 118] PDFs. The invariant mass distribution for all the generated and simulated  $q^*$  mass points, normalized to unity is shown in Fig 5.2.

## 5.2 Sources of background

The  $\gamma +$  jet final state is a clean and topologically simple signature in the detector. It can, however, be mimicked by many known SM processes and forms the source of background in our study of  $q^* \rightarrow \gamma +$  jet. The potential physics backgrounds are listed below according to the their dominance :

**SM  $\gamma +$  jet :** The most dominant contribution to  $\gamma +$  jet final state comes when a photon and a hadronic jet is produced in a hard scattering. This forms the irreducible background for the search  $q^*$  in the  $\gamma +$  jet decay channel. It can be achieved by the quark gluon Compton scattering ( $qg \rightarrow \gamma q$ ) shown in Fig 5.3a, quark antiquark annihilation ( $q\bar{q} \rightarrow \gamma q$ ) shown in Fig 5.3b and gluon gluon fusion ( $gg \rightarrow \gamma q$ ) shown in Fig 5.3c. The  $qg$  scattering dominates the total  $\gamma +$  jet cross section in pp collision for almost the entire range of  $p_T^\gamma$ . Though the  $q\bar{q}$  contribution is sub-leading when compared to  $qg$ , its fraction increases at higher  $p_T^\gamma$ . The  $gg$  fusion constitutes a minuscule fraction of the total  $\gamma +$  jet cross section. These backgrounds are modeled using PYTHIA with contiguous intervals of  $p_T^\gamma$  spanning from 120 GeV to a very large value. For example the  $p_T^\gamma$  range varies as: 120-170, 170-300, 300-470, 470-800, 800-1400, 1400-1800,  $>1800$  GeV and are listed in Table 3.2.

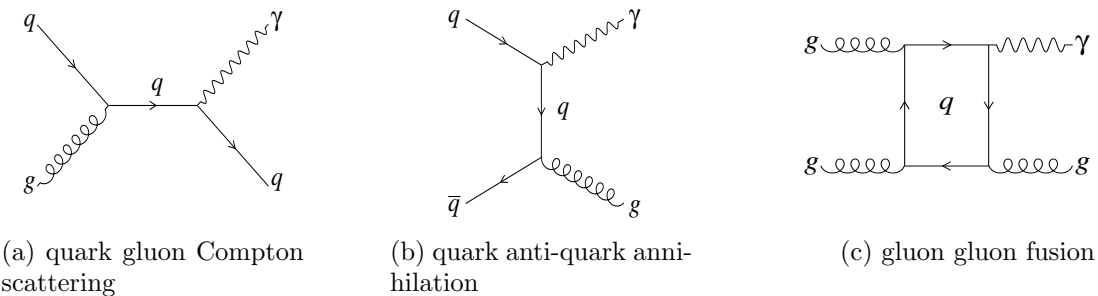


Figure 5.3: Some of the Feynman diagrams of SM  $\gamma +$  jet final states with different possible allowed exchanges.

**SM QCD dijet :** The next leading contribution to the total background comes from the dijet events, when one of the jets fragments into a high  $E_T \pi^0$  which subsequently decays into a pair of overlapping photons and hence, is reconstructed as a single photon.

In addition, the electromagnetic fraction of a jet can also mimic a photon in the detector. This background constitutes processes like  $qg \rightarrow qg$ ,  $q\bar{q} \rightarrow q\bar{q}$ ,  $gg \rightarrow gg$  and  $gg \rightarrow q\bar{q}$  with all the allowed exchanges, and Feynman diagrams for a few of these channels are shown in Fig 5.4. The total production cross-section for such processes is about  $10^4$  larger than the  $\gamma + \text{jet}$  process. Despite having a large cross section, its contribution to the total background is of the same order as that of the  $\gamma + \text{jet}$  background as only a small fraction ( $10^{-3} - 10^{-4}$ ) of jets fake as a photon in the detector. Also, the dijet cross section falls very swiftly ( $\sim p_T^{-4}$ ) with increasing  $p_T^{\text{jet}}$  which provides an addition means to suppress this background for the study of large  $p_T$  photons and jets.

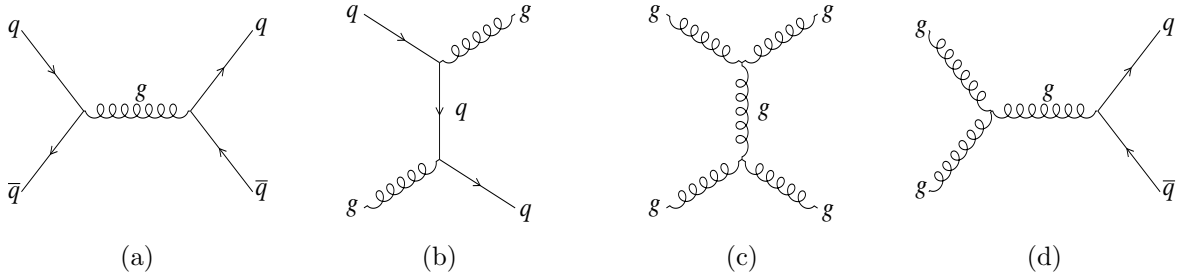


Figure 5.4: Some of the Feynman diagrams for SM QCD Dijet background.

The SM dijet background is also supplemented by something known as “bremsstrahlung contributions”, when a photon is radiated from one of the quark in the process of collinear fragmentation as shown in Fig 5.5. Similar contribution also arises from initial state radiation, when photon is radiated from one of the incoming quark line. This forms the photon + dijet final state, and mimics as  $\gamma + \text{jet}$  when one of the jets is either lost or mismeasured. As these photon do not emerge from the interaction vertex and have collinear quark which manifests as jets, these are easily removed by applying isolation requirements. The total SM dijet background is also modeled using PYTHIA with contiguous binning in  $p_T$ : 120-170, 170-300, 300-470, 470-600, 600-800, 800-1000, 1000-1400, 1400-1800,  $>1800$  GeV and are listed in Table 3.2.

**SM EWK processes :** Finally, a very small fraction of the total background comes from electroweak processes, viz.,  $W/Z + \gamma$  production as shown in Fig 5.6 with the heavy

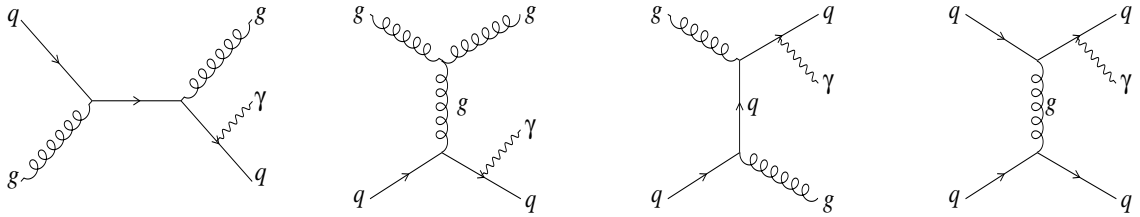


Figure 5.5: Feynman diagrams for Bremsstrahlung contribution of SM QCD dijet production.

bosons decaying into a pair of jets. For highly boosted bosons, two jets merge to give a photon and a jet in the final state. The other scenario is when one of the jets from heavy boson is lost in the detector. These backgrounds are generated using the **MADGRAPH** event generator and are also listed in Table 3.2.

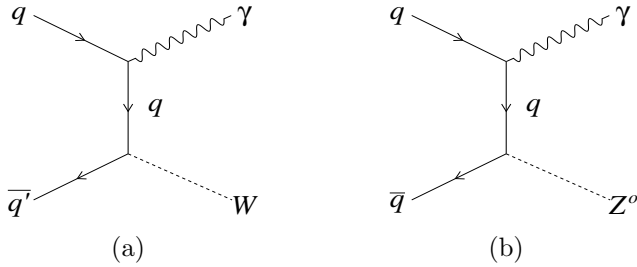


Figure 5.6: Background contributions to  $\gamma + \text{jet}$  from electroweak processes.

All the signal and background simulated MC samples mentioned above are processed within the CMSSW version 5\_3\_8\_patch1 package [87, 153] using  $Z2^*$  underlying event tune [127, 128], CTEQ6L1 PDFs [117, 118] and full CMS detector simulation with **GEANT4** toolkit as mentioned in Chapter 3.

## 5.3 Data Samples and Triggers

### 5.3.1 Data

The data samples considered for this analysis are listed in Table 3.3. During the entire data taking period for  $\text{pp}$  collisions at  $\sqrt{s} = 8 \text{ TeV}$ , i.e. year 2012, the instantaneous luminosity, known with a precision of 2.6%, varied over the range  $10^{29} - 10^{33} \text{ cm}^{-2}\text{s}^{-1}$  and resulted in

a total integrated luminosity of  $19.7\text{fb}^{-1}$ . The events stored in these data samples are part of runs and lumi sections<sup>2</sup> for which all CMS sub-detectors were properly collecting data. These runs and lumi sections are tabulated in a specific java format JSON file, also listed in Table 3.3. In addition, while processing these datasets and making Ntuples for analysis, the following set of filters were applied to the data to remove various noisy events as reported during offline data quality monitoring,

- CSC tight beam halo filter: To reject beam halo muons.
- HBHE noise filter with isolated noise rejection: To reject noisy HCAL events.
- HCAL laser filter: For removing events containing HCAL calibration laser firing during the collision bunch-crossing.
- ECAL dead cell trigger primitive filter: To reject events where masked crystals produce large missing energy.
- Bad EE supercrystal filter: For removing events from two EE crystals registering anomalously high energies.

### 5.3.2 Trigger

The CMS trigger system as described in Section 2.3 is designed to control event rates consistent with the available bandwidth and is modified with the luminosity of the machine. During 2012, the LHC improved the luminosity by a large amount over the year and consequently the trigger conditions were modified to suit the increase in instantaneous luminosity within the allowed bandwidth. As mentioned in Section 2.3, CMS trigger consists of two parts, the L1 trigger which operates at the hardware level and the HLT which is a software based trigger.

In the L1 trigger system, electromagnetic energy deposits are reconstructed through the sum of the transverse energy ( $E_T$ ) deposited in two neighboring groups of  $5 \times 5$  ECAL

---

<sup>2</sup>One lumi section refers to  $2^{20}$  orbits or about 93s.

crystals (trigger towers). The  $E_T$  sum of two neighboring trigger towers is required to be above a pre-defined threshold of 8 GeV. The events satisfying the L1 selection conditions are passed on to the HLT, where the same clustering algorithm as used in the off-line photon reconstruction and specified in Section 4.3 is used to cluster the crystals. To suppress the influence of anomalous interactions arising from direct ionization of APDs in the ECAL, a simple topological selection criterion is implemented at the HLT level, where the highest energy deposit in a single crystal,  $E_1$ , is compared to the total energy deposited in the four adjacent crystals,  $E_4$ , for each channel and if  $1 - E_4/E_1 > 0.95$ , such anomalous signals are rejected. The L1 trigger used in the analysis is L1\_SingleEG30 [83, 108, 109],

Trigger	Integrated Luminosity
HLT_Photon150_v1	94.67 $\text{pb}^{-1}$
HLT_Photon150_v2	390.11 $\text{pb}^{-1}$
HLT_Photon150_v3	4.80 $\text{fb}^{-1}$
HLT_Photon150_v4	14.43 $\text{fb}^{-1}$
<b>Total of HLT_Photon150</b>	<b>19.71 <math>\text{fb}^{-1}</math></b>

Table 5.1: List of HLT paths used in the analysis.

i.e. events with at least one  $e/\gamma$  candidate with  $E_T > 30 \text{ GeV}$  are passed on to the HLT. At this level, no distinction is made between a photon or an electron and no isolation or identification criteria are applied. The analysis makes use of single photon trigger, HLT\_Photon150 [83, 108, 109], i.e. events having a minimum of one reconstructed cluster in the ECAL with  $E_T$  above 150 GeV are selected. The HLT\_Photon150 trigger path was required to be unprescaled for the entire data taking period which means all the events passed by L1 and HLT are stored for analysis. The effective integrated luminosities for different HLT paths are summarized in Table 5.1.

The offline trigger efficiency, also referred as trigger turn-on was studied as a function of leading photon  $p_T$  to correct for possible inefficiencies in different phase space. The trigger turn-on was evaluated using Eq 5.1 with respect to lower threshold triggers, HLT\_Photon75\_CaloIdVL\_v\* and HLT\_Photon90\_CaloIdVL\_v\* [83, 108, 109]. These lower

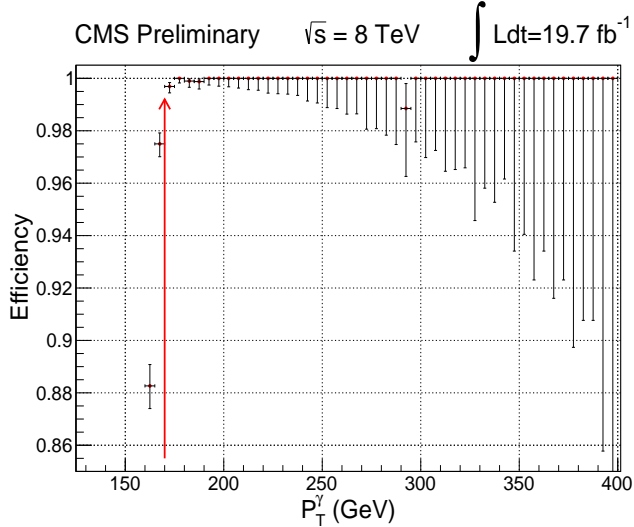


Figure 5.7: Trigger turn-on curve for single photon trigger HLT\_Photon\_150. The errors on each point are statistical only.

threshold triggers have very loose identification criteria applied based on the calorimetric

$$\text{Trigger Turn-on} = \frac{\text{HLT\_Photon150\_v* AND Prescale} = 1}{\text{HLT\_Photon75\_CaloIdVL\_v* OR HLT\_Photon90\_CaloIdVL\_v*}} \quad (5.1)$$

information and are prescaled by some factor. The trigger turn-on curve as shown in Fig 5.7 saturates and reaches the plateau region with efficiency of almost 100% at 170 GeV.

## 5.4 Reweighting of MC samples for pile-up

In high-luminosity collisions, there is a finite probability that a single bunch crossing results in many separate inelastic interactions. These additional interactions are referred to as pile-up (PU) interactions, and are proportional to the instantaneous luminosity of the collision. The presence of PU affects the reconstruction efficiency and may be reflected in the  $p_T$  distribution of the reconstructed objects. It is expected to affect the current analysis in the following two ways:

- Additional energy deposits from PU would be added to the jets from the main interaction, and

- Tracks and calorimetric towers from PU energy deposits will be added to the isolation energy sum of photon, thus making isolation cuts less efficient.

In this analysis, PF clustering algorithms, as described in Section 4.4.1, which make use of particles reconstructed using PF algorithms, are deployed to take care of these additional interactions. Charged particles with tracks pointing to non-primary vertices are removed from the list of particles used to reconstruct jets. Neutral particles do not leave tracks, and therefore cannot be associated with a vertex and are removed. Various techniques have been developed and centrally validated in CMS to alleviate the degradation in object reconstruction due to PU effects. The present analysis makes full use of these improvements. The L1-offset, L2-absolute and L3-relative corrections, as mentioned in Section 4.4.3, are applied to remove the additional energy released in the event from PU interactions.

All simulated samples were generated with additional interaction (PU) to match the expected conditions of each data taking period using the 2012\_Summer\_50ns\_PoissonOOTPU pileup scenario [154]. The deterministic annealing primary vertex (PV) reconstruction is well-behaved for high levels of PU. However, the final distribution for the number of reconstructed PV is still sensitive to the details of the PV reconstruction and to differences in the underlying event in data and simulation. The number of reconstructed vertices can be further affected by the trigger and the event selection criteria. In order to factorize these effects, instead of reweighting the simulated MC events by the number of reconstructed PV, the simulation is reweighted using the number of pileup interactions, which is a Poisson distribution with a mean given by true number of interactions. The true number of interactions is the mean of number of interactions in a given lumi section using the measured instantaneous luminosity.

In the process of reweighting, the target pileup distribution for data is generated using the instantaneous luminosity per bunch crossing of 50 ns for each luminosity section, and the total pp inelastic cross section of 69.4 mb [154]. A Poissonian smearing is applied to

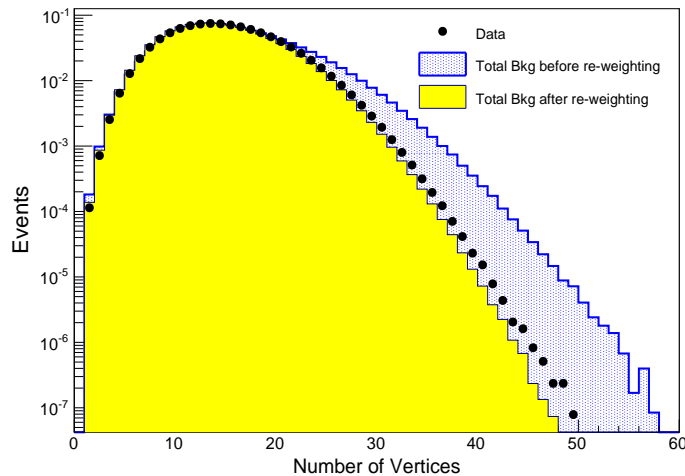


Figure 5.8: Effect of pileup re-weighting on MC.

model statistical fluctuations in the actual number of pileup events present in the data. A comparison of the number of vertices in an event for data and simulated MC events is shown in Fig 5.8, before and after reweighting for additional interactions.

All simulated MC events are thus re-weighted to reflect the data luminosity and are also corrected to pileup effects. The relevant event weight is given by :

$$w_i = \frac{PUweight \times \sigma_i \times Lumi}{N_{tot}} \quad (5.2)$$

where, *PUweight* is a factor from pile-up reweighting calculated per event,  $N_{tot}$  is the total number of simulated events and  $\sigma_i$  refers to the theoretical cross section of the simulated process.

## 5.5 Event Selection

In our signal topology, we expect excited quarks to decay into quarks (that fragment into jets) and photons. The events passing the trigger selection are required to have at least one well-identified vertex within 24 cms of the nominal interaction point in  $z$ -direction and within a radius 2 cm in the  $xy$ -plane. The vertex corresponding to the origin of the hard-scattering process with the largest value of  $\sum p_T^2$  of all associated tracks is identified

as the primary vertex. After selecting a good primary vertex, we search for an isolated photon. Photons, as explained in Section 4.3, are objects reconstructed based on clusters of energy deposited in the ECAL, and are identified and isolated using the following set of criteria that were defined in Section 4.3.2:

- $\sigma_{i\eta i\eta} < 0.011$ ,
- **Single tower H/E**  $< 0.05$ ,
- **PF photon isolation**  $< 0.5 + 0.005 \times p_T^\gamma \text{ GeV}$ ,
- **PF charged hadron isolation**  $0.7 \text{ GeV}$ ,
- **PF neutral hadron isolation**  $< 0.4 + 0.04 \times p_T^\gamma \text{ GeV}$ ,
- **Conversion safe electron veto:** True.

The photon isolation cone is susceptible to pileup from interactions not corresponding to the primary vertex. These variables need to be corrected for the presence of additional reconstructed vertices and this was done using the following equation:

$$\text{Iso}^{new} = \text{Iso}^{original} - (\rho_{event} \times A_{eff}) \quad (5.3)$$

where Iso refers to all the three PF isolations (photon, charged and neutral hadrons). The

Binning in $\eta$	EA charged hadrons	EA neutral hadrons	EA photons
$ \eta  < 1.0$	0.012	0.030	0.148
$1.0 <  \eta  < 1.479$	0.010	0.057	0.130
$1.479 <  \eta  < 2.0$	0.014	0.039	0.112
$2.0 <  \eta  < 2.2$	0.012	0.015	0.216
$2.2 <  \eta  < 2.3$	0.016	0.024	0.262
$2.3 <  \eta  < 2.4$	0.020	0.039	0.260
$ \eta  > 2.4$	0.012	0.072	0.266

Table 5.2: Effective Area for photon isolation criteria.

energy density  $\rho_{event}$ , computed using the FastJet package [155], is the median background

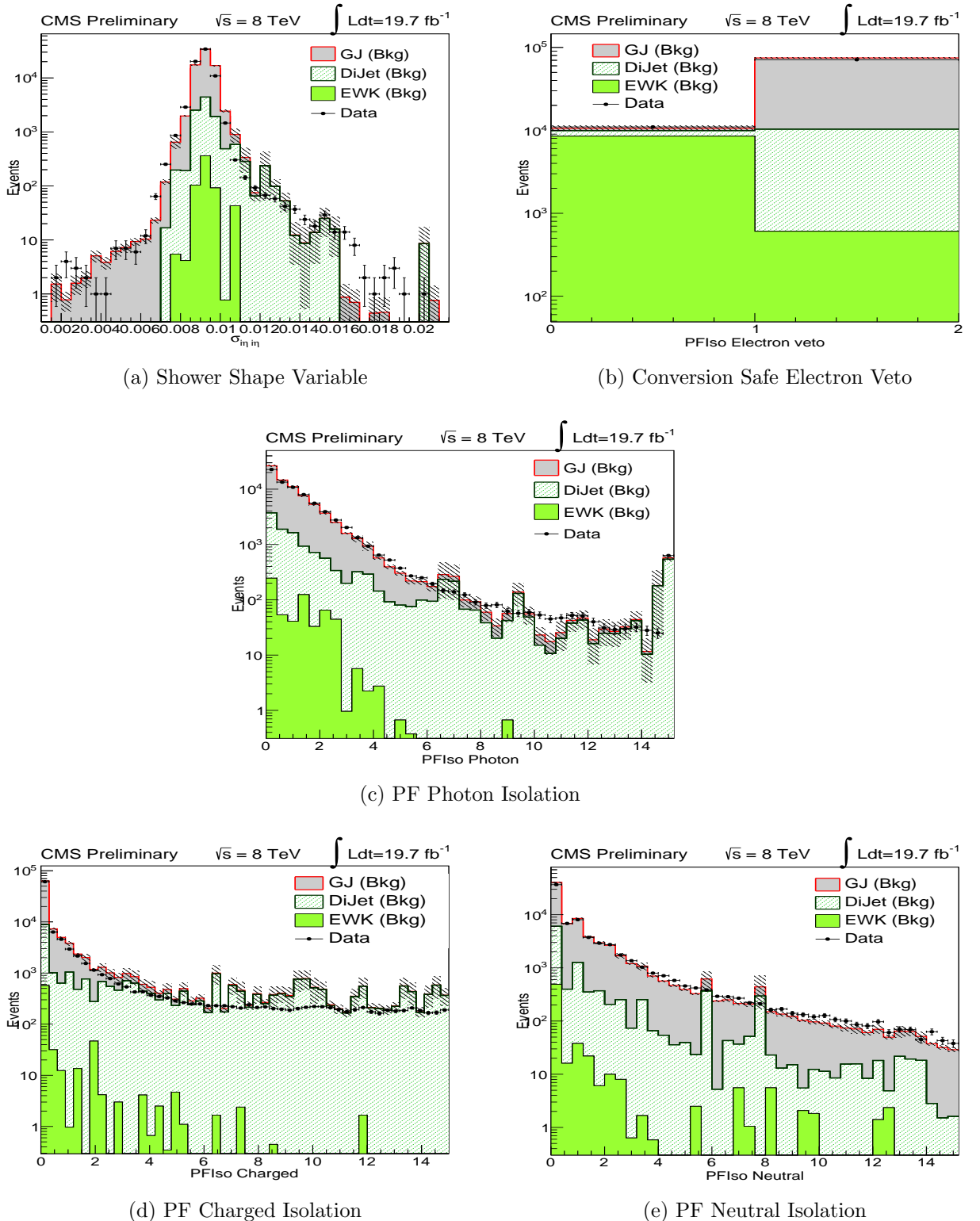


Figure 5.9: N-1 plots for photon identification and isolation variables.

density per unit area of the particles associated with pile-up vertices and gives a measure of the pileup activity in the event. The effective area,  $A_{eff}$ , is defined as the ratio of the

slope obtained from linearly fitting  $\text{Iso}(N_{vtx})$  to the one from linearly fitting  $\rho_{event}(N_{vtx})$ . The values of  $A_{eff}$  are tabulated for all three isolation criteria, separately for barrel and endcap in Table 5.2. N-1 distributions, i.e. applying cuts on all the variables except the one under study, of photon identification and isolation variables in Data and MC are shown in Fig 5.9 while the comparison after applying the final selection criteria has been shown in Fig 5.10.

Since the non-collision backgrounds from anomalous calorimeter signals described in Section 4.3.2.3 may contribute to the background for this physics process, the following restrictions are applied on the rectangular ratios (described in Section 4.3.2.1), shower shape profile and the timing of the photon candidates :

- $R9 < 1$
- $\sigma_{i\eta i\eta} > 0.001$
- $\sigma_{i\phi i\phi} > 0.001$
- The largest intracluster time difference (LICTD) between crystals with more than 1 GeV deposited must have an absolute value less than 5 ns.

A collection of isolated and identified photons ordered in  $p_T$  is formed after applying the above set of criteria. The highest  $p_T$  (leading) photon in the event is required to have  $p_T$  greater than 170 GeV. The selection on  $p_T$  comes from the fact that trigger is 100% efficient at this value. The leading photon is also required to be within the barrel fiducial region of the detector ( $|\eta| < 1.4442$ ) as  $q^*$ , if produced, would result in back-to-back production of  $\gamma$  and jet and are expected mostly to be in the barrel section of the detector. The thus selected photon is referred to as the photon candidate for the analysis.

Events are also required to have at least one jet (reconstructed with anti- $k_T$  algorithm with distance parameter 0.5 as described in Section 4.4) which is away from the leading photon in  $\Delta R = 0.5$ . In addition to the PF calorimeter-noise cleaning at reconstruction level, to discriminate jets from fake jets due to electronic noise or other detector artifacts,

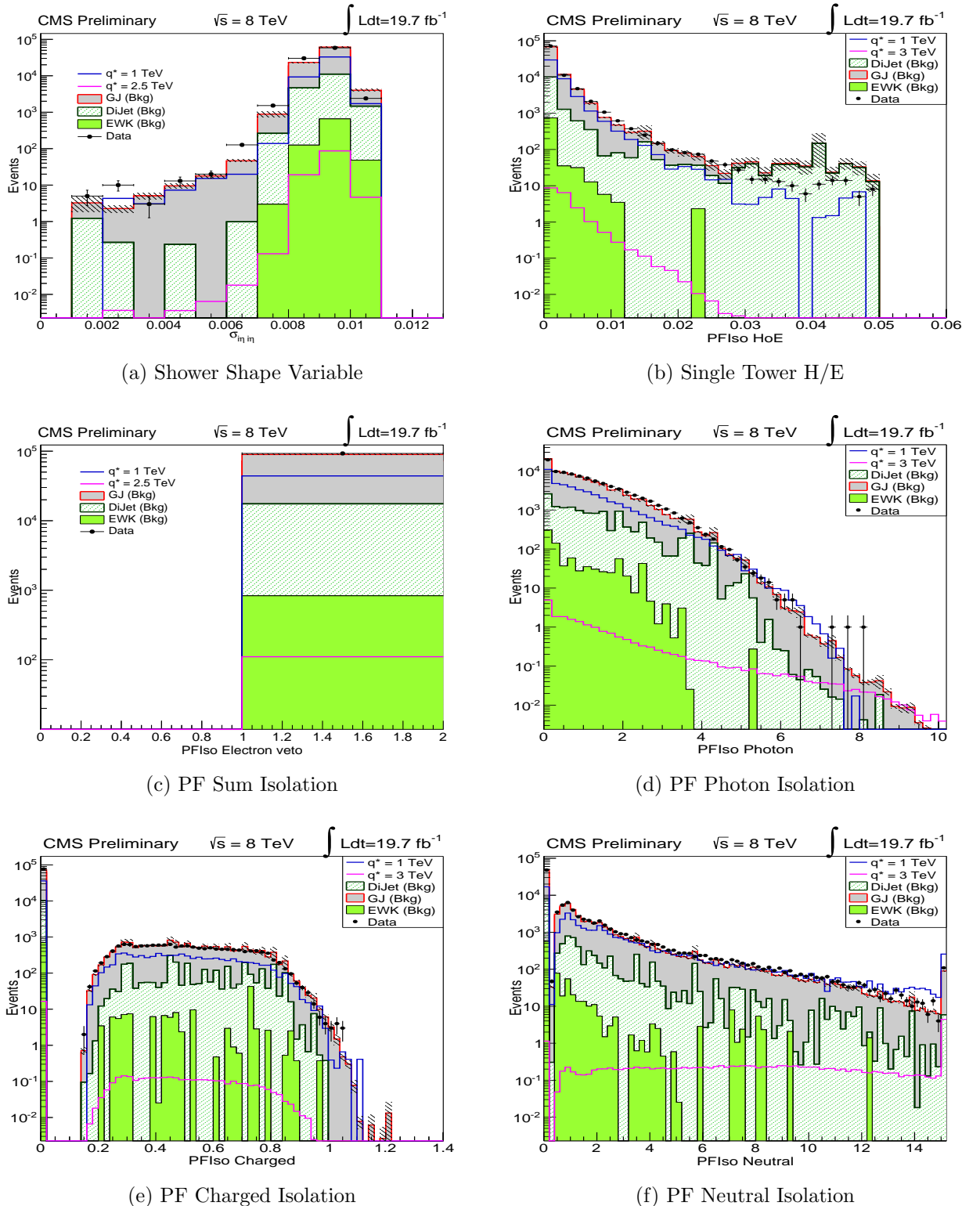


Figure 5.10: Distributions of photon identification and isolation variables after all the selection criteria.

a set of variables are defined in Section 4.4.4. The selection applied to these variables is listed below :

- Neutral Hadron Fraction  $< 0.90$ ,
- Charged Hadron Fraction  $> 0$ ,
- Neutral Electromagnetic Fraction  $< 0.90$ ,
- Charged Electromagnetic Fraction  $< 0.90$ ,
- Number of Constituents  $> 1$

The jet candidate thus selected is required to be within  $|\eta| < 3.0$  in the pseudorapidity region, and need to have a  $p_T$  greater than 170 GeV. A symmetric selection on the  $p_T$  of  $\gamma$  and jet is applied looking at the 2-dimensional distribution of  $p_T$  of  $\gamma$  and jet as shown in Fig 5.11. To improve non-linear response of the calorimeter, a set of jet energy corrections, called L1, L2, and L3 corrections are applied to both the data and MC simulations as described in Section 4.4.3. The comparison of jet identification variable in Data and MC after final selection criteria is shown Fig 5.12.

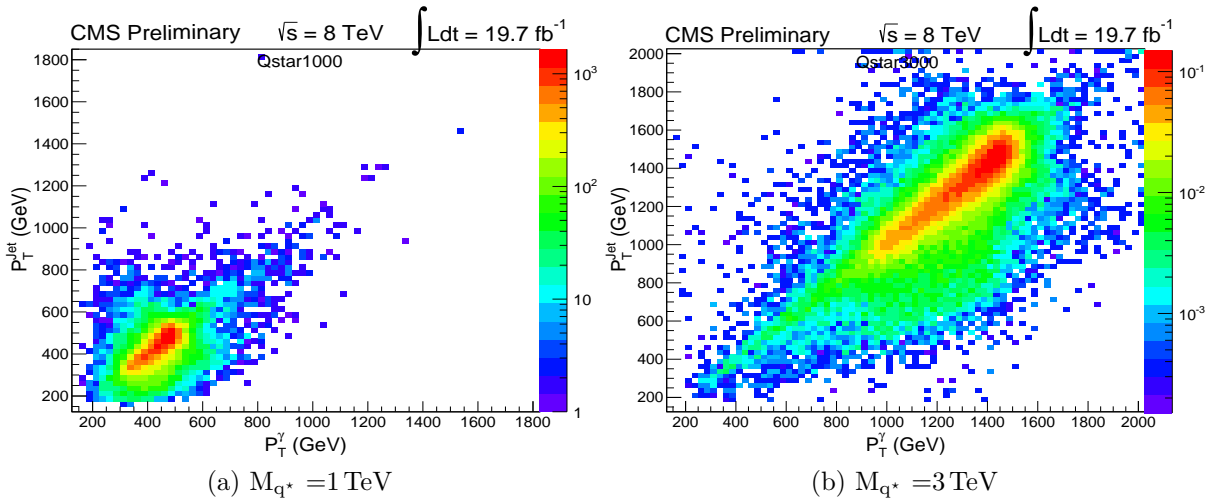


Figure 5.11: 2-dimensional histogram comparing  $p_T$  of  $\gamma$  and jet for  $q^*$  signal.

If more than one photon or jet candidate exist in the event, the leading objects are chosen for further analysis. The invariant mass of the  $\gamma + \text{jet}$  system is evaluated using

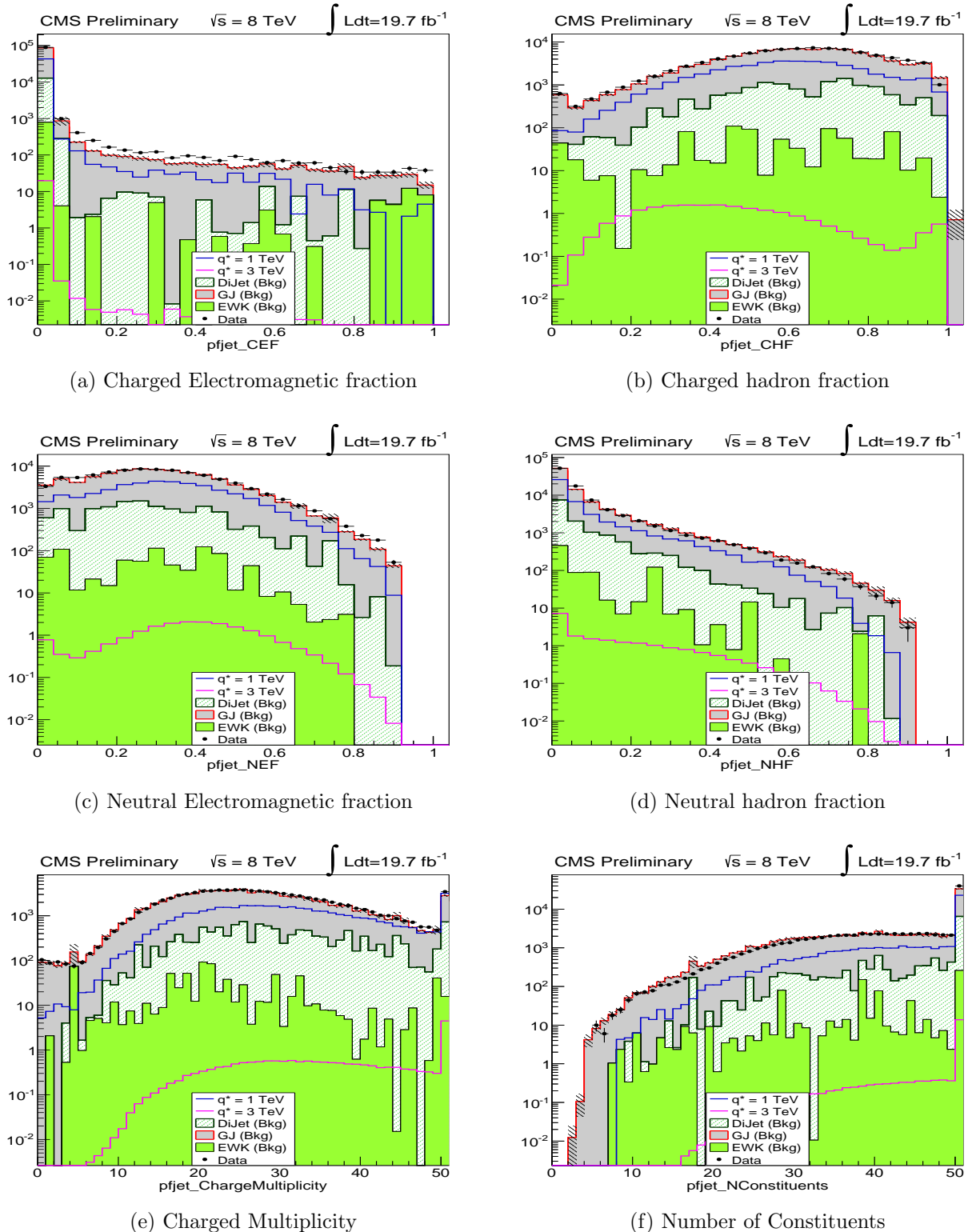


Figure 5.12: Comparison of Data and MC for jet identification variables after final selection criteria has been applied.

the leading photon and jet candidates and is given by  $M_{\gamma,\text{jet}} = \sqrt{(E^\gamma + E^{\text{jet}})^2 - (\vec{p}^\gamma + \vec{p}^{\text{jet}})^2}$ . Selected photon and jet candidates are expected to be back-to-back in a two body final state, which is ensured by requiring  $|\Delta\phi(\gamma, \text{jet})| > 1.5$ . The decay products arising out of excited quarks produced via s-channel process would lead to an isotropic distribution of the final-state objects, while all the backgrounds are predominantly produced through t-channel processes and have an angular distribution that is heavily peaked in the forward or backward direction. Hence, to reduce these background contributions while retaining high acceptance for signal, a selection of  $|\Delta\eta| < 2.0$  between the leading photon and jet is also applied. Finally a selection on the invariant mass of  $\gamma + \text{jet}$ , i.e.  $M_{\gamma,\text{jet}} > 560 \text{ GeV}$ , is applied to avoid the kinematical turn-on region in the  $\gamma + \text{jet}$  mass spectrum due to various selection requirements. The same selection criteria are applied to both data and simulations.

Since the theoretical predictions for  $\gamma + \text{jet}$  and dijet were generated with PYTHIA, a LO event generator, a K-factor of 1.3 [156–158] was applied to include NLO effects for both the simulated background MC samples. Also a data/MC scale factor of  $0.964 \pm 0.023$  and  $0.98 \pm 0.002 \pm 0.023$  was applied to simulated MC to take into account the inefficiency due to LICTD cut and Photon ID, respectively. The selection cut flow table after applying entire selection criteria and scale factors, for all the backgrounds and data, is shown in Table 5.3 along with  $q^*$  signal of  $M_{q^*} = 1 \text{ TeV}$ , while the signal efficiencies for various  $q^*$  mass points is listed in Table 5.4 & Table 5.5 respectively, for couplings  $f = 1.0$  and  $f = 0.5$ . It is observed from Table 5.3, that  $\gamma + \text{jet}$  SM production accounts for 80.5% of the total background, QCD dijets results in 18.5% of the background, while electroweak backgrounds contributes only 1.0%.

Figure 5.13 depicts the kinematical distributions for the leading photon and jet candidates selected after final selection criteria. The  $p_T$  distributions for leading photon and jet candidates, shown in Fig 5.13a and 5.13b, respectively, fall steeply with increase in  $p_T$  and were found to be in good agreement for data and MC simulations, after taking into account the various sources of systematic uncertainties, and the modelling of the  $p_T$

Cuts	Signal	DiJetg	PhotonJet	EWK	Total Bkg	Data
Total Events	81357	1.367e+07	776325	118070	1.45e+07	2.538e+07
HLT	81357	1.367e+07	776325	118070	1.45e+07	2.285e+07
Photon ID	57104	201546	586374	7751	795671	1.311e+06
$p_T^\gamma > 170 \text{ GeV}$	54639	95419	463731	4613	563763	626273
$ \eta^\gamma  < 1.4442$	52911	87505	435341	4356	527202	573933
Jet ID	52910	87505	435331	4352	527188	573913
$p_T^{\text{jet}} > 170 \text{ GeV}$	51721	60251	290647	2684	353582	355121
$ \eta^{\text{jet}}  < 3.0$	51615	59915	290446	2684	353045	354832
$ \Delta\phi  > 1.5$	51573	58347	290389	2667	351403	353731
$ \Delta\eta  < 2.0$	44429	48419	279206	2285	329910	327468
$M_{\gamma,\text{jet}} > 560 \text{ GeV}$	44073	16654	72142	832	89628	92786

Table 5.3: Selection cut flow table for  $q^*$  signal with  $M_{q^*} = 1 \text{ TeV}$ , data and different backgrounds showing number of expected events after each level.

Cuts	700	1000	1200	1500	1700	2000	2500	3000	3500	4000	4500
Initial Efficiency	100	100	100	100	100	100	100	100	100	100	100
Photon ID	67.6	70.2	70.9	71.7	71.9	72.1	72.1	71.9	72.1	70.9	68.7
$p_T^\gamma > 170 \text{ GeV}$	59.8	67.2	69.2	70.7	71.2	71.7	71.7	71.5	71.7	70.4	68.1
$ \eta^\gamma  < 1.4442$	56.9	65.0	67.3	68.9	69.3	69.8	69.8	69.6	69.6	68.2	65.9
Jet ID	56.9	65.0	67.3	68.9	69.3	69.8	69.8	69.6	69.6	68.2	65.9
$p_T^{\text{jet}} > 170 \text{ GeV}$	53.2	63.6	66.2	68.4	68.9	69.6	69.7	69.6	69.5	68.1	65.7
$ \eta^{\text{jet}}  < 3.0$	53.1	63.4	66.1	68.3	68.8	69.6	69.7	69.6	69.5	68.0	65.7
$ \Delta\phi  > 1.5$	53.1	63.4	66.1	68.3	68.8	69.5	69.6	69.5	69.5	68.0	65.7
$ \Delta\eta  < 2.0$	48.7	54.6	55.9	57.6	57.6	58.5	58.7	58.7	58.5	57.4	55.4
$M_{\gamma,\text{jet}} > 560 \text{ GeV}$	45.7	54.2	55.7	57.5	57.6	58.5	58.7	58.7	58.5	57.3	55.3

Table 5.4: Selection efficiencies (in %) for  $q^*$  signal samples with  $M_{q^*} = 700 - 4500 \text{ GeV}$ , and coupling  $f = 1.0$ .

distribution in PYTHIA. Similarly, the  $\eta$  distributions for both photon and jet, shown in Fig 5.13c and 5.13d, respectively, were also found to be in good agreement with the shape predicted by the simulations, and no regions with significant deviations were observed.

Other kinematical variables  $\Delta\eta$  and  $\Delta\phi$  between the leading photon and jet are shown in Fig 5.14. Figure 5.14a compares the  $\Delta\eta(\gamma, \text{jet})$  spectra in data and simulations, yielding good agreement. Figure 5.14b verifies that the events with back-to-back topology are selected most of the times with our selection criteria.

Finally, the invariant mass spectrum of  $\gamma + \text{jet}$  system (as shown in Fig 5.15) is studied to validate our selection criteria based on the MC simulations. This invariant mass dis-

Cuts	1000	1500	2000	2500	3000	3500	4000	4500
Initial Efficiency	100	100	100	100	100	100	100	100
Photon ID	70.5	71.5	72.4	72.3	72.3	72.1	70.8	66.5
$p_T^\gamma > 170 \text{ GeV}$	67.6	70.6	71.9	71.9	71.9	71.8	70.5	66.0
$ \eta^\gamma  < 1.4442$	65.4	68.8	70.1	70.0	69.9	69.7	68.3	63.6
JetID	65.4	68.8	70.1	70.0	69.9	69.7	68.3	63.6
$p_T^{\text{jet}} > 170 \text{ GeV}$	63.7	68.3	69.9	69.9	69.9	69.7	68.2	63.6
$ \eta^{\text{jet}}  < 3.0$	63.6	68.2	69.9	69.9	69.9	69.7	68.2	63.6
$ \Delta\phi  > 1.5$	63.6	68.2	69.8	69.9	69.8	69.6	68.2	63.5
$ \Delta\eta  < 2.0$	54.8	57.5	58.7	58.9	58.8	58.7	57.6	53.4
$M_{\gamma, \text{jet}} > 560 \text{ GeV}$	54.5	57.4	58.7	58.9	58.8	58.7	57.6	53.3

Table 5.5: Selection efficiencies (in %) for  $q^*$  signal samples with  $M_{q^*} = 1000 - 4500 \text{ GeV}$ , and coupling  $f = 0.5$ .

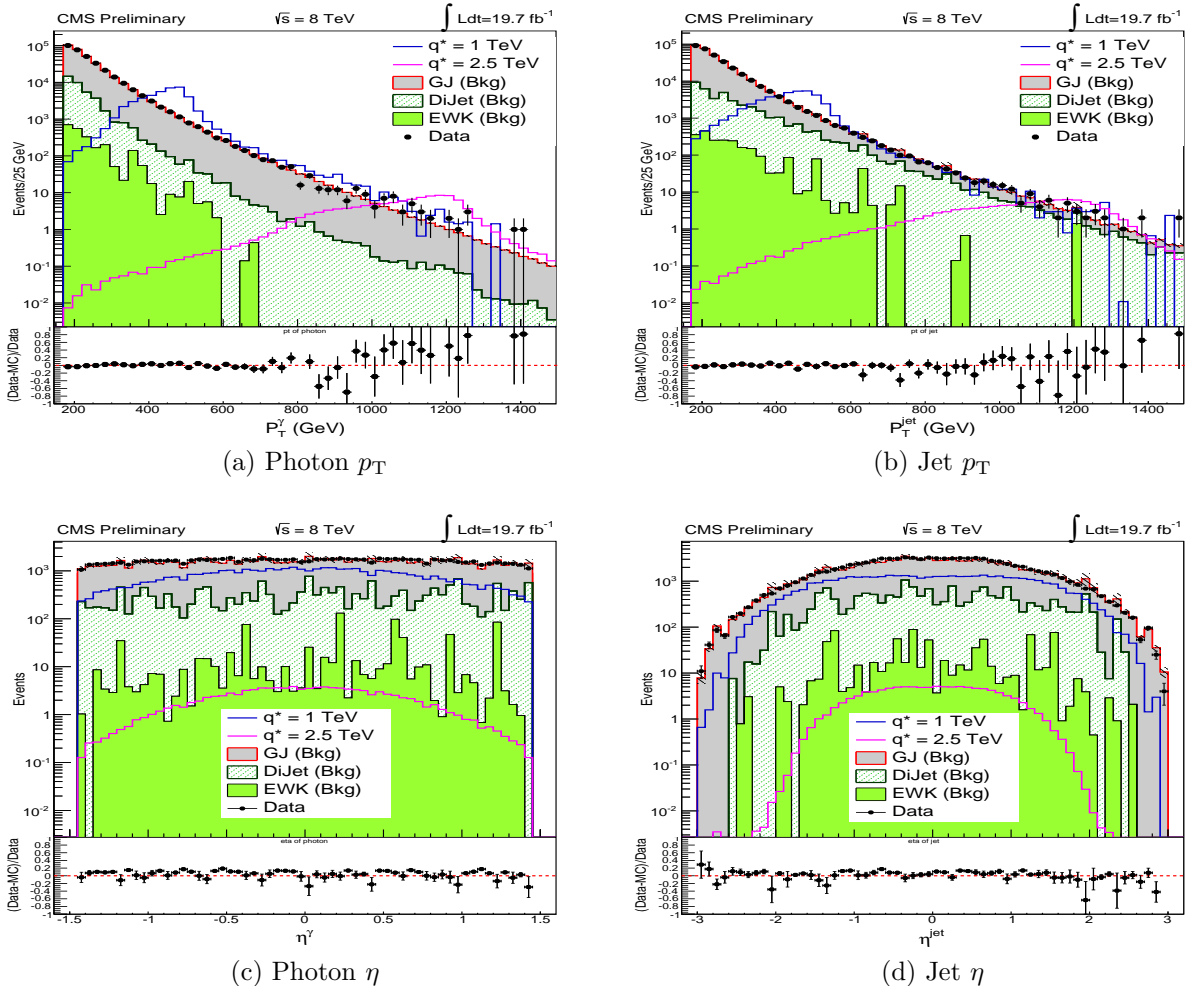


Figure 5.13: The  $p_T$  and  $\eta$  spectrum of the leading  $\gamma$  and jet for the events comparing data and MC simulation after applying the final selection criteria.

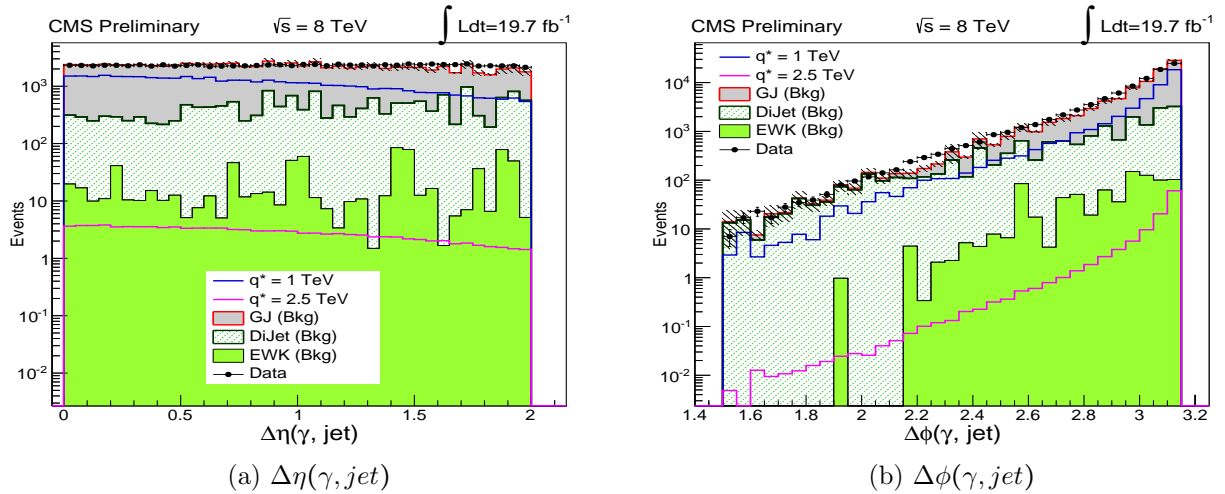


Figure 5.14: The  $\Delta\eta(\gamma, \text{jet})$  and  $\Delta\phi(\gamma, \text{jet})$  distributions between the leading  $\gamma$  and jet comparing data and MC simulation after applying final selection criteria.

tribution and all the above kinematical distributions confirm that the photons and jets in this data sample have the kinematics expected from the theoretical predictions. *I remind here that I do not use the MC simulations, but a data driven technique, to estimate the backgrounds in this analysis. A smooth fit function is used to model our SM background, as described in Section 5.6.1.*

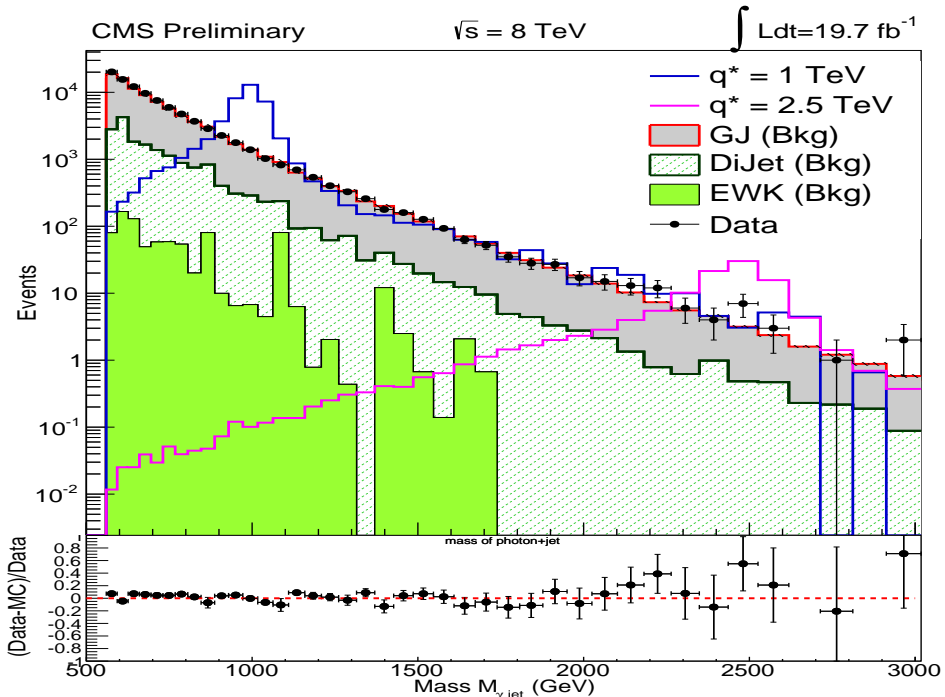


Figure 5.15: Invariant mass of  $\gamma + \text{jet}$ .

## 5.6 Photon + Jet Spectrum

The  $\gamma$ +jet invariant mass spectrum falls steeply with the increase in  $\gamma$ +jet mass. Variable binning, with bin width approximately equal to the width of the excited quarks was chosen, which increases as a function of mass.

To obtain the mass binning function, the core of the invariant mass distribution of  $q^*$  for all the resonant mass points is fit with Gaussian, Breit-Wigner and Crystal Ball functions as shown in Fig 5.16 and 5.17. Crystal Ball function, that describe the resonance peaks most accurately based on the  $\chi^2/ndf$  of the fit, is given by:

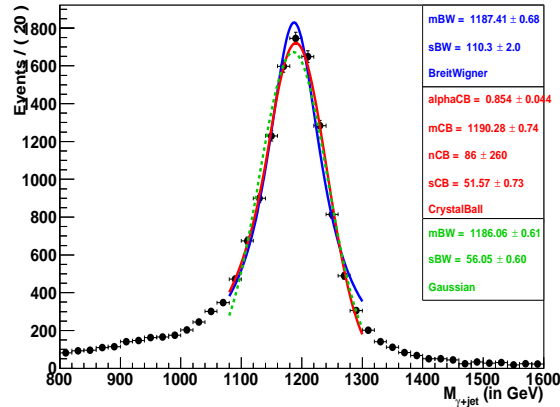
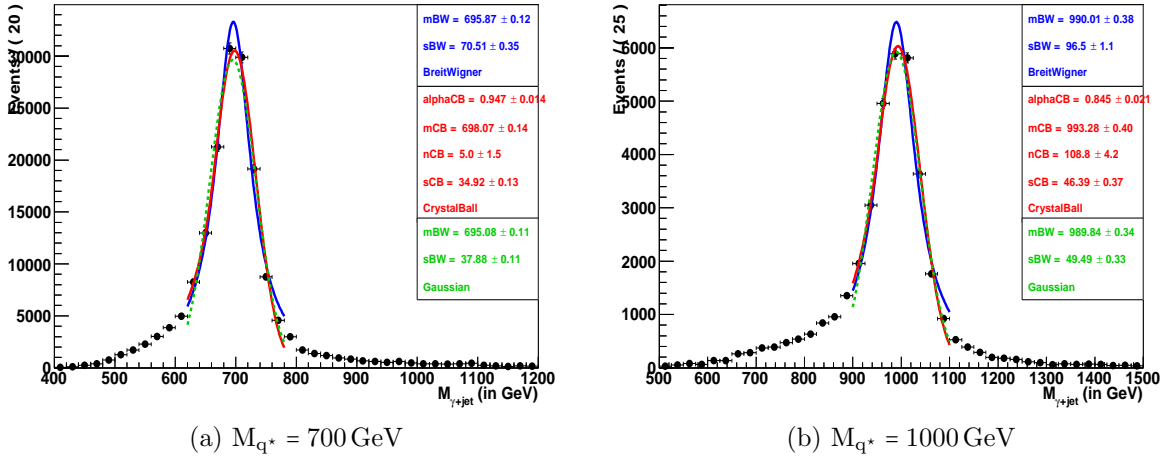
$$CB(m; \alpha, n, \mu, \sigma) = N_{CB} \cdot \begin{cases} \exp\left(-\frac{(m-\mu)^2}{2\sigma^2}\right), & \text{for } \frac{m-\mu}{\sigma} > -\alpha \\ \left(\frac{n}{|\alpha|}\right)^n \cdot \exp\left(-\frac{|\alpha|^2}{2}\right) \cdot \left(\frac{n}{|\alpha|} - |\alpha| - \frac{m-\mu}{\sigma}\right)^{-n}, & \text{for } \frac{m-\mu}{\sigma} \leq -\alpha, \end{cases} \quad (5.4)$$

where  $N_{CB}$  is a normalization factor and  $\alpha, n, \mu$  and  $\sigma$  are parameters which are fit to the data. It was used to compute the mass resolution, defined as  $\sigma/mean$  for various mass points of  $q^*$  signal. The mass resolution obtained by fitting  $q^*$  signal peaks with Crystal function (Eq 5.4), was again fit using Eq 5.5 to get a functional form for the invariant mass binning. In Eq 5.5,  $M_{Res}$  refers to the actual resonance mass of the  $q^*$  signal.

$$\frac{\sigma}{Mean} = A + \frac{B}{M_{Res}} \quad (5.5)$$

The fit to  $q^*$  mass resolution for different mass points has been illustrated in Fig 5.18. The binning obtained using this function, and used for different invariant mass distributions is mentioned below in an array named nMassBin[].

```
nMassBin[102] = {1, 3, 6, 10, 16, 23, 31, 40, 50, 61, 73, 86, 100, 115, 132, 150, 169, 189, 210,
232, 252, 273, 295, 318, 341, 365, 390, 416, 443, 471, 500, 530, 561, 593, 626,
660, 695, 731, 768, 806, 846, 887, 929, 972, 1017, 1063, 1110, 1159, 1209, 1261,
1315, 1370, 1427, 1486, 1547, 1609, 1673, 1739, 1807, 1877, 1950, 2025, 2102,
2182, 2264, 2349, 2436, 2526, 2619, 2714, 2812, 2913, 3018, 3126, 3237, 3352,
3470, 3592, 3718, 3847, 3980, 4117, 4259, 4405, 4556, 4711, 4871, 5036, 5206,
5381, 5562, 5748, 5940, 6138, 6342, 6552, 6769, 6993, 7223, 7461, 7706, 7959};
```



(c)  $M_{q^*} = 1200 \text{ GeV}$

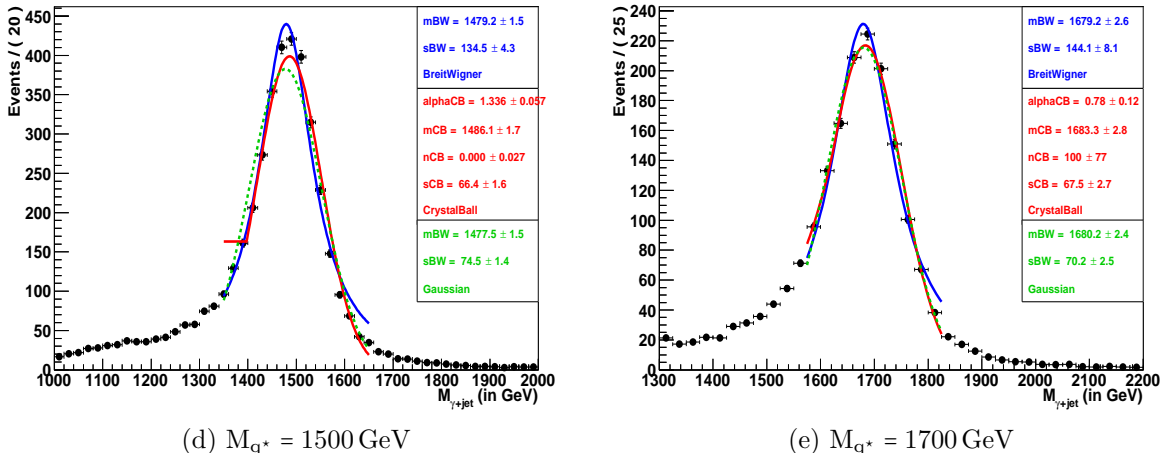


Figure 5.16: Fitting the core of  $q^*$  invariant mass for different samples of  $M_{q^*}$  from 700 to 1700 GeV with  $f = 1.0$  using Breit-Wigner (Blue), Crystal-Ball (Red), and Gaussian (Green) functions to get the mass resolution of each mass point.

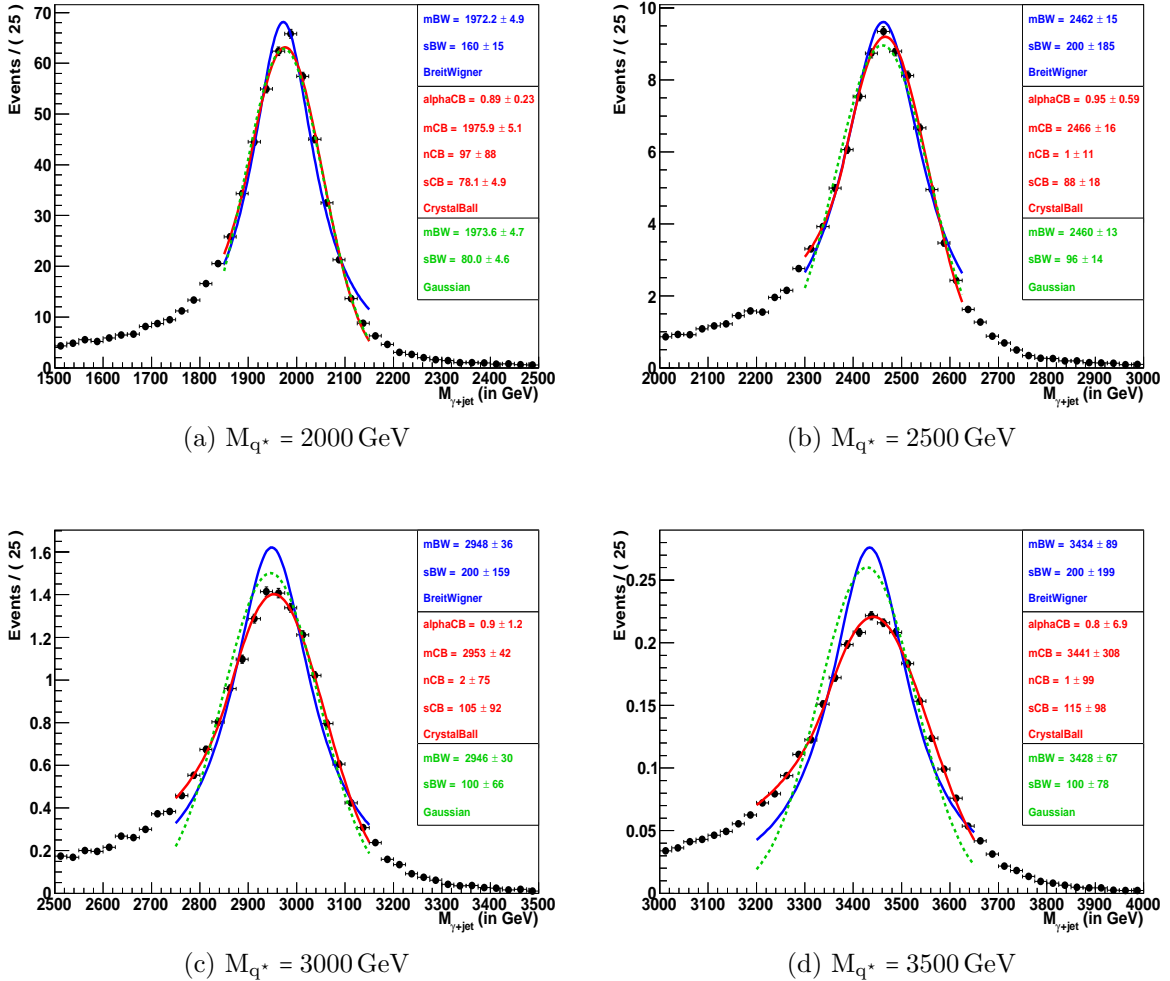


Figure 5.17: Fitting the core of  $q^*$  invariant mass for different samples of  $M_{q^*}$  from 2000 to 3500 GeV with  $f = 1.0$  using Breit-Wigner (Blue), Crystal-Ball (Red), and Gaussian (Green) functions to get the mass resolution of each mass point.

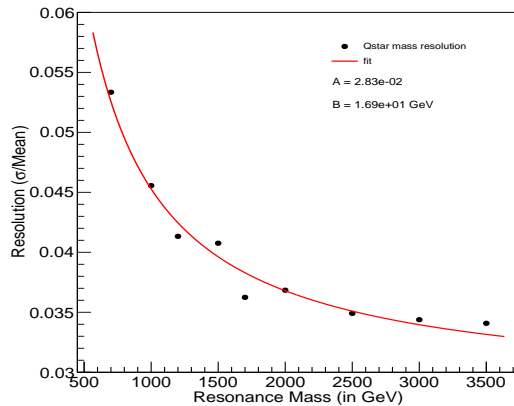


Figure 5.18: Fit function to get the variable binning from resolution of signal samples.

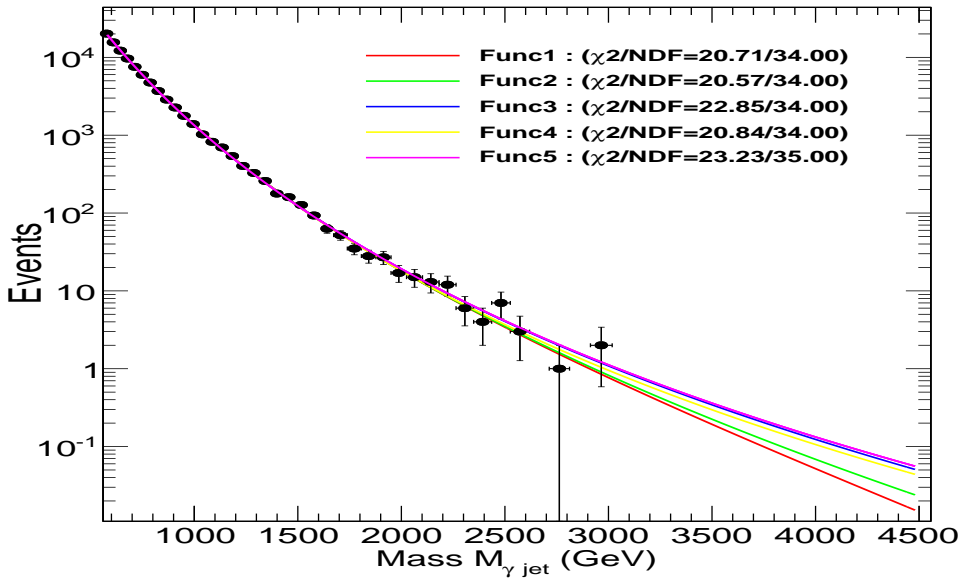
### 5.6.1 Choice of Fit function

The invariant mass distribution of both the MC simulation and data, illustrated in Fig 5.15 are plotted in bins of width similar to that of the expected mass resolution of  $q^*$ , which varies from 4.5% at 1 TeV to 3% at 3 TeV as obtained in the previous section. The MC simulation for background, while not used to compute the analysis results, is seen in Fig 5.15 to describe the data well, both in shape and yield.

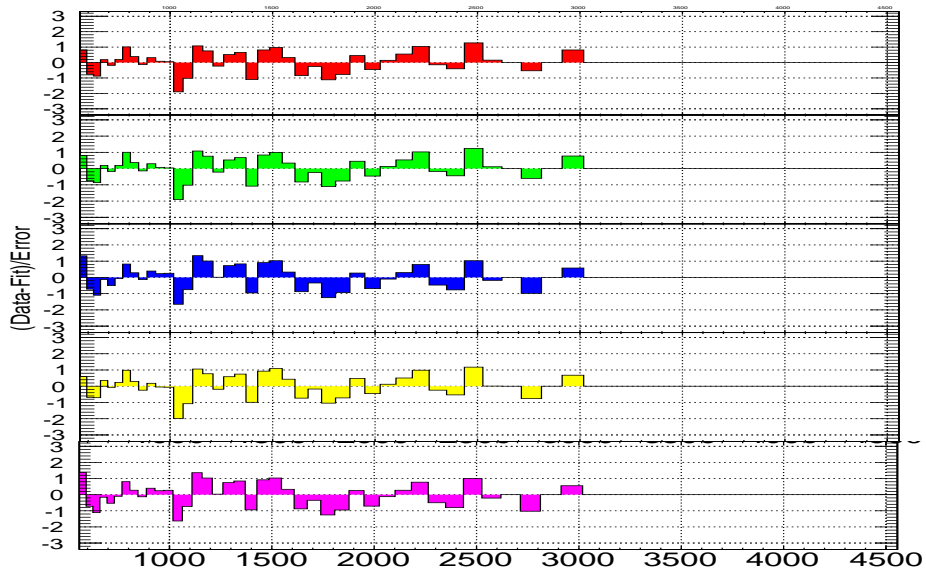
The heart of the search for the  $q^*$  resonance is the measurement of the  $\gamma +$  jet mass distribution and the estimation of the background. The traditional method to search for a large resonance signal used by previous experiments viz. UA2, CDF [159], is adopted, wherein background is estimated using a smooth parameterization. One can either use the MC simulations or the parameterized fit function estimated using the data to finally evaluate the background. In this analysis we have used the fit function to simulate the background. The advantage of using fit function is that even though the shape and normalization may agree between the data and the MC, there are still considerable theoretical uncertainties such as PDFs, renormalization scale, etc. and experimental uncertainties such as jet energy scale, resolution, etc. The methodology of smooth parameterization makes use of the fact that  $\gamma +$  jet background always produces a smooth and monotonically decreasing spectrum. To extract the smoothly falling background, the  $\gamma +$  jet invariant mass is fit to several functional forms used in searches for resonance signal at previous experiments, also discussed in Ref [159]. Functions that were tested to model the SM background in the best possible manner are:

- $F_1(x) = \frac{p_0 * (1+x)^{p_1}}{x^{p_2+p_3 \ln(x)}}$
- $F_2(x) = \frac{p_0 * (1-x)^{p_1}}{x^{p_2+p_3 \ln(x)}}$
- $F_3(x) = \frac{p_0}{p_1+p_2 x+x^{2p_3}}$
- $F_4(x) = \frac{p_0(1-x+p_3 x^2)^{p_1}}{m^{p_2}}$
- $F_5(x) = \frac{p_0}{(x+p_1)^{p_2}}$

where  $x = m/\sqrt{s}$ ,  $m$  being the  $\gamma +$  jet invariant mass,  $\sqrt{s}$  is the center-of-mass energy, and  $p_0$ ,  $p_1$ ,  $p_2$ , and  $p_3$  are the fit parameters. These parameterizations are motivated by LO QCD. The term  $x^{p_2}$  or  $m^{p_2}$  in the denominator mimics the QCD matrix element mass dependence and was introduced in searches at UA2 experiments [159]. The term  $(1 \pm x)^{p_1}$  in the numerator mimics the mass dependence of the parton distributions at an average



(a) Fit to data with different fit functions described in the text.



(b) Residuals for all the fit function on the same scale.

Figure 5.19: Fit  $\gamma +$  jet invariant mass in data using different fit function.

fractional momentum of  $m/\sqrt{s}$  and was introduced by CDF [159]. The  $p_3$  term was added in order to model the data at high invariant mass.

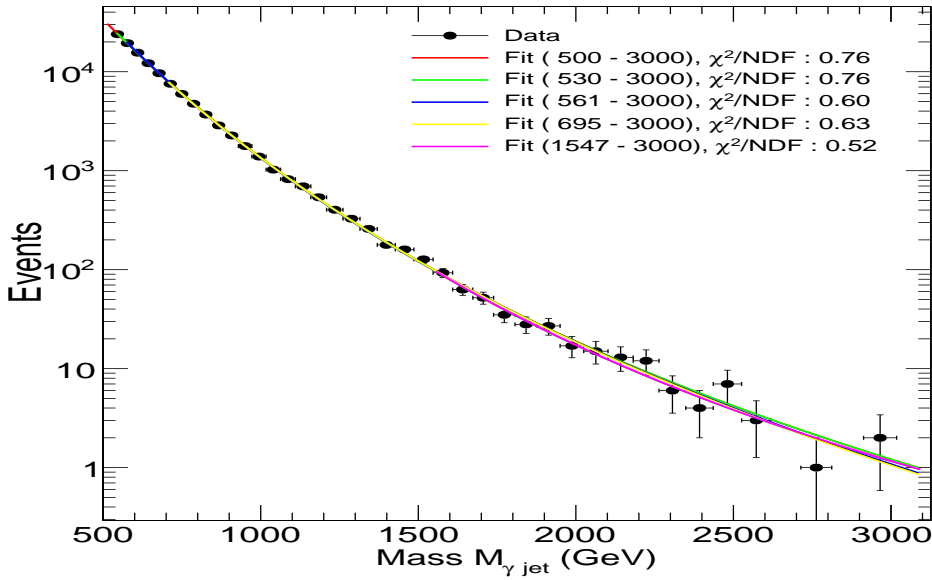
Fit to data with the above set of functions is shown in Fig 5.19a, while their residuals, i.e.,  $(\text{Data} - \text{Fit})/\sigma_{Data}$  are reported in Fig 5.19b. Though, almost all the functions describe the data well, the function  $F_2$ , which has a good comparison with a full NLO QCD calculation from fastNLO was chosen for this study as shown in Ref [160]. This function is also used by the ATLAS experiment for resonance search in the  $\gamma + \text{jet}$  and the dijet final states [79, 161] and the CMS experiment in the dijet final state [162]. It also had a slightly better  $\chi^2/ndf$  and less fluctuations in all the mass bins when compared with other four functions as can be seen in Fig 5.19a, where  $\chi^2/ndf$  for all the fit functions are listed in the top right corner of the plot.

The modeling of the  $\gamma + \text{jet}$  background is based on the smooth parametrization  $F_2$ ,

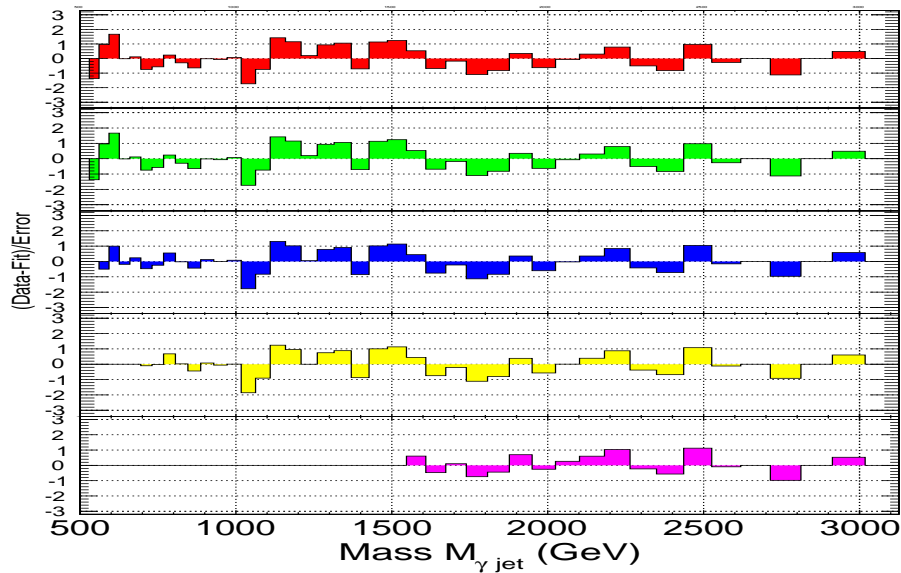
$$\frac{d\sigma}{dm} = \frac{P_0(1 - m/\sqrt{s})^{P_1}}{(m/\sqrt{s})^{P_2 + P_3 \ln(m/\sqrt{s})}} \quad (5.6)$$

where  $\sqrt{s} = 8 \text{ TeV}$ , and  $P_0 = 2.74277 \times 10^{-3} \pm 1.199 \times 10^{-4}$ ,  $P_1 = 3.33455 \pm 1.831 \times 10^{-1}$ ,  $P_2 = 8.06973 \pm 1.745 \times 10^{-2}$ , and  $P_3 = 7.47310 \times 10^{-1} \pm 5.88315 \times 10^{-3}$  are the 4-parameters used to describe the background. The fit probability tells us whether the data is smooth, or not, which is the first test for the presence of a resonance. To check the stability of this function for fit to data, and avoid any bias from statistically rich low mass region, different mass range were chosen, and were fit using the same function. The result of the fit with different mass ranges is shown in Fig 5.20.

The difference between the data and the fit, referred to as residuals, is used to estimate the significance of the largest upward fluctuation in the data interpreted as a narrow resonance. The parametrization in Eq 5.6, gives a good description of both the observed data and simulated background, as shown in Fig 5.21. The resulting fit has a  $\chi^2$  of 20.57 for 34 degrees of freedom. The residual difference between the fit and observed data for each mass bin, as shown at the bottom of Fig 5.21, do not show significant difference



(a) Fit to data for  $F_2$  over different mass range



(b) Residuals for fit to data for  $F_2$  over different mass range

Figure 5.20: Fit to data with different fit ranges.

between the two. The largest fluctuations in the data are seen at  $\sim 1.5$  and  $2.3$  TeV of mass but are not significant enough to claim any evidence of a resonance and are consistent with background fluctuation. Figure 5.21 also shows simulated  $q^*$  resonance peaks for  $1.0$  and  $1.5$  TeV with  $f = 1.0$  and a resonance peak at  $2.5$  TeV with  $f = 0.5$ .

The event with highest  $\gamma +$  jet invariant mass in data was observed at  $2934$  GeV. The

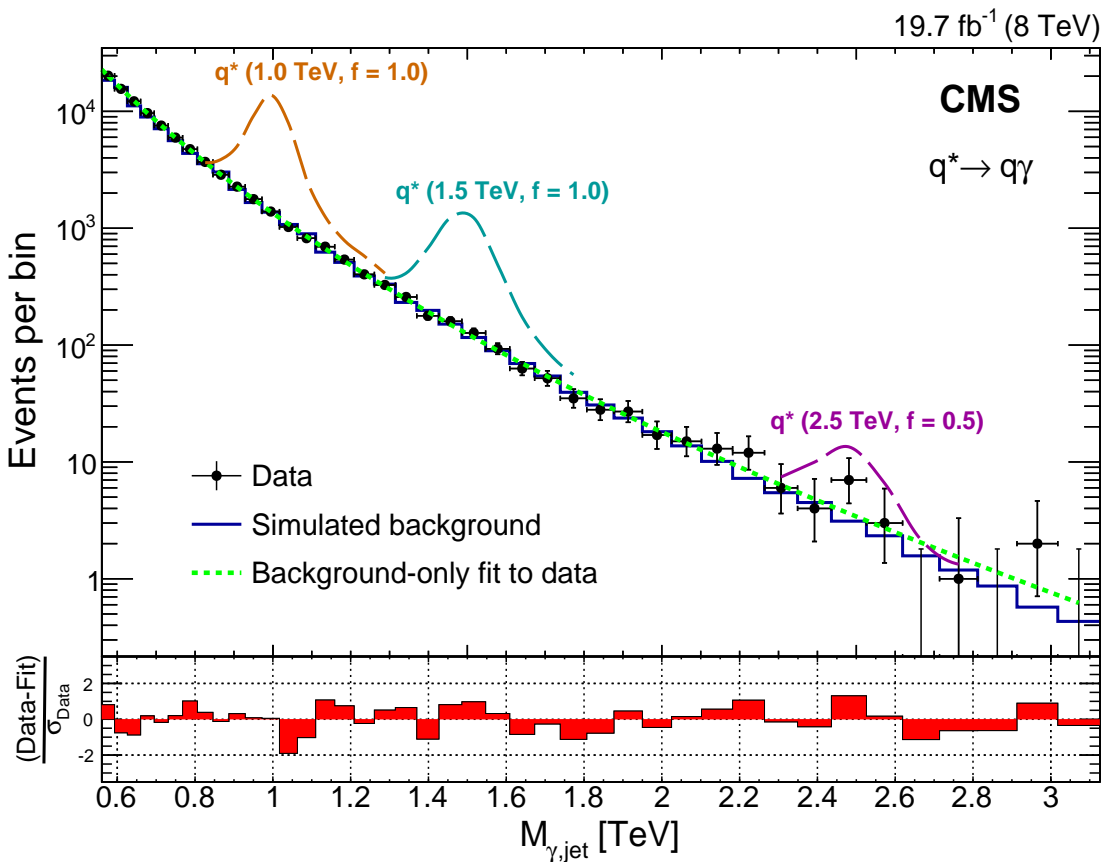
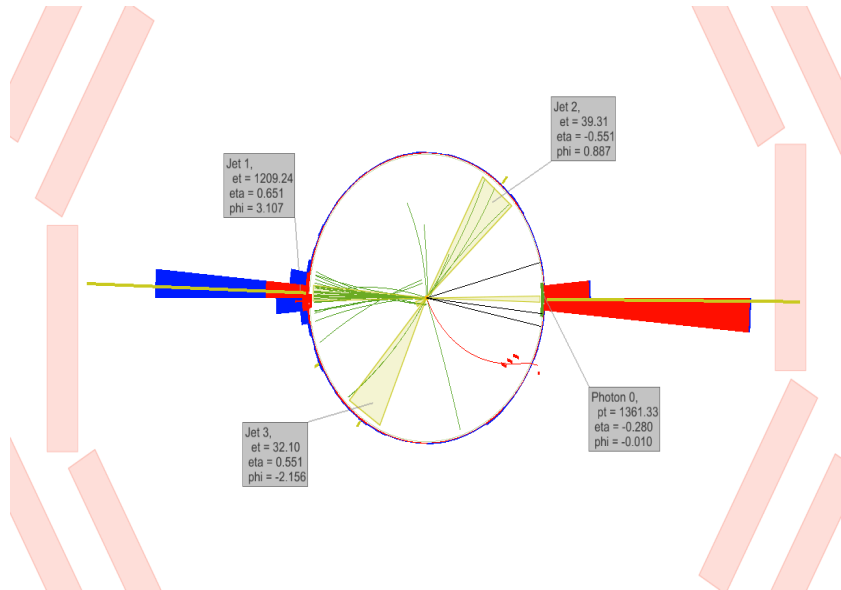


Figure 5.21: The  $\gamma + \text{jet}$  invariant mass spectrum from data, the result of the fit with fit error, and residuals.

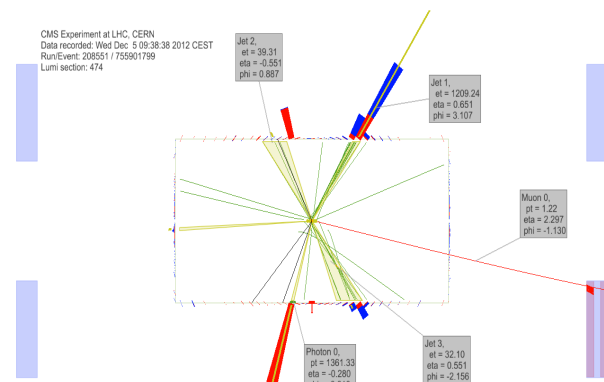
event display for the event with highest mass after passing the full selection criteria was made using cmsShow package [163] in several planes viz.  $r-\phi$ ,  $\rho-z$ , and 3-dimensional, and is reported in Fig 5.22. It is a very well balanced  $\gamma + \text{jet}$  event from: Run Number-208551, Lumisection-474, and Event Number-755901799. The  $p_T$  of the photon reconstructed in this event was found to be 1361 GeV and that of jet was 1280 GeV. The event was recorded by the CMS detector on 5<sup>th</sup> December 2012 and thus could be found in Run2012D dataset.

## 5.7 Interpolation technique

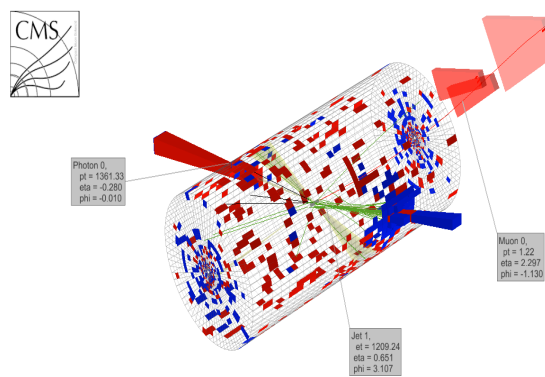
When searching for new resonances or particles, *a priori*, we do not have the knowledge of mass point where to expect a peak, and hence need to scan the entire mass range possible.



(a)  $r - \phi$  plane



(b)  $\rho - z$  plane



(c) 3-dimensional view

Figure 5.22: Graphic display for highest  $\gamma + \text{jet}$  invariant mass event in different geometric planes, with  $M_{\gamma,\text{jet}} = 2934.4 \text{ GeV}$ ,  $p_T^\gamma = 1361.3 \text{ GeV}$  and  $p_T^{\text{jet}} = 1280.2 \text{ GeV}$ .

For this study only 20  $q^*$  signal mass points were generated using event generators ranging from 700 GeV to 4.5 TeV, 11 for coupling  $f = 1.0$  and 9 for  $f = 0.5$ . To study the

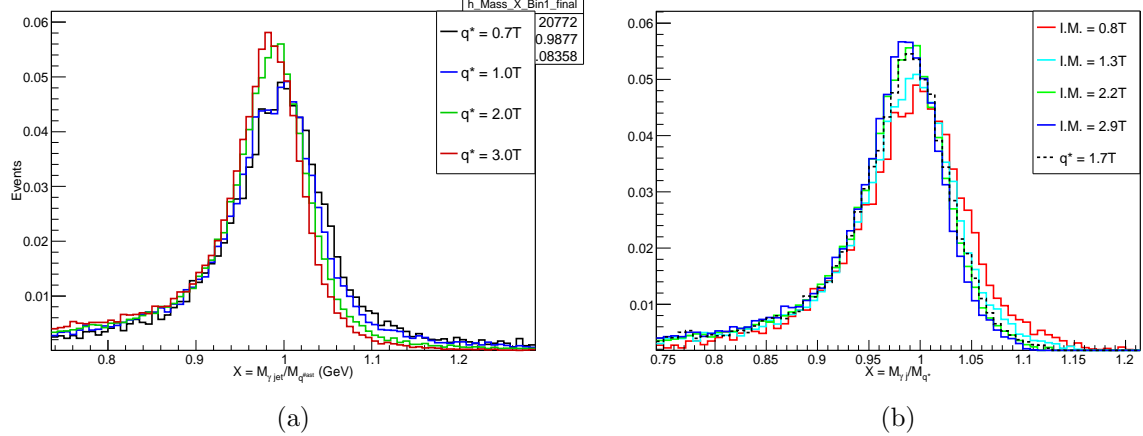


Figure 5.23:  $X$  distribution for excited quark with different mass points for generated and Interpolated samples.

intermediate mass region, the shape of resonances at mass values that were not generated are obtained using an interpolation technique [164], wherein information is extracted from the nearest neighboring generated mass points. Here, at first a new parameter,  $X = \frac{M_{\gamma, \text{jet}}}{M_{\text{Res}}}$  is defined, where,  $M_{\gamma, \text{jet}}$  is the  $\gamma$ +jet mass and  $M_{\text{Res}}$  is resonance mass. The  $X$  distribution is computed for all the generated  $q^*$  mass points and the comparison of these distributions for various  $q^*$  mass points is reported in Fig 5.23a. Then,  $X$  distributions for the mass points that has to be interpolated were generated using Eq 5.7. If a resonance mass  $M$  lies between the generated mass point  $M_A$  and  $M_B$ , ( $A < B$ ) following equation is applied to obtain the  $X$  distribution,

$$Prob_M(X) = Prob_A(X) + [Prob_B(X) - Prob_A(X)] \cdot \frac{M - M_A}{M_B - M_A} \quad (5.7)$$

where,  $Prob_M(X)$ , gives the probability of a mass point defined by  $X$ . For example, to generate distribution of a resonance with mass of 1.7 TeV, the first thing is to search for its nearest generated masses. Since 1.5 TeV and 2.0 TeV are the immediate neighbors,

they form  $M_A$  and  $M_B$ , leaving the above equation to the following,

$$Prob_{1.7\text{TeV}}(X) = Prob_{1.5\text{TeV}}(X) + [Prob_{2.0\text{TeV}}(X) - Prob_{1.5}(X)] \cdot \frac{1.7 - 1.5}{2.0 - 1.5} \quad (5.8)$$

The comparison of  $X$  distribution of the interpolated mass points with those that were generated is shown in Fig 5.23b. Lastly, the  $X$  distribution for the interpolated mass point was multiplied with the respective resonance mass value and converted to variable  $\gamma + \text{jet}$  binning using Eq 5.5 to obtain the final  $q^*$  resonance mass shape at respective mass value. The fully interpolated mass point for some of the mass values is shown in Fig 5.24, where, solid lines are for the generated samples and dotted lines represent interpolated mass shapes.

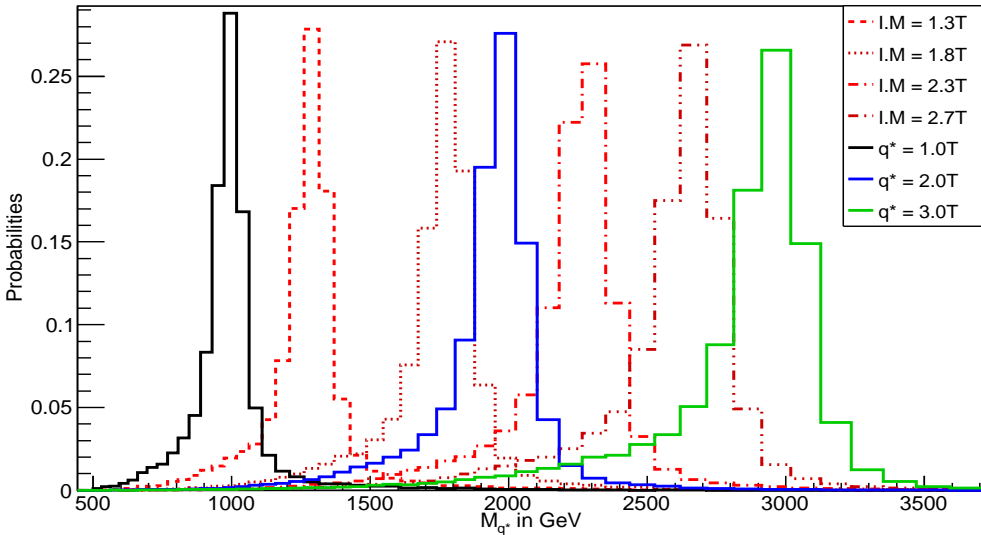


Figure 5.24: Comparison of  $q^*$  resonance shapes for the generated and interpolated samples. The solid lines are from the generated samples ( $q^*$ ) while dotted lines represent interpolated samples (I.M.).

To verify this technique a closure test was performed in which an already generated mass point, viz. 2.5 TeV, was chosen to be interpolated using its immediate neighbors, viz. 2.0 and 3.0 TeV. The shape of the interpolated 2.5 TeV mass point was then compared with its generated shape and a good agreement was observed, as reported in Fig 5.25. A similar comparison for  $q^*$  with mass 1.0 TeV is also shown in the same figure, which

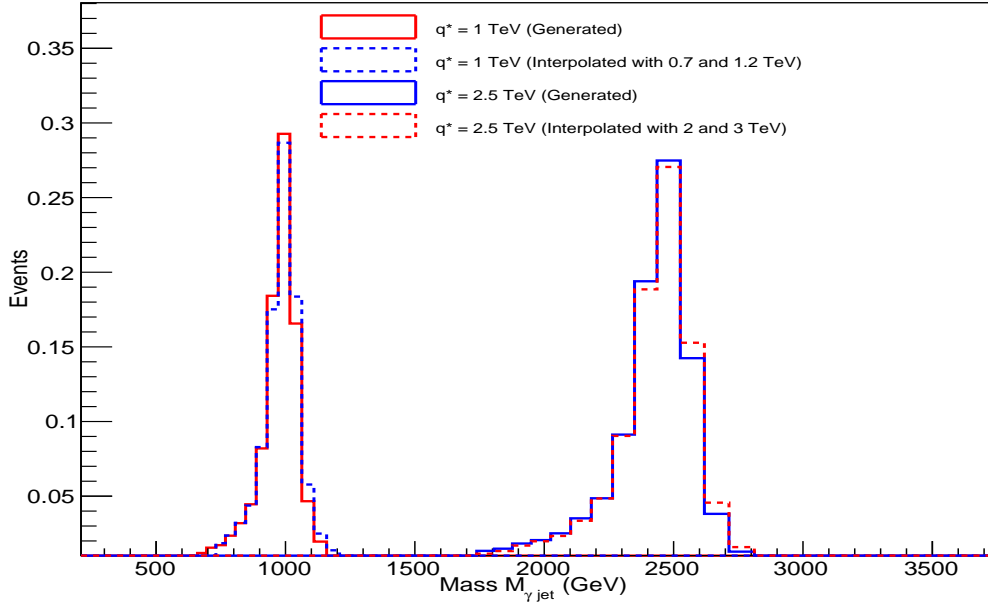


Figure 5.25: Comparison of  $q^*$  resonance shape for generated (solid lines) and interpolated (dotted lines) excited quark at 1.0 and 2.5 TeV.

is interpolated using 0.7 and 1.2 TeV generated  $q^*$  sample. To add weight to this test, observed cross section was also evaluated using both the shapes, result of which are described in Section 5.9.1.

## 5.8 Systematic Uncertainties

There are various sources of systematic uncertainties in this analysis, such as those due to reconstructed objects identification inefficiencies, energy scales, measurement in luminosity, etc. In this section, I describe the most significant of them and they are listed below:

- Photon and Jet Energy Calibration Scale
- Photon and Jet Energy Resolution
- Final State Radiations
- Background Shape
- Theoretical Uncertainty

- Pile-up Uncertainty

- Luminosity

Only Background shape uncertainty is included in background since the background shape is derived from data and the rest of the uncertainties are considered for the resonance signal shapes alone.

### 5.8.1 Photon and Jet Energy Calibration Scale

The energy measured in calorimeters is different from the true particle-level energy. The difference is caused primarily by the non-uniform and non-linear response of the calorimeters. Therefore, corrections are made to the energy scale of the reconstructed photons and jets.

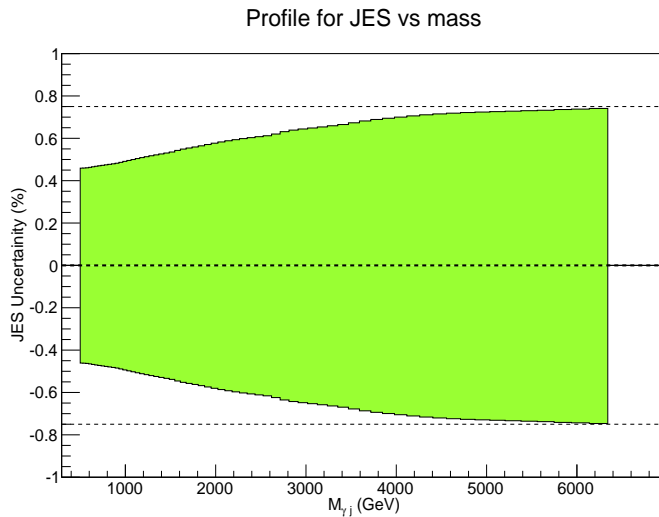


Figure 5.26: Uncertainty in jet Energy Scale as a function of mass.

The photon energy scale (PES) uncertainty [165, 166] was found to be about 1.5%, while the jet energy scale (JES) uncertainty [165] was found to vary between 1.0 – 1.4%. The effect of the photon and jet energy scale uncertainty was studied on the  $\gamma +$  jet mass spectrum of the  $q^*$  signal, wherein the four-momenta of photon and jet is varied by  $1 \pm$  uncertainties and is reported in Fig 5.26 and 5.27. It was found to have an effect of 0.75% on the  $q^*$  resonance shape in the case of photons and 0.8% for jets.

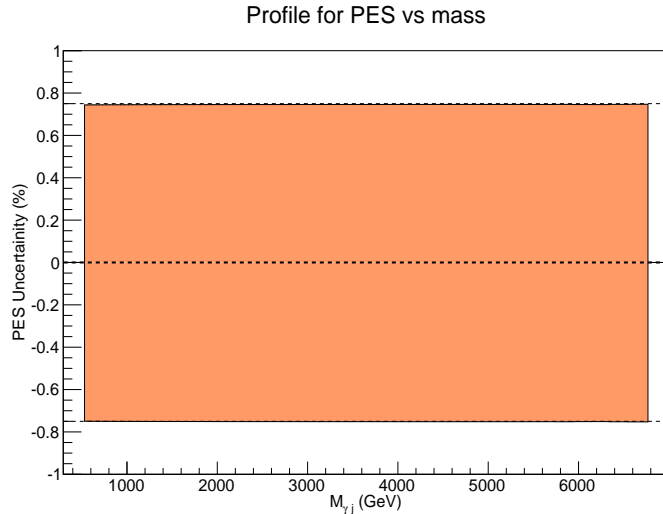


Figure 5.27: Uncertainty in photon energy scale as a function of mass.

### 5.8.2 Photon and Jet Energy Resolution

If the  $\gamma +$  jet mass resolution of the simulated  $q^*$  signal is wider or smaller than what we expect, it may be harder to find a resonance, as it may either spread over a large number of bins or get contained in just a few of them. So, it is important to incorporate the uncertainty due to energy resolution. The uncertainty on the jet energy resolution(JER) [165] and photon energy resolution(PER) [167] was taken to be 10% and 0.5%, respectively. The uncertainty in JER and PER translates into a relative uncertainty of 5% on the  $\gamma +$  jet mass and is propagated to the search by changing the width of the resonance shape, which results in slight stretching or shrinking of the resonance shape itself.

### 5.8.3 Final State Radiations

The initial state radiation (ISR) and the final state radiation (FSR) could also affect the shape of  $q^*$  resonances. The effect of ISR is small and mostly contained in the low mass tail but FSR could affect the determination of the mean and width of these resonances significantly. The effect of FSR depends on the choice of the scale. Within PYTHIA [112], this is controlled by a parameter, PARJ(81), set at 0.29 for the nominal scenario. To estimate the uncertainty due to FSR, the parameter value was scaled by a factor of 2.0

and 0.5. The change in mean was found to be  $\pm 0.5\%$  as reported in Table 5.6, for both

FastSim Signal	PARJ(81)	Mean (GeV)	Width (GeV)	Expected Limit	Observed Limit
1 TeV Down	0.145	988.48	57.08	0.0154572	0.00885582
1 TeV Nominal	0.29	993.08	61.35	0.0153808	0.00980415
1 TeV Up	0.58	995.6	59.15	0.0161674	0.00927311
3 TeV Down	0.145	2941.81	149.68	0.000457463	0.00034185
3 TeV Nominal	0.29	2951.8	144.25	0.000457362	0.000352528
3 TeV Up	0.58	2958.39	144.70	0.000473748	0.000365025

Table 5.6: Effect of change in Final state radiations on the mean and width of FASTSIM  $q^*$  shapes at 1 TeV and 3 TeV.

a low and a high mass signal. The change in width was found to be 7% (4%) for 1 TeV (3 TeV)  $q^*$  mass shapes generated using FASTSIM [168]. In Table 5.6, ‘Down’ refers to scaling by factor 0.5 while, ‘Up’ means by a factor of 2.0.

#### 5.8.4 Background Shape Uncertainty

To estimate the uncertainty due to the background fit, different functional forms were tested to parametrize the data, as shown in Fig 5.19. The statistical uncertainty in the prediction of fit using the chosen function was estimated to be 1% at 1 TeV and about 30% at 3 TeV. A signal-plus-background fit to the data was performed to identify a reasonable starting point for each of the four parameter values. Covariance matrix of the 4 background parameters ( $P_0, P_1, P_2, P_3$ ) was diagonalized and the variations of the original 4 parameters along the 4 eigenvectors of the covariance matrix were introduced as nuisance parameters. These nuisance parameters were integrated over a  $\pm 7\sigma$  range, around the best fit values, where  $\sigma$  is the square root of the corresponding eigenvalue of the covariance matrix. It had been verified that the result remains stable if a bigger integration interval was chosen.

#### 5.8.5 Theoretical Uncertainty

Theoretical uncertainties, here, refer to the choice of factorization and renormalization scales. These were varied by a factor of 0.5 and 2.0, separately, to estimate the variation

in the signal cross section for different resonances masses. The uncertainties in the signal due to the variation in scales were found to be about 4%.

### 5.8.6 Pileup Uncertainty

A central value for the total inelastic cross section of 69.4 mb [169, 170] has been used for pp collisions at 8 TeV. The number of interactions in the data is estimated from the measured luminosity in each bunch crossing times the total inelastic cross section. A variation of  $\pm 5\%$  in the number of interactions has been done to cover the uncertainties due to the pileup reweighting. This includes an additional  $\sim 3\%$  uncertainty to cover all the physics aspects of the pileup simulation. The effect of pileup uncertainty on the product (acceptance  $\times$  efficiency) of  $q^*$  signal samples were found to be  $\sim 0.3\%$ .

### 5.8.7 Luminosity

The total uncertainty on the integrated luminosity [170] delivered to the CMS experiment by the LHC in pp collisions for the 2012 physics run was estimated to be 2.6%.

## 5.9 Limit setting procedure

As no significant excess is observed in data with respect to the background expectations, we proceed to set upper limits on the cross section of excited quarks in the  $\gamma +$ jet channel. A Bayesian technique [171] based on a binned likelihood method is used to search for the  $q^*$  resonances. The binned likelihood uses three distributions in the  $\gamma +$ jet invariant mass: data, background, and signal. For each  $\gamma +$ jet invariant mass bin,  $i$ ,

- Signal: number of events from  $q^*$  signal simulated samples,  $N_i(S)$ .
- Data: measured number of events in data,  $n_i$ .
- Background: expected number of events from the background fit,  $N_i(B)$ .

The normalization of the  $q^*$  signal is multiplied with a normalization parameter  $\alpha$ , and added in background to obtain the mean number of expected events  $\mu_i$  , for each  $\gamma + \text{jet}$  invariant mass bin  $i$  :

$$\mu_i = \alpha N_i(S) + N_i(B) \quad (5.9)$$

The likelihood,  $\mathcal{L}(n|\mu)$ , of observing  $n_i$  events when  $\mu_i$  are predicted is given by Poisson statistics :

$$\mathcal{L}(n|\mu) = \prod_{i=1}^{\text{Total Bins}} \frac{\mu_i^{n_i} e^{-\mu_i}}{n_i!} \quad (5.10)$$

The limit code [172] is based on the ROOT TMinuit class. The bin width size is approximately of the  $\gamma + \text{jet}$  mass resolution, and gradually increases as a function of mass according to the  $\gamma + \text{jet}$  mass resolution. The binned likelihood  $\mathcal{L}$  is used to evaluate the number of expected background events in each bin by integrating the chosen fit function over the bin width. The resulting fit function with the signal cross section set to zero is used as the background hypothesis. This provides the expected number of background events in the  $i$ th  $\gamma + \text{jet}$  mass bin,  $N_i(B)$ . The number of signal events in the same mass bin,  $N_i(S)$ , comes from the signal histogram templates. For the mass points for which  $q^*$  signal samples were not simulated using event generators, signal templates were taken using the interpolated samples as described in Section 5.7. We assume a flat prior in normalization parameter  $\alpha$ , which is the same as a flat prior in the resonance cross section. The likelihood function is multiplied by the flat prior in cross section,  $P(\sigma)$ , and normalized to give a posterior probability density in cross section:

$$P_{post}(\sigma) = \frac{\mathcal{L}(n|\mu)P(\sigma)}{\int_0^\infty \mathcal{L}(n|\mu)P(\sigma)d\sigma} \quad (5.11)$$

Log-normal prior distribution functions were used [173] to model the systematic uncertainties which are treated as nuisance parameter. The posterior probability density was calculated as a function of signal cross section for resonances with masses starting from 0.7 TeV to 4.5 TeV in steps of 100 GeV. Finally, the 95% confidence level upper limit

on the cross section,  $\sigma_{95}$  were calculated from the posterior probability density as follows:

$$\int_0^{\sigma_{95}} P_{POST}(\sigma) d\sigma = 0.95 \quad (5.12)$$

The systematic uncertainties in JES, PES, JER, PER, FSR, in the integrated luminosity, and in the correction factors are used in the limit setting procedure as nuisance parameters and affect only the signal. They were used to evaluate model independent limits on  $\sigma \times \mathcal{B}$ .

### 5.9.1 Optimization

To verify the interpolation technique, two  $q^*$  samples with  $M_{q^*} = 1.0 \text{ TeV}$  and  $2.5 \text{ TeV}$ , that were already generated using PYTHIA event generator, were interpolated using the techniques described in Section 5.7. For the  $M_{q^*} = 1.0 \text{ TeV}$  case, 0.7 and 1.2 TeV generated

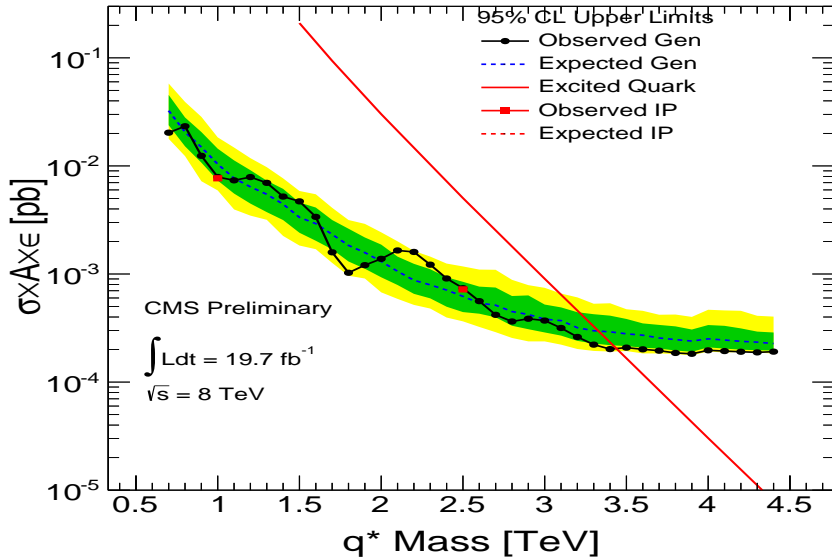


Figure 5.28: Comparison of interpolated (red dots) and generated signal shapes (black dots) based on the observed limits.

$q^*$  samples were used for interpolation, while 2.0 and 3.0 TeV samples were used in the case of 2.5 TeV. The 95% CL upper limits on the  $\sigma \times A \times \epsilon$  were evaluated using the interpolated shapes and the generated shapes. The comparison of the two is shown in

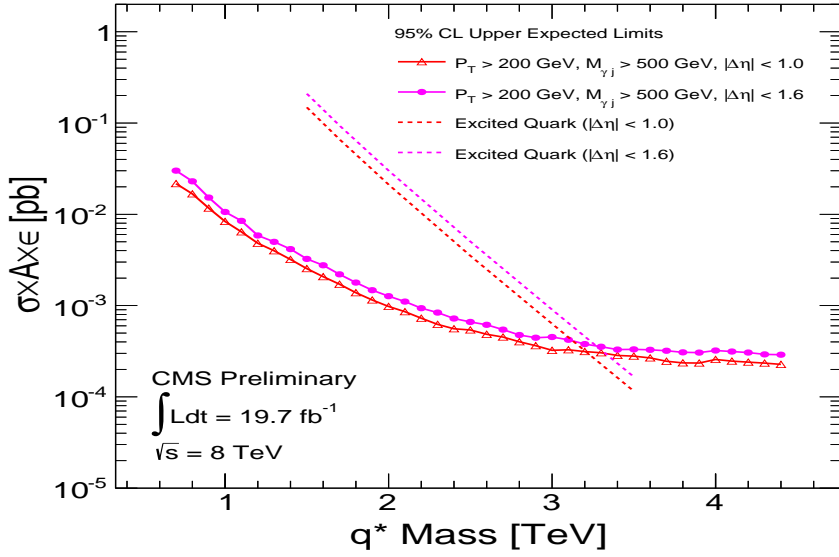


Figure 5.29: Optimization based on the expected limits with different  $\Delta\eta$  selection criteria.

Fig 5.28 and a very good agreement between the two can be observed.

To optimize the selection of  $\Delta\eta$  between the leading photon and jet, lower limit on the expected mass of  $q^*$  were compared for different set of selection values. Figure 5.29 shows that with increasing  $\Delta\eta$  selection the expected mass limit improves. To study the exact

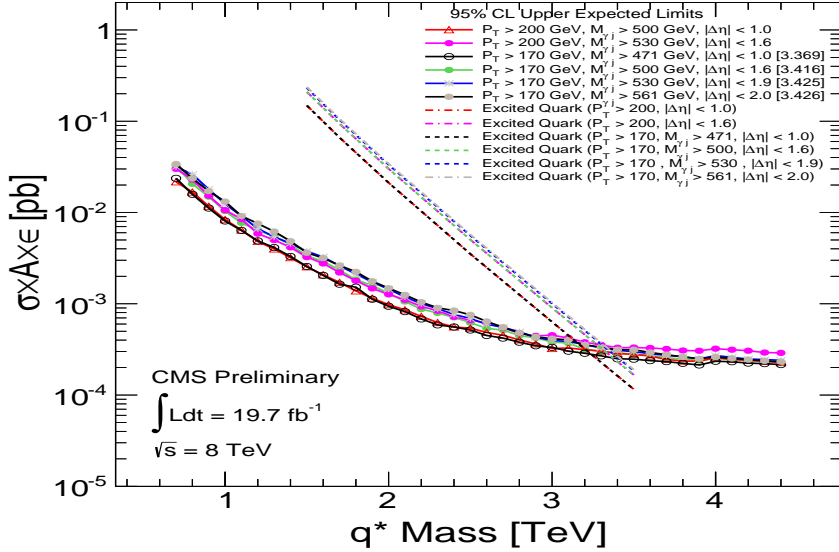


Figure 5.30: Optimization based on the expected limits with different criteria on  $p_T$ ,  $\Delta\eta$  and mass selections.

behavior, different values of  $\Delta\eta$  were considered as shown in Fig 5.30. The expected mass

Optimization of $\Delta\eta$	Expected Limit (in GeV)
$p_T^\gamma > 170 \text{ GeV}, M_{\gamma,\text{jet}} > 471 \text{ GeV}, \Delta\eta < 1.0$	3.369
$p_T^\gamma > 170 \text{ GeV}, M_{\gamma,\text{jet}} > 500 \text{ GeV}, \Delta\eta < 1.6$	3.416
$p_T^\gamma > 170 \text{ GeV}, M_{\gamma,\text{jet}} > 530 \text{ GeV}, \Delta\eta < 1.9$	3.425
$p_T^\gamma > 170 \text{ GeV}, M_{\gamma,\text{jet}} > 560 \text{ GeV}, \Delta\eta < 2.0$	3.426
$p_T^\gamma > 170 \text{ GeV}, M_{\gamma,\text{jet}} > 560 \text{ GeV}, \Delta\eta < 2.2$	3.418
$p_T^\gamma > 170 \text{ GeV}, M_{\gamma,\text{jet}} > 560 \text{ GeV}, \Delta\eta < 2.5$	3.373

Table 5.7: Table showing expected limits for different cases of optimization.

limits obtained for various values of  $\Delta\eta$  requirement is tabulated in Table 5.7 and it was found that a value of  $\Delta\eta = 2.0$  gives the best expected mass limit. Different selection on  $\Delta\eta$  lead to different turn-on region in the invariant mass distribution as seen in Fig 5.31. A selection of 2.0 on the  $\Delta\eta$  requirement lead to a selection of 560 GeV on the invariant mass distribution on  $\gamma + \text{jet}$ . Finally,  $\Delta\eta = 2.0$  has been used to set the limit on search for  $q^*$  in  $\gamma + \text{jet}$  channel in this thesis.

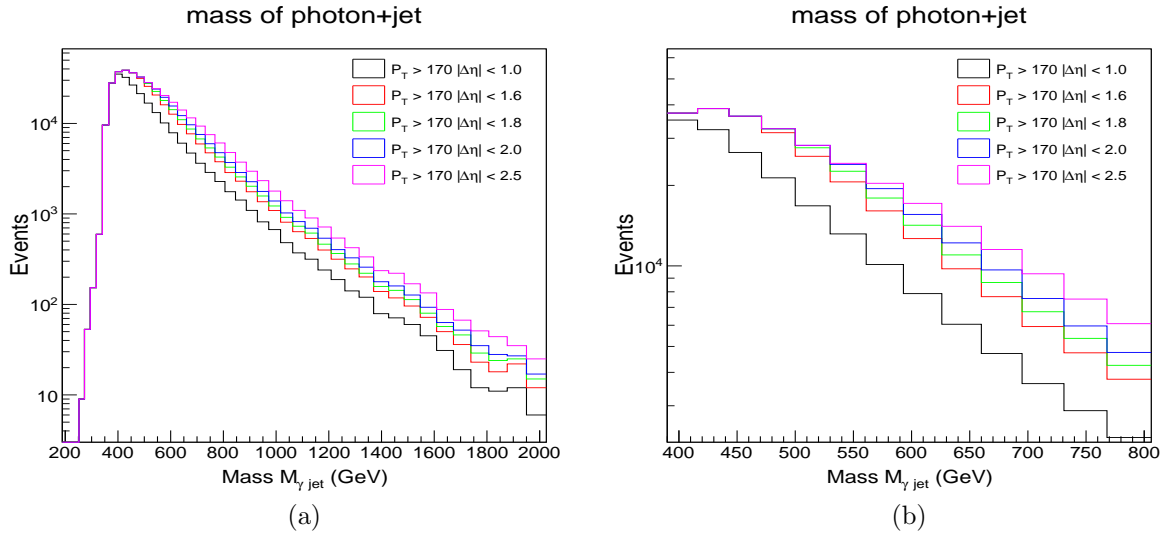


Figure 5.31: Turn on region in the  $\gamma + \text{jet}$  invariant mass plot for different selection criteria.



# Chapter 6

## Results and Summary

This chapter presents the results of the study for search of excited quarks in the  $\gamma$ +jet final state at the CMS experiment using  $19.7\text{ fb}^{-1}$  of proton-proton collision data at  $\sqrt{s} = 8\text{ TeV}$  and finally summarizes the results.

### 6.1 Results

The expected and observed 95% confidence level (CL) upper limits on the  $\sigma \times \mathcal{B} \times A \times \epsilon$  for excited quarks,  $q^*$ , as a function of the mass of  $q^*$  ( $M_{q^*}$ ) in the  $\gamma$ +jet final state for coupling multiplier,  $f = 1.0$  has been shown in Fig 6.1. Here,  $\sigma$  is the production cross section,  $\mathcal{B}$  is the branching ratio and  $A \times \epsilon$  refers to the acceptance  $\times$  efficiency of the  $q^*$  signal. For the  $q^*$  signal,  $A \times \epsilon$  was found to range from 54% to 58% for  $M_{q^*}$  ranging from 1 TeV to 4 TeV as reported in Table 5.4. Figure 6.2 depicts 95% CL upper limits for the case when  $f = 0.5$ . The observed upper limits were found to be consistent with those expected in the absence of a signal. These limits were computed up to a  $q^*$  mass of 4.4 TeV, since at higher masses, off-shell production dominates, thus reducing the sensitivity of the search. As mentioned in Section 5.8, to estimate the cross section upper limits, all major sources of systematic uncertainties have been considered.

Figures 6.3 and 6.4, respectively, show the model independent limits on  $\sigma \times \mathcal{B}$  for coupling multipliers,  $f = 1.0$  and  $f = 0.5$ . For estimating these model independent

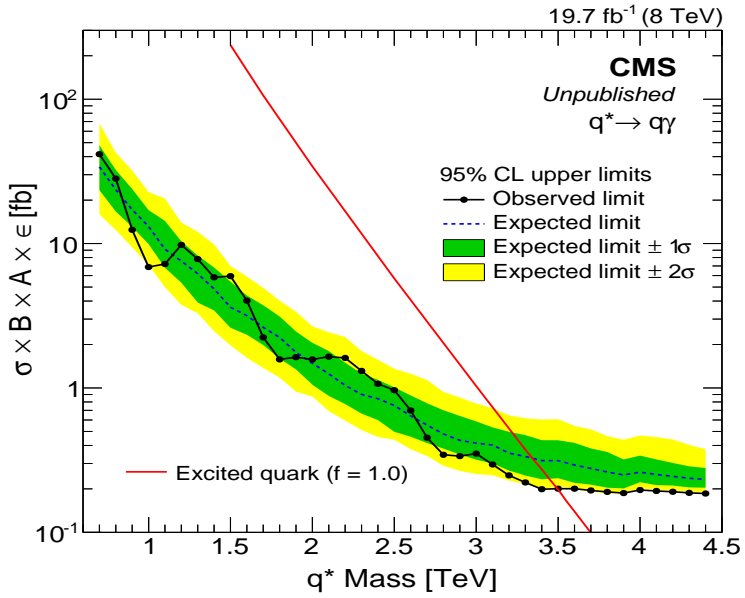


Figure 6.1: The expected and observed 95% CL upper limits on  $\sigma \times B \times A \times \epsilon$  for  $q^* \rightarrow \gamma + \text{jet}$  with coupling parameter  $f = 1.0$ . The upper limits are also compared with theoretical prediction for  $q^*$  production. The uncertainty at  $1\sigma$  and  $2\sigma$  levels are shown as green and yellow bands, around the expected limit.

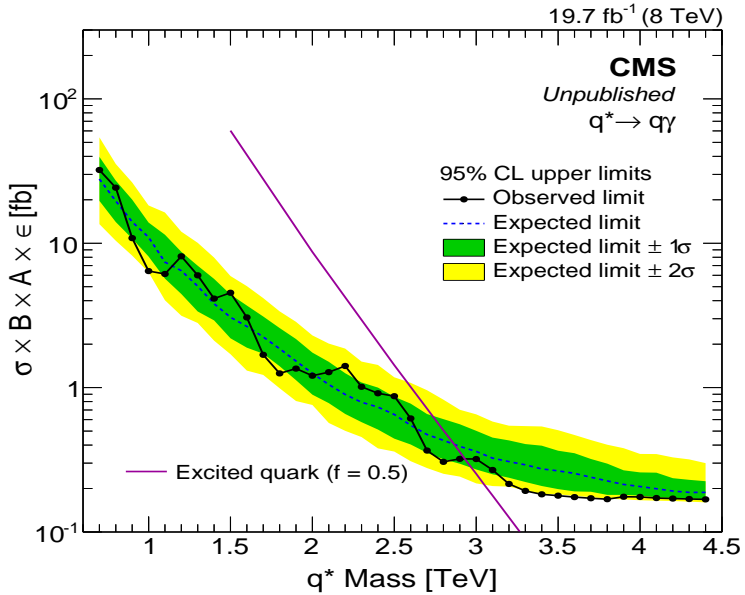


Figure 6.2: The expected and observed 95% CL upper limits on  $\sigma \times B \times A \times \epsilon$  for  $q^* \rightarrow \gamma + \text{jet}$  with coupling parameter  $f = 0.5$ . The upper limits are also compared with theoretical prediction for  $q^*$  production. The uncertainty at  $1\sigma$  and  $2\sigma$  levels are shown as green and yellow bands, around the expected limit.

limits on the cross section an additional systematics uncertainty of 4% on correction factors and statistical uncertainty on  $A \times \epsilon$ , was propagated in the limit setting procedure.

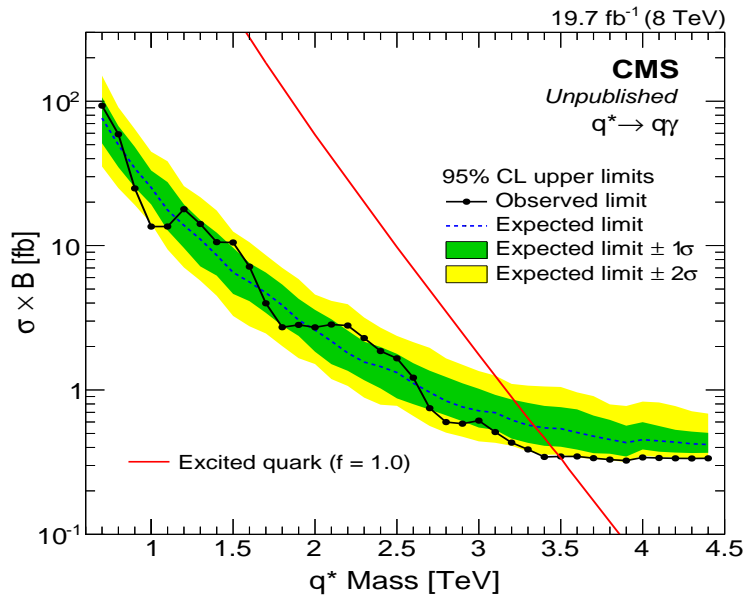


Figure 6.3: The expected and observed 95% CL upper limits on  $\sigma \times \mathcal{B}$  for  $q^* \rightarrow \gamma + \text{jet}$  with coupling parameter  $f = 1.0$ . The upper limits are also compared with theoretical predictions for  $q^*$  production. The uncertainty at  $1\sigma$  and  $2\sigma$  levels are shown as green and yellow bands, around the expected limit.

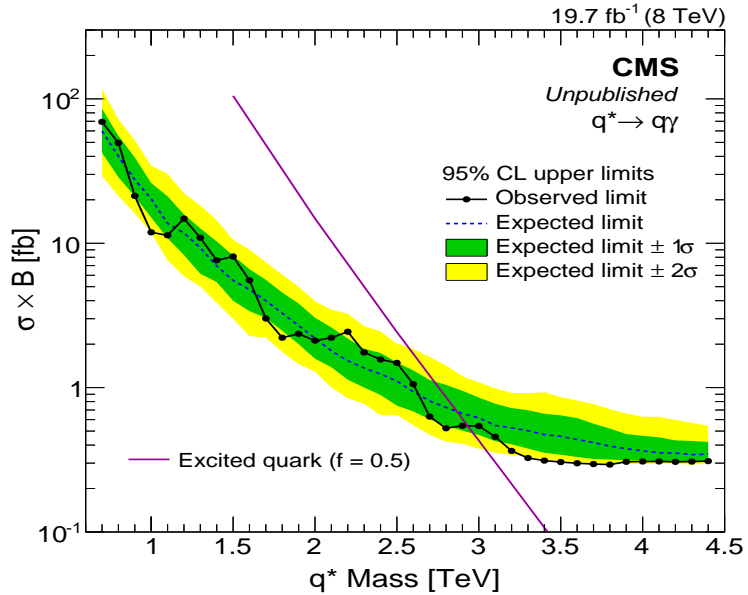


Figure 6.4: The expected and observed 95% CL upper limits on  $\sigma \times \mathcal{B}$  for  $q^* \rightarrow \gamma + \text{jet}$  with coupling parameter  $f = 0.5$ . The upper limits are also compared with theoretical predictions for  $q^*$  production. The uncertainty at  $1\sigma$  and  $2\sigma$  levels are shown as green and yellow bands, around the expected limit.

The observed upper limits were compared to the leading order theoretical predictions to estimate the lower mass bounds on the excited quarks as shown in Figs 6.3 and 6.4. A

lower bound of 3.5 TeV (2.9 TeV) on the mass of  $q^*$  is set for coupling multipliers,  $f = 1.0$  (0.5). The corresponding expected limits were found to be 3.4 (2.8) TeV.

These cross section upper limits for coupling multiplier half the strength of standard couplings  $f = 1.0$ , i.e.,  $f = 0.5$  are the first set of results from any LHC experiment at 8 TeV. The comparison of observed limits for  $f = 0.5$  and  $f = 1.0$  coupling scenarios has been shown in Fig 6.5. Table 6.1 shows the comparison of expected and observed limits for couplings  $f = 0.5$  and  $f = 1.0$  in a tabular form. Figure 6.6 shows the expected and observed 95% CL upper limit on  $\sigma \times \mathcal{B}$  for  $q^*$  and a comparison with theoretical predictions for couplings  $f = 1.0$  and  $f = 0.5$  on the same canvas. If one takes into account the theoretical uncertainty on signal, the observed limit on  $M_{q^*}$  changes by  $\pm 0.2\%$ .

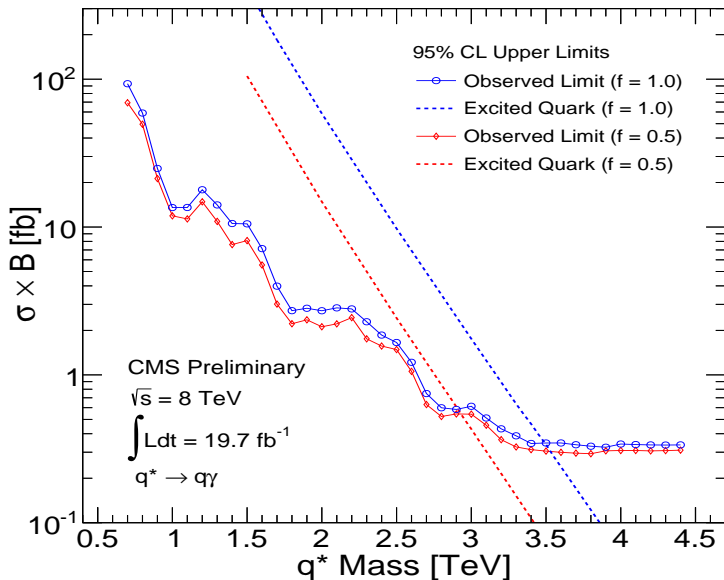


Figure 6.5: Comparison of observed limits for excited quarks with  $f = 0.5$  and  $1.0$  respectively.

As the observed width of  $q^*$  resonance is dominated by the experimental resolution, the dependence of  $\sigma \times \mathcal{B}$  cross section upper limit on  $f$  was found to be negligible for  $f \leq 1$ . Using the theoretical predictions, cross sections were evaluated for various  $q^*$  mass points for different couplings ranging from  $f = 1.0$  to as low as  $f = 0.04$  as reported in Table 6.2. These theoretical predictions were then used to exclude the mass of excited quarks for respective set of coupling strength as shown in Fig 6.7.

Mass ( TeV)	$f = 0.5$		$f = 1.0$	
	Expected	Observed	Expected	Observed
0.7	59.954	69.295	76.369	93.179
0.8	40.079	49.590	49.836	59.039
0.9	27.571	21.270	34.298	24.896
1.0	20.329	11.904	25.235	13.543
1.1	13.721	11.348	17.629	13.559
1.2	11.776	14.815	13.806	17.872
1.3	9.2835	10.919	11.073	14.112
1.4	6.9799	7.6101	8.5730	10.564
1.5	5.5258	8.0946	6.5187	10.508
1.6	4.7815	5.5372	5.5947	7.1461
1.7	3.9969	3.0119	4.7100	3.9834
1.8	3.2762	2.2179	3.8666	2.7188
1.9	2.6871	2.3577	3.0480	2.8226
2.0	2.1982	2.1161	2.6015	2.7155
2.1	1.8008	2.2140	2.1788	2.8401
2.2	1.5338	2.4396	1.8017	2.7940
2.3	1.3667	1.7533	1.5616	2.2873
2.4	1.2400	1.5670	1.4529	1.8591
2.5	1.1111	1.4838	1.3205	1.6559
2.6	0.9361	1.0562	1.1133	1.2165
2.7	0.8079	0.6300	0.9645	0.7477
2.8	0.7286	0.5232	0.8387	0.5991
2.9	0.6610	0.5442	0.7625	0.5839
3.0	0.6179	0.5424	0.7173	0.6132
3.1	0.5474	0.4566	0.6965	0.5111
3.2	0.5271	0.3646	0.6197	0.4316
3.3	0.5026	0.3255	0.5708	0.3871
3.4	0.4729	0.3123	0.5463	0.3436
3.5	0.4597	0.3051	0.5394	0.3462
3.6	0.4365	0.2994	0.5071	0.3463
3.7	0.4163	0.2956	0.4783	0.3369
3.8	0.3933	0.2930	0.4537	0.3292
3.9	0.3773	0.3065	0.4319	0.3241
4.0	0.3648	0.3080	0.4527	0.3407
4.1	0.3537	0.3081	0.4436	0.3378
4.2	0.3522	0.3061	0.4352	0.3360
4.3	0.3433	0.3075	0.4237	0.3353
4.4	0.3464	0.3096	0.4187	0.3361

Table 6.1: Expected and observed 95% CL upper limits on  $\sigma \times \mathcal{B}$  (in fb) as a function of resonance mass for couplings strengths  $f = 0.5$  and  $1.0$  respectively.

Couplings <i>f</i>	Mass (in GeV)								
	700	1000	1500	2000	2500	3000	3500	4000	4500
0.04	3.962e-2	6.859e-3	6.743e-4	5.918e-10	-	-	-	-	-
0.05	6.219e-2	1.078e-2	1.047e-3	5.966e-8	-	-	-	-	-
0.07	1.217e-1	2.102e-2	2.074e-3	5.890e-6	-	-	-	-	-
0.1	-	4.268e-2	4.222e-3	5.940e-4	9.721e-5	1.700e-5	2.989e-6	4.841e-7	7.163e-8
0.2	-	1.707e-1	1.699e-2	2.377e-3	3.921e-4	6.831e-5	1.189e-5	1.950e-6	2.839e-7
0.3	-	3.863e-1	3.782e-2	5.298e-3	8.754e-4	1.547e-4	2.657e-5	4.389e-6	6.518e-7
0.4	-	6.838e-1	6.692e-2	9.497e-3	1.546e-3	2.738e-4	4.784e-5	7.837e-6	1.180e-6
0.5	-	1.061e-0	1.047e-1	1.481e-2	2.436e-3	4.298e-4	7.575e-5	1.258e-5	1.928e-6
0.6	-	1.541e-0	1.507e-1	2.129e-2	3.522e-3	6.233e-4	1.101e-4	1.882e-5	3.023e-6
0.7	-	2.088e-0	2.050e-1	2.897e-2	4.756e-3	8.479e-4	1.512e-4	2.659e-5	4.574e-6
0.8	-	2.695e-0	2.653e-1	3.751e-2	6.212e-3	1.111e-3	2.009e-4	3.602e-5	6.422e-6
0.9	-	3.388e-0	3.364e-1	4.736e-2	7.898e-3	1.404e-3	2.601e-4	4.727e-5	8.772e-6
1.0	-	4.177e-0	4.121e-1	5.830e-2	9.718e-3	1.761e-3	3.245e-4	6.041e-5	1.174e-5

Table 6.2: Cross section (in pb) of  $q^*$  signal samples for different couplings ( $f = 0.04$  to  $1.0$ ).

Based on the lower mass limit for different set of coupling strengths as reported in Fig 6.7, a mass region is excluded as a function of coupling parameter  $f$  and is shown in Fig 6.8. The results depicted in Fig 6.8 may also be used to present the limits on the excited quark mass,  $M_{q^*}$ , as a function of compositeness scale,  $\Lambda$ , if the assumption  $\Lambda = M_{q^*}$  is relaxed. This is justified as variation in  $f$  and in  $M_{q^*}/\Lambda$  also result in similar effect on the  $q^*$  cross section. For example, if we assume  $\Lambda = 10 M_{q^*}$  and standard model couplings, then using Fig 6.8 we exclude excited quarks with mass  $0.7 < M_{q^*} < 1.2$  TeV.

## 6.2 Summary

This thesis presents a search for excited quarks in the  $\gamma +$  jet final state using  $19.7 \text{ fb}^{-1}$  of proton-proton collision data at  $\sqrt{s} = 8 \text{ TeV}$  at the CMS experiment. The data are found to be consistent with the standard model predictions and upper limits are placed on the  $\sigma \times \mathcal{B}$  for  $q^*$  predictions in the  $\gamma +$  jet final state. The experimental techniques used in this analysis can be summarized as follows:

- Measure the  $\gamma +$  jet invariant mass spectrum.
- Compare the measured invariant mass spectrum to simulated standard model Monte Carlo predictions.

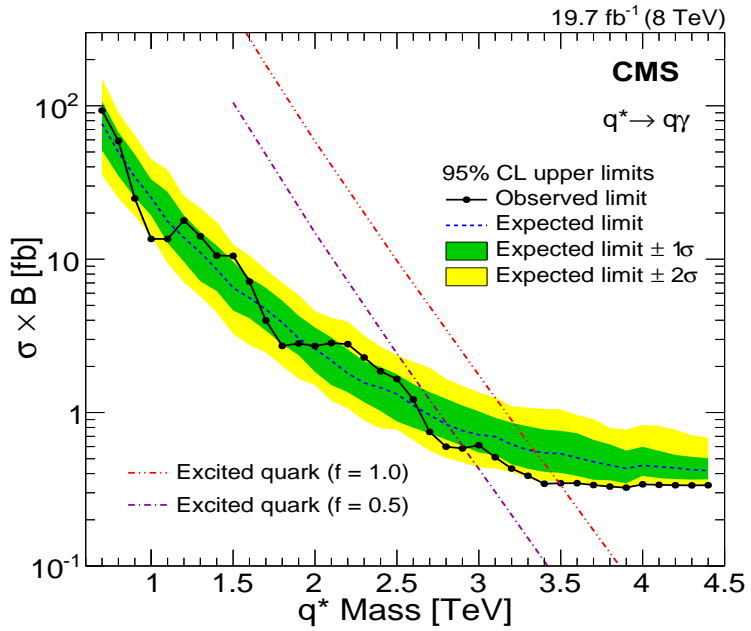


Figure 6.6: The expected and observed 95% CL upper limits on  $\sigma \times \mathcal{B}$  for  $q^* \rightarrow \gamma + \text{jet}$  production, and comparison with theoretical predictions for coupling parameters  $f = 0.5$  and  $f = 1.0$  respectively. The uncertainty at  $1\sigma$  and  $2\sigma$  levels are shown as green and yellow bands, around the expected limits.

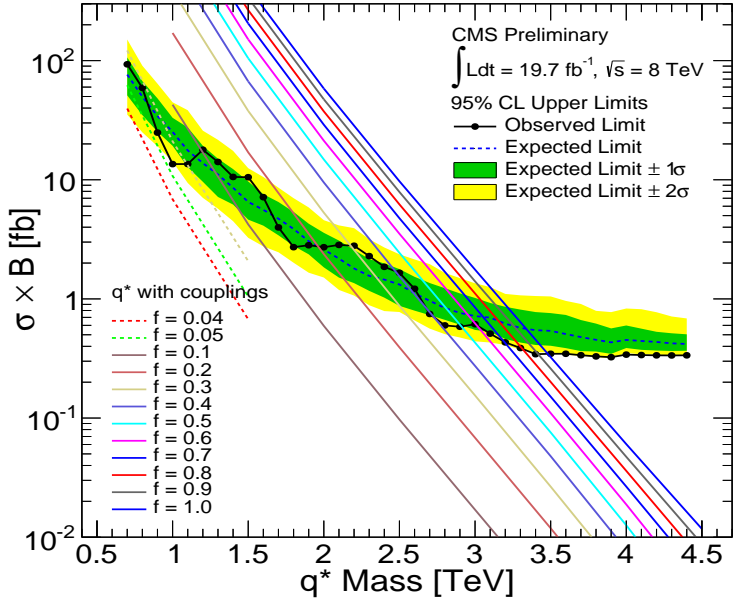


Figure 6.7: The expected and observed 95% CL upper limits on  $\sigma \times \mathcal{B}$  of excited quarks for coupling parameter  $f$ , ranging from  $f = 0.004$  to  $1.0$ .

- Fit the measured  $\gamma + \text{jet}$  invariant mass spectrum with a smooth parametrization and search for a resonant signal.

- If there is no evidence for the  $\gamma +$  jet resonance, evaluate model independent cross section upper limits and compare with the theoretical cross section prediction of the excited quark model.
- Set the exclusion mass limits for the excited quark model.

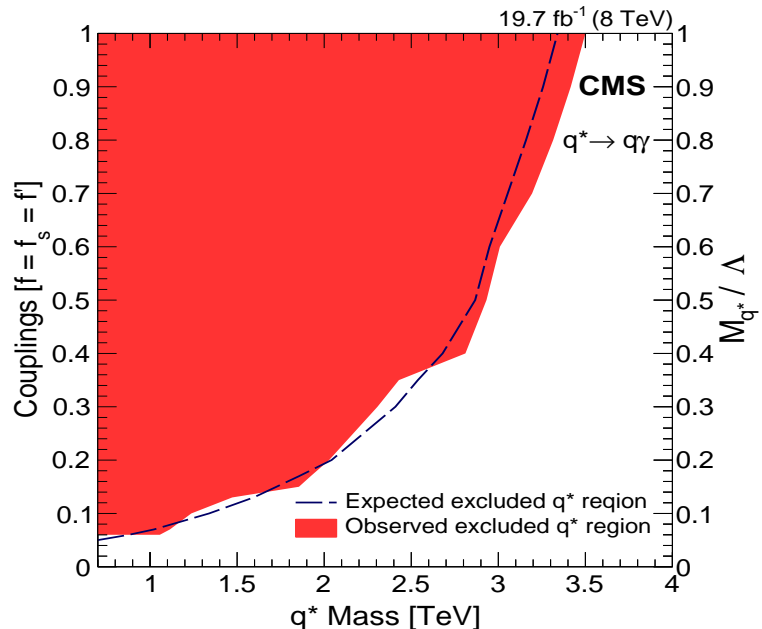


Figure 6.8: The expected (dashed) and observed (red filled) excluded regions at 95% CL as a function of  $q^*$  mass and coupling strength for  $\Lambda = M_{q^*}$  (left axis) or the  $M_{q^*}/\Lambda$  for coupling strength  $f = 1$  (right axis).

Comparing the cross section upper limits with the theoretical predictions, excited quarks with masses in the range,  $0.7 < M_{q^*} < 3.5$  TeV are excluded at 95% confidence level limit under the assumption  $f = 1.0$ .

For the first time at the LHC experiment, the sensitivity of the excited quark search has also been investigated for coupling strength less than unity, as illustrated in Fig 6.8. Excited quark masses in the range  $0.7 < M_{q^*} < 2.9$  TeV are excluded for  $f = 0.5$ . Furthermore, excited quarks with masses in the range  $0.7 < M_{q^*} < 1.0$  TeV are excluded for coupling value  $f$  as low as  $f = 0.06$ .

The work presented in this thesis has been published in Physics Letters B 738 (2014) 274-293.

# Glossary

**ALICE** A Large Ion Collider Experiment.

**AOD** Analysis Object Data (A format to store processed data).

**APDs** Silicon Avalanche Photodiodes (photo-detectors in EB).

**ATLAS** A Large Toroidal LHC Accelerator System.

**BNL AGS** Brookhaven National Laboratory, Alternating Gradient Synchrotron.

**BPIX** Barrel region of the pixel detectors.

**CDF** Collider Detector at Fermilab.

**CERN** The European Organization for Nuclear Research.

**CMS** Compact Muon Solenoid.

**CMSSW** CMS Software Framework.

**CRAB** CMS Remote Analysis Builder.

**CSC** Cathode Strip Chambers (sub-detector of muon system).

**CTF** Combinatorial Track Finder.

**D0** Experiment in Tevatron Collider at Fermilab.

**DAQ** Data Acquisition System.

**DT** Drift Tubes (sub-detector of muon system).

**EB** Barrel region ( $|\eta| < 1.48$ ) of the electromagnetic calorimeter.

**ECAL** Electromagnetic Calorimeter.

**EE** Endcap region ( $1.48 < |\eta| < 3.00$ ) of the Electromagnetic calorimeter.

**FEDs** Front End Drives.

**FPIX** Forward region of the pixel detectors.

**FSR** Final State Radiations.

**GCT** Global Calorimeter Trigger.

**GMT** Global Muon Trigger.

**GT** Global Trigger.

**HB** Barrel region ( $|\eta| < 1.3$ ) of the hadronic calorimeter.

**HCAL** Hadronic Calorimeter.

**HE** Endcap region ( $1.3 < |\eta| < 3.0$ ) of the hadronic calorimeter.

**HERA** Hadron Electron Ring Accelerator.

**HF** Forward region ( $3.0 < |\eta| < 5.0$ ) of the hadronic calorimeter.

**HLT** High Level Trigger.

**HO** Outer region of the hadronic calorimeter.

**HPDs** Hybrid Photodiodes (photo-detectors in HCAL).

**ISR** Initial State Radiations.

**JER** Jet Energy Resolution.

**JES** Jet Energy Calibration Scale.

**LEP** Large Electron Positron Collider.

**LHC** Large Hadron Collider.

**LHCb** Large Hadron Collider beauty Experiment.

**LICTD** Largest Intra Cluster Time Difference.

**LINAC2** Linear Accelerator.

**LO** Leading Order.

**MC** Monte Carlo simulated dataset.

**NLO** Next-to-Leading Order.

**PDFs** Parton Distribution Functions.

**PER** Photon Energy Resolution.

**PES** Photon Energy Calibration Scale.

**PF** Particle Flow (algorithm to reconstruct particles).

**PS** Proton Synchrotron.

**PSB** Proton Synchrotron Booster.

**PU** Pile-up (addition interations in a single bunch crossing).

**PV** Primary Vertex.

**QCD** Quantum Chromodynamics.

**QED** Quantum Electrodynamics.

**RCT** Regional Calorimeter Trigger.

**RECO** Reconstructed Data Format.

**RPC** Resistive Plate Chambers (sub-detector of muon system).

**SCs** Superclusters (clusters of energy depositions in ECAL).

**SLAC** Stanford Linear Accelerator Center at Stanford University, USA.

**SM** Standard Model.

**SPEAR** Stanford Positron Electron Asymmetric Rings.

**SPS** Super Proton Synchrotron.

**TEC** Endcap region of the tracker.

**TIB** Inner barrel region of the tracker.

**TID** Inner disks of the tracker.

**TOB** Outer barrel region of the tracker.

**TTC** Trigger Timing and Control.

**TTS** Trigger Throttling System.

**VPTs** Vacuum Phototriodes (photo-detectors in EE).

**WLS** Wavelength-shifting fibres used in plastic scintillators in HCAL.

# Bibliography

- [1] S. L. Glashow, “Partial Symmetries of Weak Interactions”, *Nucl. Phys.* **22** (1961) 579–588, doi:10.1016/0029-5582(61)90469-2.
- [2] A. Salam and J. C. Ward, “Electromagnetic and weak interactions”, *Phys. Lett.* **13** (1964) 168–171, doi:10.1016/0031-9163(64)90711-5.
- [3] S. Weinberg, “A Model of Leptons”, *Phys. Rev. Lett.* **19** (1967) 1264–1266, doi:10.1103/PhysRevLett.19.1264.
- [4] J. J. Thomson, “Cathode Rays”, *Philosophical Magazine* **44** (1897) 293.
- [5] E. Rutherford, “The scattering of alpha and beta particles by matter and the structure of the atom”, *Phil. Mag.* **21** (1911) 669–688, doi:10.1080/14786440508637080.
- [6] E. Rutherford, “The structure of the atom”, *Nature* **92** (1913) 423.
- [7] N. Bohr, “On the constitution of atoms and molecules”, *Philosophical Magazine* **26** (1914) 1.
- [8] J. Chadwick, “Possible Existence of a Neutron”, *Nature* **129** (1932) 312.
- [9] A. Einstein, “On the electrodynamics of moving bodies”, *Annalen Phys.* **17** (1905) 891–921, doi:10.1002/andp.200590006. [Annalen Phys.14,194(2005)].
- [10] A. H. Compton, “A Quantum Theory of the Scattering of X-rays by Light Elements”, *Phys. Rev.* **21** (1923) 483–502, doi:10.1103/PhysRev.21.483.

- [11] P. A. M. Dirac, “The Quantum Theory of the Emission and Absorption of Radiation”, *Proc. R. Soc. Lond. A114* **243** (1927) 710.
- [12] C. D. Anderson, “The Positive Electron”, *Phys. Rev.* **43** (1933) 491–494, doi:10.1103/PhysRev.43.491.
- [13] E. Fermi, “Fermi’s Theory of Beta Decay”, *Z. Phys.* **88** (1934) 161.
- [14] C. L. Cowan et al., “Detection of the free neutrino: A Confirmation”, *Science* **124** (1956) 103–104, doi:10.1126/science.124.3212.103.
- [15] H. Yukawa, “On the Interaction of Elementary Particles I”, *Proc. Phys. Math. Soc. Jap.* **17** (1935) 48–57, doi:10.1143/PTPS.1.1. [Prog. Theor. Phys. Suppl.1,1(1935)].
- [16] S. H. Neddermeyer and C. D. Anderson, “Note on the Nature of Cosmic Ray Particles”, *Phys. Rev.* **51** (1937) 884–886, doi:10.1103/PhysRev.51.884.
- [17] C. M. G. Lattes, G. P. S. Occhialini, and C. F. Powell, “Observations on the Tracks of Slow Mesons in Photographic Emulsions. 1”, *Nature* **160** (1947) 453–456, doi:10.1038/160453a0.
- [18] R. P. Feynman, “Space-time approach to nonrelativistic quantum mechanics”, *Rev. Mod. Phys.* **20** (1948) 367–387, doi:10.1103/RevModPhys.20.367.
- [19] R. P. Feynman, “A Relativistic cutoff for classical electrodynamics”, *Phys. Rev.* **74** (1948) 939–946, doi:10.1103/PhysRev.74.939.
- [20] R. P. Feynman, “The Theory of positrons”, *Phys. Rev.* **76** (1949) 749–759, doi:10.1103/PhysRev.76.749.
- [21] J. S. Schwinger, “On Quantum electrodynamics and the magnetic moment of the electron”, *Phys. Rev.* **73** (1948) 416–417, doi:10.1103/PhysRev.73.416.

- [22] J. S. Schwinger, “Quantum electrodynamics. I A covariant formulation”, *Phys. Rev.* **74** (1948) 1439, doi:10.1103/PhysRev.74.1439.
- [23] S.-I. Tomonaga and J. R. Oppenheimer, “On Infinite Field Reactions in Quantum Field Theory”, *Phys. Rev.* **74** (1948) 224–225, doi:10.1103/PhysRev.74.224.
- [24] F. J. Dyson, “The Radiation theories of Tomonaga, Schwinger, and Feynman”, *Phys. Rev.* **75** (1949) 486–502, doi:10.1103/PhysRev.75.486.
- [25] G. D. Rochester and C. C. Butler, “Evidence for the Existence of New Unstable Elementary Particles”, *Nature* **160** (1947) 855–857, doi:10.1038/160855a0.
- [26] V. D. Hopper and S. Biswas, “Evidence Concerning the Existence of the New Unstable Elementary Neutral Particle”, *Phys. Rev.* **80** (Dec, 1950) 1099, doi:10.1103/PhysRev.80.1099.
- [27] M. Gell-Mann, “A Schematic Model of Baryons and Mesons”, *Phys. Lett.* **8** (1964) 214–215, doi:10.1016/S0031-9163(64)92001-3.
- [28] G. Zweig, “An  $SU_3$  model for strong interaction symmetry and its breaking; Version 2”,. Version 1 is CERN preprint 8182/TH.401, Jan. 17, 1964.
- [29] V. E. Barnes et al., “Observation of a Hyperon with Strangeness -3”, *Phys. Rev. Lett.* **12** (1964) 204–206, doi:10.1103/PhysRevLett.12.204.
- [30] J. D. Bjorken and S. L. Glashow, “Elementary Particles and  $SU(4)$ ”, *Phys. Lett.* **11** (1964) 255–257, doi:10.1016/0031-9163(64)90433-0.
- [31] S. L. Glashow, J. Iliopoulos, and L. Maiani, “Weak Interactions with Lepton-Hadron Symmetry”, *Phys. Rev.* **D2** (1970) 1285–1292, doi:10.1103/PhysRevD.2.1285.
- [32] E598 Collaboration, “Experimental Observation of a Heavy Particle J”, *Phys. Rev. Lett.* **33** (1974) 1404–1406, doi:10.1103/PhysRevLett.33.1404.

- [33] SLAC-SP-017 Collaboration, “Discovery of a Narrow Resonance in  $e^+ e^-$  Annihilation”, *Phys. Rev. Lett.* **33** (1974) 1406–1408, doi:10.1103/PhysRevLett.33.1406. [Adv. Exp. Phys.5,141(1976)].
- [34] M. L. Perl et al., “Evidence for Anomalous Lepton Production in  $e^+e^-$  Annihilation”, *Phys. Rev. Lett.* **35** (1975) 1489–1492, doi:10.1103/PhysRevLett.35.1489.
- [35] S. W. Herb et al., “Observation of a Dimuon Resonance at 9.5-GeV in 400-GeV Proton-Nucleus Collisions”, *Phys. Rev. Lett.* **39** (1977) 252–255, doi:10.1103/PhysRevLett.39.252.
- [36] CDF Collaboration, “Observation of top quark production in  $\bar{p}p$  collisions”, *Phys. Rev. Lett.* **74** (1995) 2626–2631, doi:10.1103/PhysRevLett.74.2626, arXiv:hep-ex/9503002.
- [37] D0 Collaboration, “Observation of the top quark”, *Phys. Rev. Lett.* **74** (1995) 2632–2637, doi:10.1103/PhysRevLett.74.2632, arXiv:hep-ex/9503003.
- [38] TASSO Collaboration, “High energy trends in  $e^+e^-$  physics”, *Invited talk at Geneva Conference* (1979).
- [39] Gargamelle Neutrino Collaboration, “Observation of Neutrino Like Interactions Without Muon Or Electron in the Gargamelle Neutrino Experiment”, *Phys. Lett.* **B46** (1973) 138–140, doi:10.1016/0370-2693(73)90499-1.
- [40] P. W. Higgs, “Broken symmetries, massless particles and gauge fields”, *Phys. Lett.* **12** (1964) 132–133, doi:10.1016/0031-9163(64)91136-9.
- [41] P. W. Higgs, “Broken Symmetries and the Masses of Gauge Bosons”, *Phys. Rev. Lett.* **13** (1964) 508–509, doi:10.1103/PhysRevLett.13.508.
- [42] P. W. Higgs, “Spontaneous Symmetry Breakdown without Massless Bosons”, *Phys. Rev.* **145** (1966) 1156–1163, doi:10.1103/PhysRev.145.1156.

- [43] F. Englert and R. Brout, “Broken Symmetry and the Mass of Gauge Vector Mesons”, *Phys. Rev. Lett.* **13** (1964) 321–323, doi:10.1103/PhysRevLett.13.321.
- [44] G. S. Guralnik, C. R. Hagen, and T. W. B. Kibble, “Global Conservation Laws and Massless Particles”, *Phys. Rev. Lett.* **13** (1964) 585–587, doi:10.1103/PhysRevLett.13.585.
- [45] UA1 Collaboration, “Experimental Observation of Isolated Large Transverse Energy Electrons with Associated Missing Energy at  $\sqrt{s} = 540$  GeV”, *Phys. Lett. B* **122** (1983) 103–116, doi:10.1016/0370-2693(83)91177-2.
- [46] UA2 Collaboration, “Observation of Single Isolated Electrons of High Transverse Momentum in Events with Missing Transverse Energy at the CERN  $p\bar{p}$  Collider”, *Phys. Lett. B* **122** (1983) 476–485, doi:10.1016/0370-2693(83)91605-2.
- [47] UA1 Collaboration, “Experimental Observation of Lepton Pairs of Invariant Mass Around 95-GeV/c<sup>2</sup> at the CERN SPS Collider”, *Phys. Lett. B* **126** (1983) 398–410, doi:10.1016/0370-2693(83)90188-0.
- [48] UA1 Collaboration, “Further Evidence for Charged Intermediate Vector Bosons at the SPS Collider”, *Phys. Lett. B* **129** (1983) 273–282, doi:10.1016/0370-2693(83)90860-2.
- [49] UA2 Collaboration, “Evidence for  $Z^0 \rightarrow e^+e^-$  at the CERN  $p\bar{p}$  Collider”, *Phys. Lett. B* **129** (1983) 130–140, doi:10.1016/0370-2693(83)90744-X.
- [50] ATLAS Collaboration, “Observation of a new particle in the search for the Standard Model Higgs boson with the ATLAS detector at the LHC”, *Phys. Lett. B* **716** (2012) 1–29, doi:10.1016/j.physletb.2012.08.020, arXiv:1207.7214.

- [51] CMS Collaboration, “Observation of a new boson at a mass of 125 GeV with the CMS experiment at the LHC”, *Phys. Lett. B* **716** (2012) 30–61, doi:10.1016/j.physletb.2012.08.021, arXiv:1207.7235.
- [52] ATLAS Collaboration, “Updated coupling measurements of the Higgs boson with the ATLAS detector using up to  $25 \text{ fb}^{-1}$  of proton-proton collision data”, (2014). ATLAS-CONF-2014-009.
- [53] CMS Collaboration, “Combination of standard model Higgs boson searches and measurements of the properties of the new boson with a mass near 125 GeV”, (2013). CMS-PAS-HIG-13-005.
- [54] Super-Kamiokande Collaboration, “Evidence for oscillation of atmospheric neutrinos”, *Phys. Rev. Lett.* **81** (1998) 1562–1567, doi:10.1103/PhysRevLett.81.1562, arXiv:hep-ex/9807003.
- [55] Super-Kamiokande Collaboration, “Constraints on neutrino oscillations using 1258 days of Super-Kamiokande solar neutrino data”, *Phys. Rev. Lett.* **86** (2001) 5656–5660, doi:10.1103/PhysRevLett.86.5656, arXiv:hep-ex/0103033.
- [56] SNO Collaboration, “Direct evidence for neutrino flavor transformation from neutral current interactions in the Sudbury Neutrino Observatory”, *Phys. Rev. Lett.* **89** (2002) 011301, doi:10.1103/PhysRevLett.89.011301, arXiv:nucl-ex/0204008.
- [57] KamLAND Collaboration, “Measurement of neutrino oscillation with KamLAND: Evidence of spectral distortion”, *Phys. Rev. Lett.* **94** (2005) 081801, doi:10.1103/PhysRevLett.94.081801, arXiv:hep-ex/0406035.
- [58] K2K Collaboration, “Evidence for muon neutrino oscillation in an accelerator-based experiment”, *Phys. Rev. Lett.* **94** (2005) 081802, doi:10.1103/PhysRevLett.94.081802, arXiv:hep-ex/0411038.

- [59] MINOS Collaboration, “Observation of muon neutrino disappearance with the MINOS detectors and the NuMI neutrino beam”, *Phys. Rev. Lett.* **97** (2006) 191801, [doi:10.1103/PhysRevLett.97.191801](https://doi.org/10.1103/PhysRevLett.97.191801), [arXiv:hep-ex/0607088](https://arxiv.org/abs/hep-ex/0607088).
- [60] Particle Data Group Collaboration, “Review of Particle Physics”, *Chin. Phys. C* **38** (2014) 090001, [doi:10.1088/1674-1137/38/9/090001](https://doi.org/10.1088/1674-1137/38/9/090001).
- [61] V. Fock, “On the invariant form of the wave equation and the equations of motion for a charged point mass. (In German and English)”, *Z. Phys.* **39** (1926) 226–232, [doi:10.1007/BF01321989](https://doi.org/10.1007/BF01321989). [Surveys High Energ. Phys.5,245(1986)].
- [62] M. E. Peskin and D. V. Schroeder, “An Introduction to quantum field theory”. Addison-Wesley (1995) 842 p, Reading, USA, 1995.
- [63] S. Kluth, “Review of alpha(s) Measurements”, *Conf. Proc. C* **060726** (2006) 449–452, [arXiv:hep-ex/0609020](https://arxiv.org/abs/hep-ex/0609020). [,449(2006)].
- [64] D. J. Gross and F. Wilczek, “Asymptotically Free Gauge Theories. 1”, *Phys. Rev. D* **8** (1973) 3633–3652, [doi:10.1103/PhysRevD.8.3633](https://doi.org/10.1103/PhysRevD.8.3633).
- [65] D. J. Gross and F. Wilczek, “Asymptotically Free Gauge Theories. 2.”, *Phys. Rev. D* **9** (1974) 980–993, [doi:10.1103/PhysRevD.9.980](https://doi.org/10.1103/PhysRevD.9.980).
- [66] H. D. Politzer, “Asymptotic Freedom: An Approach to Strong Interactions”, *Phys. Rept.* **14** (1974) 129–180, [doi:10.1016/0370-1573\(74\)90014-3](https://doi.org/10.1016/0370-1573(74)90014-3).
- [67] A. Djouadi, “The Anatomy of electro-weak symmetry breaking. I: The Higgs boson in the standard model”, *Phys. Rept.* **457** (2008) 1–216, [doi:10.1016/j.physrep.2007.10.004](https://doi.org/10.1016/j.physrep.2007.10.004), [arXiv:hep-ph/0503172](https://arxiv.org/abs/hep-ph/0503172).
- [68] Supernova Search Team Collaboration, “Observational evidence from supernovae for an accelerating universe and a cosmological constant”, *Astron. J.* **116** (1998) 1009–1038, [doi:10.1086/300499](https://doi.org/10.1086/300499), [arXiv:astro-ph/9805201](https://arxiv.org/abs/astro-ph/9805201).

- [69] J. C. Pati, A. Salam, and J. A. Strathdee, “Are Quarks Composite?”, *Phys. Lett.* **B59** (1975) 265, doi:10.1016/0370-2693(75)90042-8.
- [70] E. Eichten, K. D. Lane, and M. E. Peskin, “New Tests for Quark and Lepton Substructure”, *Phys. Rev. Lett.* **50** (1983) 811–814, doi:10.1103/PhysRevLett.50.811.
- [71] U. Baur, I. Hinchliffe, and D. Zeppenfeld, “Excited Quark Production at Hadron Colliders”, *Int.J.Mod.Phys.* **A2** (1987) 1285, doi:10.1142/S0217751X87000661.
- [72] U. Baur, M. Spira, and P. Zerwas, “Excited Quark and Lepton Production at Hadron Colliders”, *Phys.Rev.* **D42** (1990) 815–824, doi:10.1103/PhysRevD.42.815.
- [73] ZEUS Collaboration, “A Search for excited fermions in  $e^+p$  collisions at HERA”, *Z. Phys.* **C76** (1997) 631–646, doi:10.1007/s002880050585, arXiv:hep-ex/9708007.
- [74] B. Tomè, “Search for Excited fermions”, *PoS HEP2005* (2005) 313.
- [75] CDF Collaboration, “Search for excited quarks in  $p\bar{p}$  collisions at  $\sqrt{s} = 1.8$  TeV”, *Phys.Rev.Lett.* **72** (1994) 3004–3008, doi:10.1103/PhysRevLett.72.3004.
- [76] CDF Collaboration, “Search for new particles decaying to dijets at CDF”, *Phys.Rev.* **D55** (1997) 5263–5268, doi:10.1103/PhysRevD.55.R5263, arXiv:hep-ex/9702004.
- [77] D0 Collaboration, “Search for new particles in the two jet decay channel with the D0 detector”, *Phys.Rev.* **D69** (2004) 111101, doi:10.1103/PhysRevD.69.111101, arXiv:hep-ex/0308033.
- [78] ATLAS Collaboration, “Search for new phenomena in the dijet mass distribution using  $p - p$  collision data at  $\sqrt{s} = 8$  TeV with the ATLAS detector”, *Phys. Rev.*

- D91** (2015), no. 5, 052007, doi:10.1103/PhysRevD.91.052007,  
arXiv:1407.1376.
- [79] ATLAS Collaboration, “Search for new phenomena in photon+jet events collected in proton–proton collisions at  $\sqrt{s} = 8$  TeV with the ATLAS detector”, *Phys. Lett. B* **728** (2014) 562, doi:10.1016/j.physletb.2013.12.029, arXiv:1309.3230.
- [80] CMS Collaboration, “Search for narrow resonances using the dijet mass spectrum in pp collisions at  $\sqrt{s} = 8$  TeV”, *Phys. Rev. D* **87** (2013), no. 11, 114015, doi:10.1103/PhysRevD.87.114015, arXiv:1302.4794.
- [81] O. S. Brning et al., “LHC Design Report”. CERN, Geneva, 2004.  
CERN-2004-003-V-1.
- [82] L. Evans and P. Bryant, “LHC Machine”, *JINST* **3** (2008) S08001, doi:10.1088/1748-0221/3/08/S08001.
- [83] CMS Collaboration, “The CMS experiment at the CERN LHC”, *JINST* **3** (2008) S08004, doi:10.1088/1748-0221/3/08/S08004.
- [84] “CERN Experiments and Facilities”. <http://home.web.cern.ch/about>. Accessed, 2015.
- [85] “CERN Document Server”. <http://cds.cern.ch>. Accessed, 2015.
- [86] ATLAS Collaboration, A. Airapetian et al., “ATLAS detector and physics performance: Technical Design Report, 1”. TDR ATLAS. CERN, Geneva, 1999. ATLAS-TDR-014; CERN-LHCC-99-014.
- [87] CMS Collaboration, G. L. Bayatian et al., “CMS Physics: Technical Design Report Volume 1: Detector Performance and Software”. TDR CMS. CERN, Geneva, 2006. CERN-LHCC-2006-001.

- [88] ALICE Collaboration, P. Cortese et al., “ALICE physics performance: Technical Design Report”. TDR ALICE. CERN, Geneva, 2005. ALICE-TDR-13; CERN-LHCC-2005-030.
- [89] LHCb Collaboration, R. Antunes-Nobrega et al., “LHCb reoptimized detector design and performance: Technical Design Report”. TDR LHCb. CERN, Geneva, 2003. LHCb-TDR-9; CERN-LHCC-2003-030.
- [90] R. W. Assmann, F. Schmidt, F. Zimmermann, and M. P. Zorzano-Mier, “Equilibrium Beam Distribution and Halo in the LHC”,. Same report as LHC-Project-Report-597.
- [91] CMS Collaboration, S. Chatrchyan et al., “CMS Luminosity - Public Results”. <https://twiki.cern.ch/twiki/bin/view/CMSPublic/LumiPublicResults>. Accessed: 2014-09-30.
- [92] CMS Collaboration, “The CMS magnet project: Technical Design Report”. Technical Design Report CMS. CERN, Geneva, 1997.
- [93] CMS CollaborationV. Karimäki, et al., “The CMS tracker system project: Technical Design Report”. Technical Design Report CMS. CERN, Geneva, 1997.
- [94] CMS Collaboration, “Description and performance of track and primary-vertex reconstruction with the CMS tracker”, *JINST* **9** (2014), no. 10, P10009, doi:10.1088/1748-0221/9/10/P10009, arXiv:1405.6569.
- [95] CMS Collaboration, “Studies of Tracker Material”, (2010). CMS-PAS-TRK-10-003.
- [96] M. Atac et al., “Beam test results of the US - CMS forward pixel detector”, *Nucl. Instrum. Meth.* **A488** (2002) 271–281, doi:10.1016/S0168-9002(02)00472-2.
- [97] CMS Collaboration, “The CMS electromagnetic calorimeter project: Technical Design Report”. TDR CMS. CERN, Geneva, 1997. CERN-LHCC-97-033.

- [98] CMS Collaboration, “Electromagnetic calorimeter calibration with 7 TeV data”, (2010). CMS-PAS-EGM-10-003.
- [99] CMS Collaboration, “The CMS hadron calorimeter project: Technical Design Report”. TDR CMS. CERN, Geneva, 1997. CERN-LHCC-97-031.
- [100] CMS HCAL Collaboration, “Design, performance, and calibration of CMS hadron-barrel calorimeter wedges”, *Eur.Phys.J.* **C55** (2008) 159–171, doi:10.1140/epjc/s10052-008-0573-y.
- [101] CMS HCAL Collaboration, “Design, performance, and calibration of CMS hadron endcap calorimeters”, (2008). CERN-CMS-NOTE-2008-010.
- [102] CMS HCAL Collaboration, “Design, performance, and calibration of the CMS Hadron-outer calorimeter”, *Eur.Phys.J.* **C57** (2008) 653–663, doi:10.1140/epjc/s10052-008-0756-6.
- [103] G. Bayatian et al., “Design, performance and calibration of the CMS forward calorimeter wedges”, *Eur.Phys.J.* **C53** (2008) 139–166, doi:10.1140/epjc/s10052-007-0459-4.
- [104] CMS Collaboration, “Commissioning the trigger of the Compact Muon Solenoid experiment at the CERN Large Hadron Collider”, *IEEE Nucl.Sci.Symp.Conf.Rec.* (2010) doi:10.1109/RTC.2010.5750345.
- [105] USCMS, ECAL/HCAL Collaboration, “The CMS barrel calorimeter response to particle beams from 2-GeV/c to 350-GeV/c”, *Eur.Phys.J.* **C60** (2009) 359–373, doi:10.1140/epjc/s10052-009-0959-5, 10.1140/epjc/s10052-009-1024-0.
- [106] DREAM Collaboration, “The DREAM project: Towards the ultimate in calorimetry”, *Nucl. Instrum. Meth.* **A617** (2010) 129–133, doi:10.1016/j.nima.2009.09.118.

- [107] CMS Collaboration, “The CMS muon project: Technical Design Report”. TDR CMS. CERN, Geneva, 1997. CERN-LHCC-97-032.
- [108] CMS Collaboration, G. L. Bayatyan et al., “CMS TriDAS project: Technical Design Report, Volume 1: The Trigger Systems”. TDR CMS. CERN, Geneva, 2000. CMS-TDR-6-1; CERN-LHCC-2000-038.
- [109] CMS Collaboration, S. Cittolin, A. Rcz, and P. Sphicas, “CMS The TriDAS Project: Technical Design Report, Volume 2: Data Acquisition and High-Level Trigger. CMS trigger and data-acquisition project”. TDR CMS. CERN, Geneva, 2002. CMS-TDR-6; CERN-LHCC-2002-026.
- [110] A. Buckley et al., “General-purpose event generators for LHC physics”, *Phys. Rept.* **504** (2011) 145–233, doi:10.1016/j.physrep.2011.03.005, arXiv:1101.2599.
- [111] M. Dobbs et al., “Les Houches guidebook to Monte Carlo generators for hadron collider physics”, arXiv:hep-ph/0403045.
- [112] T. Sjostrand, S. Mrenna, and P. Z. Skands, “PYTHIA 6.4 Physics and Manual”, *JHEP* **0605** (2006) 026, doi:10.1088/1126-6708/2006/05/026, arXiv:hep-ph/0603175.
- [113] J. Alwall et al., “The automated computation of tree-level and next-to-leading order differential cross sections, and their matching to parton shower simulations”, *JHEP* **1407** (2014) 079, doi:10.1007/JHEP07(2014)079, arXiv:1405.0301.
- [114] M. Bahr et al., “Herwig++ Physics and Manual”, *Eur.Phys.J.* **C58** (2008) 639–707, doi:10.1140/epjc/s10052-008-0798-9, arXiv:0803.0883.
- [115] G. Altarelli and G. Parisi, “Asymptotic Freedom in Parton Language”, *Nucl.Phys.* **B126** (1977) 298, doi:10.1016/0550-3213(77)90384-4.

- [116] P. M. Nadolsky et al., “Implications of CTEQ global analysis for collider observables”, *Phys.Rev.* **D78** (2008) 013004, [doi:10.1103/PhysRevD.78.013004](https://doi.org/10.1103/PhysRevD.78.013004), [arXiv:0802.0007](https://arxiv.org/abs/0802.0007).
- [117] J. Pumplin et al., “New generation of parton distributions with uncertainties from global QCD analysis”, *JHEP* **0207** (2002) 012, [doi:10.1088/1126-6708/2002/07/012](https://doi.org/10.1088/1126-6708/2002/07/012), [arXiv:hep-ph/0201195](https://arxiv.org/abs/hep-ph/0201195).
- [118] A. Martin, W. Stirling, R. Thorne, and G. Watt, “Parton distributions for the LHC”, *Eur.Phys.J.* **C63** (2009) 189–285, [doi:10.1140/epjc/s10052-009-1072-5](https://doi.org/10.1140/epjc/s10052-009-1072-5), [arXiv:0901.0002](https://arxiv.org/abs/0901.0002).
- [119] T. Sjostrand and M. Bengtsson, “The Lund Monte Carlo for Jet Fragmentation and e+ e- Physics. Jetset Version 6.3: An Update”, *Comput. Phys. Commun.* **43** (1987) 367, [doi:10.1016/0010-4655\(87\)90054-3](https://doi.org/10.1016/0010-4655(87)90054-3).
- [120] M. L. Mangano et al., “ALPGEN, a generator for hard multiparton processes in hadronic collisions”, *JHEP* **0307** (2003) 001, [doi:10.1088/1126-6708/2003/07/001](https://doi.org/10.1088/1126-6708/2003/07/001), [arXiv:hep-ph/0206293](https://arxiv.org/abs/hep-ph/0206293).
- [121] T. Gleisberg et al., “Event generation with SHERPA 1.1”, *JHEP* **0902** (2009) 007, [doi:10.1088/1126-6708/2009/02/007](https://doi.org/10.1088/1126-6708/2009/02/007), [arXiv:0811.4622](https://arxiv.org/abs/0811.4622).
- [122] P. de Aquino et al., “ALOHA: Automatic Libraries Of Helicity Amplitudes for Feynman Diagram Computations”, *Comput. Phys. Commun.* **183** (2012) 2254–2263, [doi:10.1016/j.cpc.2012.05.004](https://doi.org/10.1016/j.cpc.2012.05.004), [arXiv:1108.2041](https://arxiv.org/abs/1108.2041).
- [123] J. Alwall et al., “A Standard format for Les Houches event files”, *Comput.Phys.Commun.* **176** (2007) 300–304, [doi:10.1016/j.cpc.2006.11.010](https://doi.org/10.1016/j.cpc.2006.11.010), [arXiv:hep-ph/0609017](https://arxiv.org/abs/hep-ph/0609017).

- [124] F. Krauss, “Matrix elements and parton showers in hadronic interactions”, *JHEP* **0208** (2002) 015, doi:10.1088/1126-6708/2002/08/015, arXiv:hep-ph/0205283.
- [125] M. L. Mangano, M. Moretti, and R. Pittau, “Multijet matrix elements and shower evolution in hadronic collisions:  $Wb\bar{b} + n$  jets as a case study”, *Nucl.Phys.* **B632** (2002) 343–362, doi:10.1016/S0550-3213(02)00249-3, arXiv:hep-ph/0108069.
- [126] GEANT4 Collaboration, “GEANT4: A Simulation toolkit”, *Nucl.Instrum.Meth.* **A506** (2003) 250–303, doi:10.1016/S0168-9002(03)01368-8.
- [127] CMS Collaboration, “Measurement of the Underlying Event Activity at the LHC with  $\sqrt{s} = 7$  TeV and Comparison with  $\sqrt{s} = 0.9$  TeV”, *JHEP* **1109** (2011) 109, doi:10.1007/JHEP09(2011)109, arXiv:1107.0330.
- [128] R. Field, “Early LHC Underlying Event Data - Findings and Surprises”, arXiv:1010.3558.
- [129] CMS Collaboration, “The CMS reconstruction software”, *J.Phys.Conf.Ser.* **331** (2011) 032020, doi:10.1088/1742-6596/331/3/032020.
- [130] CMS Collaboration, “Particle-Flow Event Reconstruction in CMS and Performance for Jets, Taus, and MET”, Technical Report CMS-PAS-PFT-09-001, CERN, 2009. Geneva, (Apr, 2009).
- [131] CMS Collaboration, “Commissioning of the Particle-flow Event Reconstruction with the first LHC collisions recorded in the CMS detector”, Technical Report CMS-PAS-PFT-10-001, CERN, (2010).
- [132] CMS Collaboration, “Track Reconstruction in the CMS tracker”, Technical Report CMS-NOTE-2006-041, CERN, Geneva, (Dec, 2006).

- [133] R. Fruhwirth, “Application of Kalman filtering to track and vertex fitting”, *Nucl.Instrum.Meth.* **A262** (1987) 444–450, doi:10.1016/0168-9002(87)90887-4.
- [134] CMS Collaboration, “Beam Position Determination using Tracks”, Technical Report CMS-NOTE-2007-021, CERN, Geneva, (Aug, 2007).
- [135] CMS Collaboration, “Adaptive Vertex Fitting”, Technical Report CMS-NOTE-2007-008, CERN, Geneva, (Mar, 2007).
- [136] CMS Collaboration Collaboration, “Performance of Track and Vertex Reconstruction and B-Tagging Studies with CMS in pp Collisions at  $\sqrt{s}=7$  TeV”, Technical Report CMS-CR-2011-047, CERN, Geneva, (Mar, 2011).
- [137] CMS Collaboration, “Performance of photon reconstruction and identification with the CMS detector in proton-proton collisions at  $\sqrt{s} = 8$  TeV”, arXiv:1502.02702.
- [138] CMS Collaboration, “Performance of Electron Reconstruction and Selection with the CMS Detector in Proton-Proton Collisions at  $\sqrt{s} = 8$  TeV”, *JINST* **10** (2015), no. 06, P06005, doi:10.1088/1748-0221/10/06/P06005, arXiv:1502.02701.
- [139] CMS Collaboration, “Review of clustering algorithms and energy corrections in ECAL”, Technical Report CMS-IN-2010-008, CERN, Geneva, (Mar, 2010).
- [140] E. Meschi, T. Monteiro, C. Seez, and P. Vikas, “Electron Reconstruction in the CMS Electromagnetic Calorimeter”, Technical Report CMS-NOTE-2001-034, CERN, Geneva, (Jun, 2001).
- [141] CMS Collaboration, “Electromagnetic calorimeter commissioning and first results with 7 TeV data”, Technical Report CMS-NOTE-2010-012, CERN, Geneva, (Jul, 2010).

- [142] CMS Collaboration, “Transverse-momentum and pseudorapidity distributions of charged hadrons in  $pp$  collisions at  $\sqrt{s} = 7$  TeV”, *Phys.Rev.Lett.* **105** (2010) 022002, doi:10.1103/PhysRevLett.105.022002, arXiv:1005.3299.
- [143] M. Cacciari, G. P. Salam, and G. Soyez, “The Anti- $k_t$  jet clustering algorithm”, *JHEP* **0804** (2008) 063, doi:10.1088/1126-6708/2008/04/063, arXiv:0802.1189.
- [144] CMS Collaboration, “Particle-flow commissioning with muons and electrons from J/Psi and W events at 7 TeV”, Technical Report CMS-PAS-PFT-10-003, CERN, 2010. Geneva, (2010).
- [145] S. Catani, Y. L. Dokshitzer, M. Seymour, and B. Webber, “Longitudinally invariant  $k_t$  clustering algorithms for hadron hadron collisions”, *Nucl.Phys.* **B406** (1993) 187–224, doi:10.1016/0550-3213(93)90166-M.
- [146] Y. L. Dokshitzer, G. Leder, S. Moretti, and B. Webber, “Better jet clustering algorithms”, *JHEP* **9708** (1997) 001, doi:10.1088/1126-6708/1997/08/001, arXiv:hep-ph/9707323.
- [147] CMS Collaboration, “Plans for Jet Energy Corrections at CMS”, Technical Report CMS-PAS-JME-07-002, CERN, 2008. Geneva, (Jul, 2008).
- [148] M. Cacciari and G. P. Salam, “Pileup subtraction using jet areas”, *Phys.Lett.* **B659** (2008) 119–126, doi:10.1016/j.physletb.2007.09.077, arXiv:0707.1378.
- [149] CMS Collaboration, “Jet Identification in the CMS detector”. <https://twiki.cern.ch/twiki/bin/view/CMS/JetID>. Accessed: 2015.
- [150] S. Bhattacharya, S. S. Chauhan, B. C. Choudhary, and D. Choudhury, “Quark Excitations Through the Prism of Direct Photon Plus Jet at the LHC”, *Phys.Rev.* **D80** (2009) 015014, doi:10.1103/PhysRevD.80.015014, arXiv:0901.3927.

- [151] C. Eck et al., “LHC computing Grid: Technical Design Report. Version 1.06 (20 Jun 2005)”. Technical Design Report LCG. CERN, Geneva, 2005.
- [152] CMS Collaboration, “CRAB: Distributed analysis tool for CMS”, Technical Report CMS-CR-2009-318, CERN, Geneva, (Oct, 2009).
- [153] CMS Collaboration, S. Chatrchyan et al., “CMSSW Application Framework”.  
`https://twiki.cern.ch/twiki/bin/view/CMSPublic/WorkBookCMSSWFramework`. Accessed: 2015-05-30.
- [154] CMS Collaboration, S. Chatrchyan et al., “Pile-up scenario for Run-I”.  
`https://twiki.cern.ch/twiki/bin/view/CMS/PdmVPileUpDescription,https://twiki.cern.ch/twiki/bin/view/CMS/PileupJSONFileforData`. Accessed: 2015-05-30.
- [155] M. Cacciari, G. P. Salam, and G. Soyez, “FastJet User Manual”, *Eur. Phys. J. C* **72** (2012) 1896, doi:10.1140/epjc/s10052-012-1896-2, arXiv:1111.6097.
- [156] M. S. David Futyan, Mauro Donega, “Updated measurements of the new Higgs-like boson at 125 GeV in the two photon decay channel”, *CMS AN 2013/008* (2013).
- [157] S. D. Ellis, Z. Kunszt, and D. E. Soper, “Two jet production in hadron collisions at order  $\alpha_s^3$  in QCD”, *Phys.Rev.Lett.* **69** (1992) 1496–1499, doi:10.1103/PhysRevLett.69.1496.
- [158] W. Giele, E. N. Glover, and D. A. Kosower, “Higher order corrections to jet cross-sections in hadron colliders”, *Nucl.Phys.* **B403** (1993) 633–670, doi:10.1016/0550-3213(93)90365-V, arXiv:hep-ph/9302225.

- [159] R. M. Harris and K. Kousouris, “Searches for Dijet Resonances at Hadron Colliders”, *Int. J. Mod. Phys. A* **26** (2011) 5005–5055,  
 doi:10.1142/S0217751X11054905, arXiv:1110.5302.
- [160] CDF Collaboration, “Search for new particles decaying into dijets in proton-antiproton collisions at  $\sqrt{s} = 1.96$  TeV”, *Phys. Rev. D* **79** (2009) 112002,  
 doi:10.1103/PhysRevD.79.112002, arXiv:0812.4036.
- [161] ATLAS Collaboration, “Search for production of resonant states in the photon-jet mass distribution using pp collisions at  $\sqrt{s} = 7$  TeV collected by the ATLAS detector”, *Phys. Rev. Lett.* **108** (2012) 211802,  
 doi:10.1103/PhysRevLett.108.211802, arXiv:1112.3580.
- [162] CMS Collaboration, “Search for narrow resonances using the dijet mass spectrum in pp collisions at  $\sqrt{s} = 8$  TeV”, *Phys. Rev. D* **87** (2013) 114015,  
 doi:10.1103/PhysRevD.87.114015, arXiv:1302.4794.
- [163] CMS Collaboration, S. Chatrchyan et al., “Physics Analysis Oriented Event Display”.  
<https://twiki.cern.ch/twiki/bin/view/CMSPublic/WorkBookFireworks>.  
 Accessed: 2015.
- [164] S. Ozturk et al., “Plans to Search for New Particles Decaying to Dijets in  $pp$  Collisions at  $\sqrt{s} = 10$  TeV”, *CMS AN* **2009/070** (2009).
- [165] CMS Collaboration, “Determination of Jet Energy Calibration and Transverse Momentum Resolution in CMS”, *JINST* **6** (2011) P11002,  
 doi:10.1088/1748-0221/6/11/P11002, arXiv:1107.4277.
- [166] CMS Collaboration, “Measurement of the  $W\gamma$  and  $Z\gamma$  inclusive cross sections in pp collisions at  $\sqrt{s} = 7$  TeV and limits on anomalous triple gauge boson couplings”, *Phys. Rev. D* **89** (2014) 092005,  
 doi:10.1103/PhysRevD.89.092005, arXiv:1308.6832.

- [167] CMS Collaboration, “Energy calibration and resolution of the CMS electromagnetic calorimeter in pp collisions at  $\sqrt{s} = 7$  TeV”, *JINST* **8** (2013) P09009, doi:10.1088/1748-0221/8/09/P09009, arXiv:1306.2016.
- [168] A. Giannanco, “The Fast Simulation of the CMS Experiment”, *J. Phys. Conf. Ser.* **513** (2014) 022012, doi:10.1088/1742-6596/513/2/022012.
- [169] CMS Collaboration, S. Chatrchyan et al., “CMS Luminosity - Public Results”. <https://twiki.cern.ch/twiki/bin/view/CMSPublic/LumiPublicResults>. Accessed: 2015-05-30.
- [170] CMS Collaboration, “CMS Luminosity Based on Pixel Cluster Counting - Summer 2013 Update”, Technical Report CMS-PAS-LUM-13-001, CERN, Geneva, (2013).
- [171] Particle Data Group Collaboration, “Review of Particle Physics”, *Phys. Rev. D* **86** (2012) 010001, doi:10.1103/PhysRevD.86.010001. Chapter-36, Pg.390-401.
- [172] CMS Collaboration, S. Chatrchyan et al., “Dijet Limit Code”. <https://twiki.cern.ch/twiki/bin/view/CMS/DijetLimitCode>. Accessed: 2015.
- [173] CMS Collaboration, B. Cousins, “Lognormal and Gamma distribution instead of truncated Gaussian for pdf of positive nuisance parameter.”. [http://www.physics.ucla.edu/~cousins/stats/cousins\\_lognormal\\_prior.pdf](http://www.physics.ucla.edu/~cousins/stats/cousins_lognormal_prior.pdf). 2010.